DEVELOPMENT OF MEMS THERMOPILE AND

RELATED APPLICATIONS

BY

Zhou Huchuan

(*B. Engineering., UESTC*)

A THESIS SUBMITTED

FOR THE DEGREE OF DOCTOR OF PHILOSOPHY

DEPARTMENT OF ELECTRICAL AND COMPUTER ENGINEERING

NATIONAL UNIVERSITY OF SINGAPORE

2014

DECLARATION

I hereby declare that this thesis is my original work and it has been written by me in its entirety. I have duly acknowledged all the sources of information which have been used in the thesis.

This thesis has also not been submitted for any degree in any university previously.

_____

Zhou Huchuan

16 Aug 2014

Acknowledgements

First and foremost, I would like to express my sincere gratitude to my supervisors Prof. Chengkuo Lee and Dr. Campanella Pineda Humberto for their consistent support, encouragement and discussions during my entire Ph.D. study. I would like to gratefully acknowledge Prof. Lee for his invaluable guidance and insightful enlightenment throughout my Ph.D candidature. I would never forget his patience, encouragement and immense knowledge, which help me working through all the challenges during past four years. I also deeply appreciate Dr. Humberto for offering such precious attachment opportunity in Institute of Microelectronics (IME) and his continuous consideration on me. I really could not have imagined the possibility of this dissertation without gracious concerns and kind help from both of my supervisors.

Besides, I would like to thank Dr. Piotr Kropelnicki for his valuable suggestions and instructions. Without his advices I cannot get my expertise in thermopile and IR sensor. I will always remember your advice during the most important two years in IME. Although you are not my supervisor officially, I will always thank you and respect you as my best teacher and friends.

Meanwhile, I am very grateful to Dr. Wang Jian, Dr. Singh Navab, for their continuous support and guidance during my attachment period. Without their helps, I would not able to complete the fabrication and characterization successfully.

List of Acronyms

MEMS	Micro-electro-mechanical systems
CMOS	Complementary metal-oxide-semiconductor
ICs	integrated circuits
IR	infrared
Te	Tellurium
Bi	Bismuth
Sb	Antimony
ZT	Figure-of-merit
Si	Silicon
SiGe	Silicon-Germanium
SiNW	Silicon Nanowires
poly-Si	Polycrystalline Silicon
GaAs	Gallium Arsenide
LPCVD	Low-pressure Chemical vapor deposition

Bi_xSb_y	Bismuth antimonide
Bi_2Te_3	Bismuth telluride
PbTe	Lead telluride
DL	Double layer
Cs	Cesium
$CsBi_4Te_6$	Cesium-doped Bismuth telluride
GeTe	Germanium telluride
SiTe	Silicon telluride
$AgSbTe_2$	Silver-doped antimony telluride
TAGS	Te/Sb/Ge/Ag
DC	Direct Current
Al	aluminum
CO_x	oxocarbon
NDIR	non-dispersive infrared

SDL thermopile	stacked double layer thermopile
CNTs	Carbon nanotubes
NEP	noise-equivalent power
2D	Two dimensions
SiO_2	Silicon dioxide
LPCVD	low-pressure chemical vapor deposition
RIE	Reactive ion etching
PECVD	Plasma-enhanced chemical vapour deposition
XeF_2	Xenon difluoride
DRIE	Deep reactive ion etching
SF_6	Sulfur Hexafluoride
C_4F_8	Octafluorocyclobutane
TCRs	temperature coefficients of resistance
IRFPAs	Infrared Focal Plane Arrays

Ge	germanium
SiC	silicon carbide
ZnSe	Zinc selenide
SEM	Scanning electron microscopy
Al_2O_3	Aluminium oxide
FTIR	Fourier transform infrared spectroscopy
EBL	electron beam lithography
TiN	Titanium Nitride
ALD	Atomic layer deposition
MoS_2	Molybdenum disulfide
CO	carbon monoxide
CH_4	methane
N_2O	nitrous oxide
O_3	ozone

CO_2	Carbon dioxide
H_2O	water
CRR	Close ring resonator
ECRR	Eccentric close ring resonator
3D	Three dimension

Table of Content

Summary

Nowadays, thermopile has been widely utilized in various applications ranging from military applications, security, non-destructive inspection to healthcare. In order to realize thermopile with good performance (e.g. high responsivity, low electrical noise etc.), the researchers need to conduct the improvement in terms of thermopile structure layout and thermoelectric materials. Furthermore, the design of wavelength-dependent characteristics of infrared (IR) absorber on thermopile detector area is a critical task for some application-specific features required in IR image sensors and gas sensors.

A stacked double layer (SDL) thermopile is designed, fabricated and characterized showing that the SDL thermopile has advantages in terms of the thermal conductance and Seebeck coefficient difference. Besides, the SDL thermopile provides improved sensor performance compared with conventional coplanar thermopiles in terms of a smaller footprint and smaller surface area exposed to air. Thus, the SDL thermopile is a superior design in applications in which thermopiles are operated exposed to air.

This new design of SDL thermopile is applied as a single IR sensor integrated with a wavelength-selective IR absorber. The temperature dependency of this IR sensor was conducted to prove that this wavelength-selective IR sensor is capable of being applied at high temperature.

Then a nanometer-thick poly-Si layer with enhanced phonon-boundary scattering was studied. The experimental results show that the nanometer-thick poly-Si is a

promising thermoelectric material. A theoretical analysis and characterization of the material were conducted and presented. Furthermore, the design, fabrication and characterization of a thermopile IR sensor constructed with a nanometer-thick poly-Si layer are presented to demonstrate the advantages of this material.

Two types of IR absorbers with different concepts for the IR absorber design are studied to explore different applications of thermopile. The first is a broadband IR absorber that uses mixed SU-8 and carbon nanotubes (CNTs). The second is a wavelength-selective interferometric absorber that can provide one selected absorption peak of the IR radiation.

List of Tables

List of Figures

Chapter I: Introduction

1.1 Background

Increasingly more microelectromechanical systems (MEMS) based on the complementary metal-oxide semiconductor (CMOS)-compatible process are being developed for various applications because of the inherent advantages of the CMOS-compatible process, including small dimensions, light weight, fast response and ability to be integrated circuits (ICs) that can be used for further signal processing [1-2]. One of the representative CMOS MEMS devices is the thermoelectric microdevice [3-8].

The way the thermoelectric devices work is based on a physical phenomenon called the Seebeck effect. When two different materials are connected in series, the temperature gradient will contribute to an electrical voltage. Figure 1.1 shows a simple schematic drawing to illustrate the Seebeck coefficient. As shown in this figure, the thermocouple is formed by two materials, material A and material B. When infrared (IR) radiation (Φ_{rad}) reaches the absorber on the left end as shown in Figure 1.1, the end will be heated. This end is called the hot junction. The other end of the thermocouple on the right, which is called the cold junction, is thermally connected to a heat sink. As such, there will be a temperature difference (ΔT) between the cold junction and hot junction. Due to the Seebeck effect, a voltage output (V_{out}) could be detected on the output end of the thermocouple between material A and material B, in this case is the right end, as illustrated in figure 1.1.

1
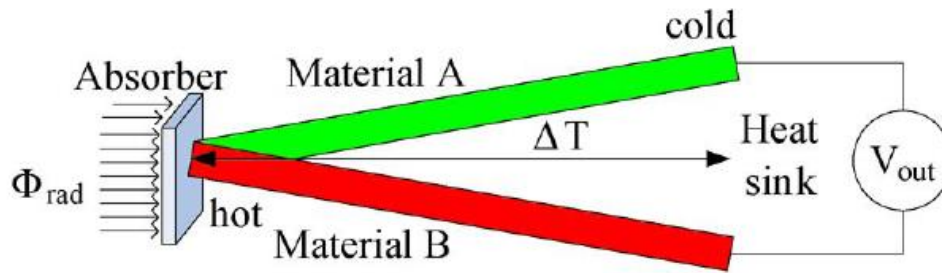
Figure 1.1. Schematic drawing of the Seebeck effect [9].

Recently, the use of the Seebeck effect has been commercialized and demonstrated in many electric microdevices for various applications, including non-contact temperature sensing [10], IR focal plane image arrays [11-14], air flow sensors [15], gas sensors [16], accelerometers [17, 18] and AC-DC converters [19]. In contrast, the Peltier effect, which showcases the complete opposite correlation between temperature difference and electrical voltage from the Seebeck effect, has also been used in thermoelectric microdevices. One application is to create thermoelectric coolers [20-26]. Thermoelectric microdevices have often been configured in such way that they are fabricated with the physical support of the silicon (Si) substrates and polymer-based flexible substrates using MEMS technology. For example, parts of thermoelectric membranes are suspended above micro-cavities [27-29]; vertical thermocouple arrays are formed in polymer substrates [30, 31]. An array of thermocouples connected in series could create larger output of voltage; such combination of thermocouples in series is called a thermopile.

1.2 Literature review

1.2.1 Thermoelectric materials

The selection of thermoelectric materials is one of the most important steps in designing a thermopile. The most widely used thermoelectric materials are tellurium (Te), in an alloy that also contains bismuth (Bi), antimony (Sb), or other elements. Those elements [32-40, 93] has high figure-of-merit, $ZT=\alpha^2 T/\rho k \approx 1$, where α, ρ, k and T are the Seebeck coefficient, electrical resistivity, thermal conductivity and absolute temperature, respectively. Creating thermoelectric materials with $ZT > 1$ with a wide range of operating temperatures remains a challenging task [41]. Nowadays, CMOS materials, such as silicon (Si) and silicon-germanium (SiGe), have been characterized as promising thermoelectric materials. However, the relatively high thermal conductivity of Si (~150 $Wm^{-1}K^{-1}$) at room temperature restricts the ZT. Recently, a few studies have reported significant increase in the ZT value of the nanostructured Si. This is made possible by the reduction in thermal conductivity, which in turn, is caused by enhanced phonon scattering. The large increase in phonon-boundary scattering leads to a drastic reduction in the thermal conductivity; such drastic change occurs when the characteristic length scales are smaller than the mean free path of phonons on a nanometer scale [42]. For bulk Si, the average mean free path of phonons is approximately 300 nm at room temperature [43]. For instance, Si nanowires have been reported to have thermal conductivities of 0.73 $Wm^{-1}K^{-1}$, which increases ZT more than 100 times over the typical ZT of bulk Si [44]. Meanwhile, it has been reported that Si phononic nanomesh structures have a thermal conductivity of

approximately 1.5 $Wm^{-1}K^{-1}$ [45, 46]. However, mass production faces a great challenge in the fabrication process if it is desirable to incorporate Si nanowires (SiNWs) or Si nanomesh into a planar thermopile structure, which has been the primary configuration used to date. In addition, the thermoelectric characteristics of SiNWs depend highly on not only their dimension but also the nanoscopic surface morphology [47-49]. Thus, the top-down fabrication technology can make use of the reliable and predictable material properties of single-crystal Si and polycrystalline Si (poly-Si). The thermal conductivity of single-crystal Si, with has a thickness on the order of around 100 nm, has been studied [43, 50], demonstrating a reduction in the thermal conductivity by more than 50% to approximately 50 $Wm^{-1}K^{-1}$. However, this value is still considerably higher than the thermal conductivity of bulk poly-Si, which is approximately 30 $Wm^{-1}K^{-1}$[51, 52]. This is because of the grain boundary scattering of phonons, which causes a reduction in the thermal conductivity [53]. In addition, a portion of n-doped dopants segregates to the grain boundaries in poly-Si, which also contributes to greater phonon scattering [54]. Advanced CMOS manufacturing technology can makes features with a few tens nanometers size and thin poly-Si layers of a few nanometers to be fabricated in 12" wafers.

1.2.1.1 History of thermoelectric materials

In 1821, Thomas Johann Seebeck discovered a current in a circuit made of two different metals when the two ends of the metals are kept at different temperatures. Seebeck also observed that a compass would deflect when brought close to the circuit above mentioned and that the deflection's magnitude increased proportionally to the increase in temperature difference [55].

In 1834, French scientist Jean Charles Athanase Peltier discovered a phenomenon that was the opposite of what has been observed in Seebeck's experiment, i.e., when a current passes through a circuit made of a certain material, one end of it could freeze water, the other end melt ice. [56]. Both discoveries - made by Seebeck and Peltier - are exemplars of the same physical theory that showcases different physical effects. It has not become clear until Brit. physicist W.T. (later known as the first Baron Kelvin) discovered something else in 1851, which became known as the Thompson effect. There began a new page of history in the physics of thermoelectricity. The Thompson effect [56] is that the rate of heat created or absorbed in a conductive material with a current flow is subjected to a temperature gradient. Furthermore, Thompson correctly predicted that the Seebeck effect and Peltier effect are actually different manifestations of the same underlying physics principal. 80 years later, in 1931, American scientist Lars Onsager confirmed Thompson's prediction and set the cornerstone for the study of thermoelectric materials. Since then, the research on thermoelectric materials and its applications became an important field of study for many decades.

1.2.1.2 Methods to enhance the ZT value

The efficiency of a thermoelectric material is defined by a unitless figure of merit, ZT, as shown in the following equation:

$$ZT = \alpha^2 T / \rho k, \tag{1.1}$$

where α, ρ, k and T are the Seebeck coefficient, electrical resistivity, thermal conductivity and absolute temperature, respectively. To achieve a high ZT, high

5

Seebeck coefficient, low thermal conductivity and electric resistivity are required. The perfect thermoelectric, which have low thermal conductivity and low electrical resistivity, are defined as "phonon glasses" and "electron-crystals" [57], which have low thermal conductivity and low electrical resistivity.

The most common method to increase *ZT* is to increase the Seebeck coefficient and to reduce the electrical resistivity by optimizing the doping concentration since the Seebeck coefficient and electrical resistivity rely highly on the carrier density. In addition, the lattice thermal conductivity can be reduced significantly by introducing the scattering center. The Seebeck coefficient, thermal conductivity and electrical resistivity are influenced by the scattering factor, carrier effective mass and carrier mobility. However, it is difficult to optimize the three parameters together as they are interrelated. i.e. the change in one will affect the other.

The main conflict in optimization of the doping concentrations is that higher doping concentration leads to lower electrical resistivity and lower thermal conductivity, which gives rise to a higher *ZT* but reduces the Seebeck coefficient at the same time, and this is undesirable. This is due to the fact that the increase in Seebeck Coefficient is proportional to the difference between the average energy of a mobile carrier and the Fermi energy. Also, when the carrier density increases, the Fermi energy increases more rapidly than the average carrier energy. Therefore, an increase in doping concentration leads to a higher carrier density, and subsequently, a decrease in Seebeck coefficient.

Equation 1.2 showcases the calculation of the Seebeck coefficient, , of metals and degenerate semiconductors [58]:

$$\alpha = \frac{8\pi^2 k_B^2}{3eh^2} m^* T \left(\frac{\pi}{3n}\right)^{2/3}, \tag{1.2}$$

where k_B is the Boltzmann constant, h is the Planck constant, e is the elementary electric charge, m^* is the density-of-states effective mass, n is the doping concentration. A higher doping concentration leads to a decrease in the Seebeck coefficient. As indicated by Equation 1.2, increasing the density-of-states effective mass m^* is also a method to enhance the Seebeck coefficient, but it is not a practical method. This is because materials that have a high density-of-states effective mass m^* also have relatively low carrier mobility, μ, and the power factor α^2/ρ is proportional to $(m^*)^{2/3}\mu$[59]. For instance, the polaron conductors, e.g., oxides or chalcogenides, have low mobility and high effective mass, whereas semiconductors, such as SiGe and GaAs, have high mobility and low effective mass [60].

However, higher doping concentration does not simply reduce *ZT*. The defects caused by implantation scatter phonons such that the thermal conductivity contributed by phonons is reduced, which, in turn, increases *ZT*. The thermal conductivity contributed by both electrons, k_e and lattice phonon scattering, k_p. The total thermal conductivity, $k=k_e + k_p$.

Wiedemann–Franz Law states that k_e is inversely proportional to the electrical resistivity, ρ, as indicated by the equation below[60]:

$$k_e = LT/\rho, \tag{1.3}$$

where *L* is the Lorenz factor, which also varies with the doping concentration.

The electrical resistivity ρ is determined by the carrier mobility μ and doping

concentration n, as indicated below:

$$\rho = \frac{1}{en\mu}. \tag{1.4}$$

Substituting Equation 1.4 into Equation 1.3, the thermal conductivity contributed by electrons is

$$k_e = LTen\mu. \tag{1.5}$$

As indicated by Equation 1.5, a low doping concentration will result in a higher electrical resistivity, thus decreasing *ZT*. In addition, Equation 1.4 illustrates that mobility carriers will reduce the electrical conductivity.

In summary, decreasing the electrical resistivity increases k_e. Thus, one of the primary methods used to increase ZT is reduce the thermal conductivity by lattice phonon scattering. However, as discussed above, introducing defects in the material by heavy implantation decreases the Seebeck coefficient. Therefore, most researchers focus on reducing the lattice thermal conductivity by using phonon engineering or low-dimensional thermoelectric materials. The lower limit of lattice thermal conductivity was derived by Spitzer to be 0.2 W/mK [61]. Because the lattice thermal conductivity has a lower limit, some researchers resort to reducing thermal conductivity contributed by electrons, k_e. Theoretically, when the distribution obeys Dirac delta distribution, which means that the carriers do not spread around the mean value, the thermal conductivity contributed by electrons can be limited, whereas the electrical resistivity does not increase [61]. Thermoelectric materials in such close-to-ideal condition have a nearly perfect performance. It is a challenge to synthesize such materials.

Minimizing the thermal conductivity is not enough to increase *ZT* to a relatively high level. Despite low thermal conductivity, it is difficult to increase *ZT* to a value higher than 1 if the Seebeck coefficient is less than 150 μV/K. The magnitude of the Seebeck coefficient of a metal is typically less than 87 μV/K [62]; most metals have a Seebeck coefficient with a magnitude between 1 to 10 μV/K, e.g., the Seebeck coefficient of aluminum is -1.4 μV/K. In contrast, semiconductors have Seebeck coefficient magnitudes on the order of 10^2 or even 10^3 μV/K. Therefore, heavily doped semiconductors are promising candidate thermoelectric materials.

Xie Jin and his colleagues [6] carefully studied the thermoelectric properties of boron- and phosphorus-doped LPCVD polycrystalline Si (poly-Si) with different doping concentrations. The poly-Si measured in his study is doped with dosages from 4×10^{15} to 10×10^{15} cm^{-2}. The implant energy for each dosage is presented in Table 1.1. The doped poly-Si layers are annealed in a furnace at 1,000°C for 30 min to activate dopants, obtain a uniform doping profile throughout the entire thickness and repair defects in the crystalline structure.

Table 1.1. Implant energies for doping poly-Si layers used reference [6].

Doping dose (at cm^{-2})	Implant energy (keV)	
	Boron doped	Phosphorus doped
4×10^{15}	70	100
6×10^{15}	70	130
8×10^{15}	80	160
10×10^{15}	80	180

The electrical resistivity, Seebeck coefficient and thermal conductivity of poly-Si with different doping dosages are shown in **Figures 1.2, 1.3 and 1.4**, respectively.
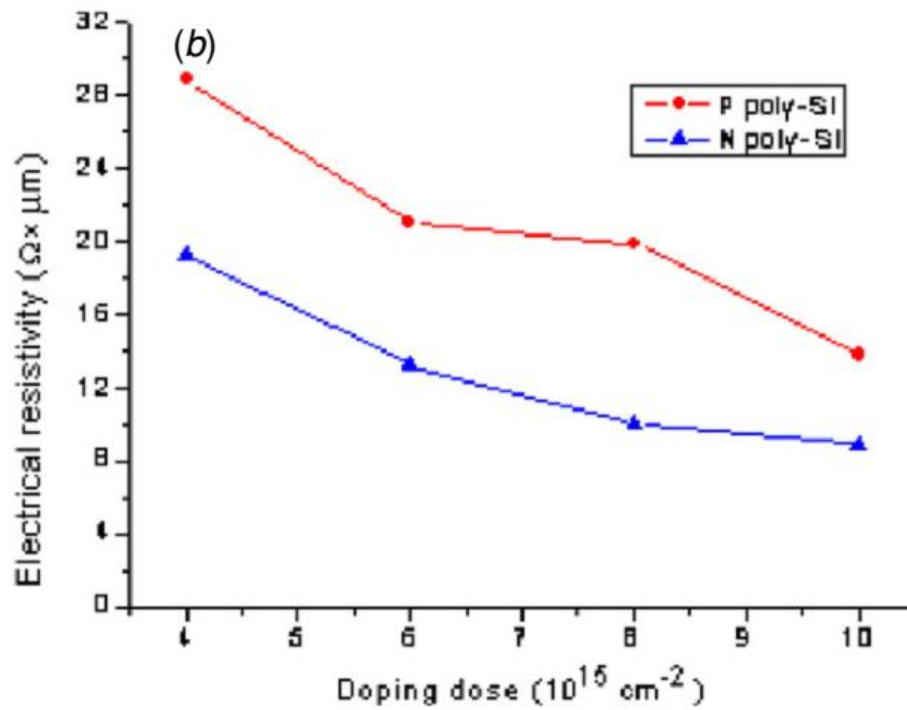
Figure 1.2. Electrical resistivity of poly-Si at different doping dosages [6].
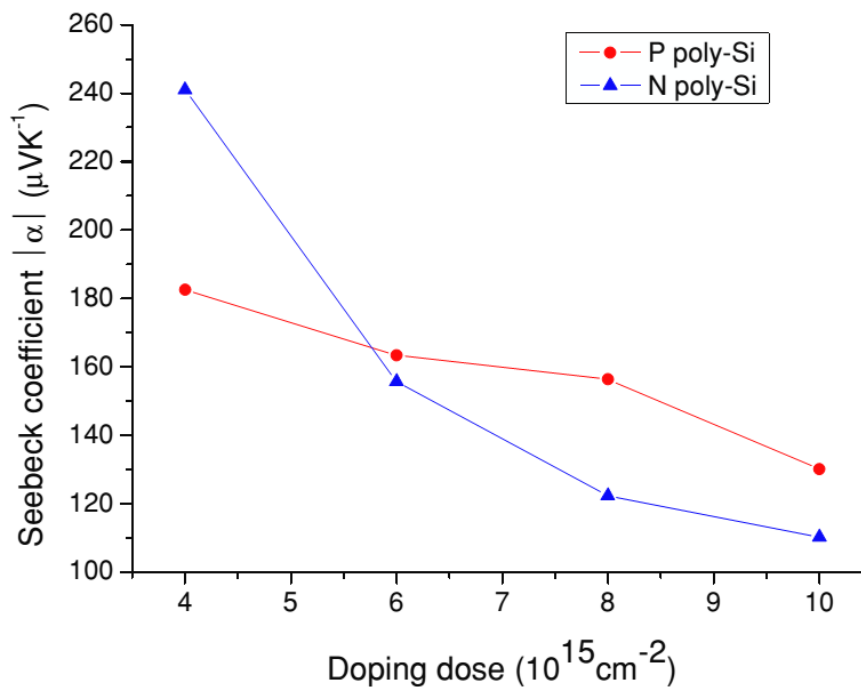
Figure 1.3. Seebeck coefficient of poly-Si at different doping dosages [6].

10
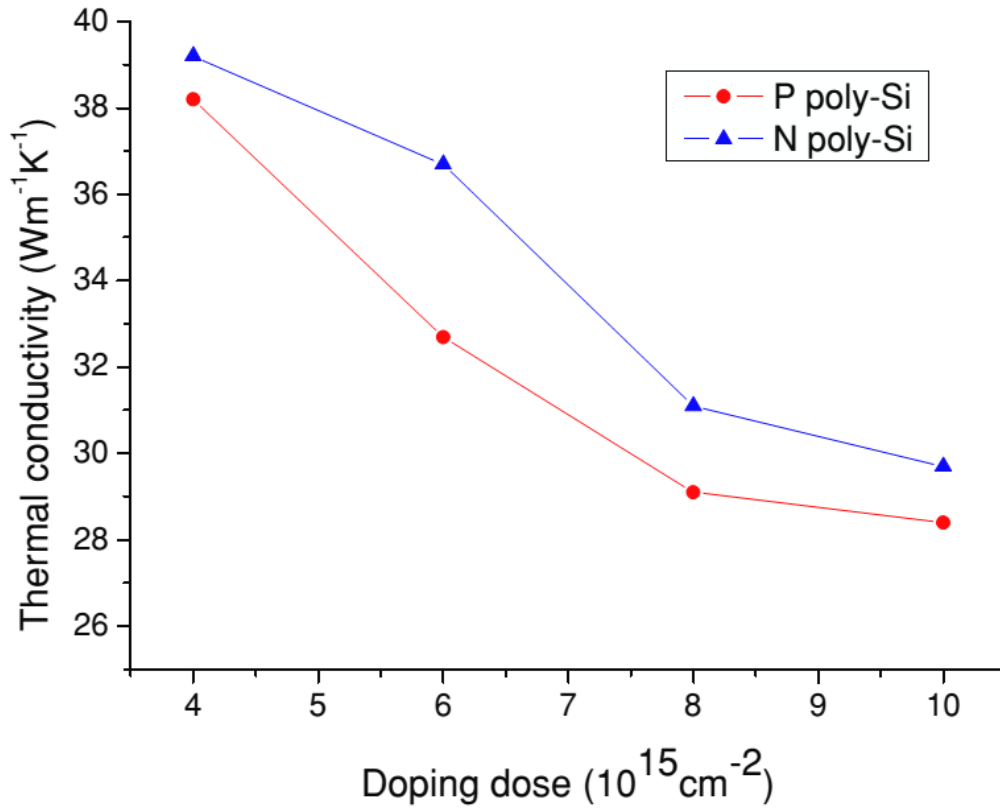
Figure 1.4. Thermal conductivity of poly-Si at different doping dosages [6].

The trends of electrical resistivity, Seebeck coefficient and thermal conductivity with different doping conditions are the same as described above: for both p-type and n-type poly-Si, a higher doping dosage leads to a lower electrical resistivity, Seebeck coefficient and thermal conductivity. The resulting *ZT* values are summarized in Figure 1.5. As shown in this figure, p-type poly-Si with the highest doping dosage has the highest *ZT*; n-type poly-Si, on the other hand, has the highest *ZT* with the lowest dosage. In Xie Jin's work, variation of the doping concentration is achieved by ion implantation, instead of *in situ* doped poly-Si. There might be some concern about whether different doping methods would affect the thermoelectric properties. However, no researchers are specifically studying differences in the thermoelectric

properties of in situ-doped poly-Si and ion-implanted poly-Si because the thermoelectric properties depend only on the doping concentration, regardless of the doping method.
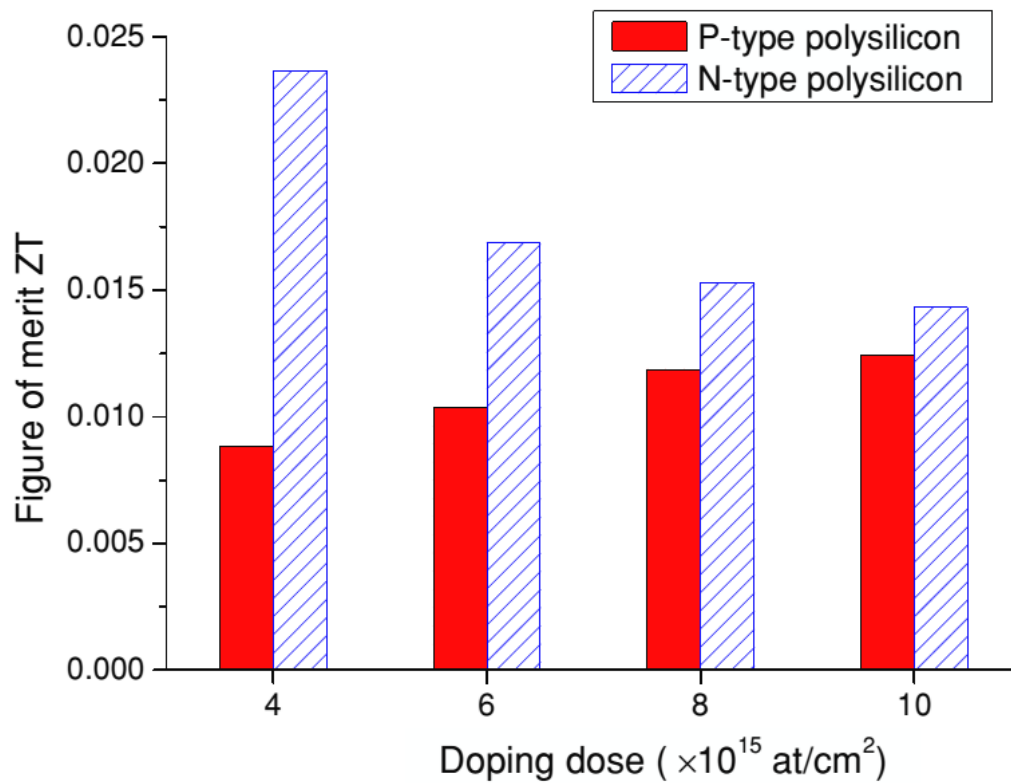
Figure 1.5. ZT for poly-Si doped with different dosages at T=300 K [6]. (at/cm^2 refers to number of atoms per square centimeter).

In addition to the optimization of the doping concentration of semiconductors, the development of doped alloys is also a popular method for increasing ZT.

One of the most widely used groups of highly effective non-CMOS compatible thermoelectric materials is bismuth (Bi) - or antimony (Sb)-related compounds or alloys, including Bi_xSb_y alloys, bismuth telluride (Bi_2Te_3), and lead telluride (PbTe).

For example, one of the most popular materials in this group, bismuth telluride (Bi_2Te_3), is a thermoelectric material; the Seebeck coefficient of this material depends on its composition. When the atomic presence of tellurium is approximately 60%, the Seebeck coefficient of bismuth telluride is as high as 230 µV/K, which means that it is a p-type thermoelectric material. The Seebeck coefficient decreases when the tellurium content increases; then, bismuth telluride becomes an n-type thermoelectric material, which has a negative Seebeck coefficient [63]. The best intrinsic bulk bismuth telluride has a relatively high *ZT* of approximately 0.8, as compared to semiconductors such as poly-Si, which have *ZT* values on the order of 10^{-2} or even lower. The reason why these alloys have such a high *ZT* is that they allow for the fine-tuning of the carrier concentration of alloys to achieve low thermal conductivity. This method does not affect the electrical resistivity when the lattice thermal conductivity is reduced. Thus, the thermal conductivities of such alloys are on the order of 1 W/mK, whereas the thermal conductivities of semiconductors are generally one order of magnitude greater than 1 W/mK. Doping can also be used to modify the thermoelectric properties of this group of materials. For instance, bismuth telluride can be doped with cesium to form $CsBi_4Te_6$, which has good thermoelectric properties at low temperatures (*ZT* is approximately 0.8 at 225 K) [64].

This group of materials also performs well at higher temperatures. The representatives are group IV telluride (Lead telluride (PbTe), Germanium telluride (GeTe), Silicon telluride (SiTe)) based materials, which can work at temperatures of 500 K to 900 K. Take PbTe as an example. Although the *ZT* of lead telluride is relatively low at room temperature (~0.001), this material has a fantastic performance (ZT>1) at 600 K [63].

Another example is AgSbTe$_2$-related alloys. One of these alloys is known as Te/Sb/Ge/Ag (TAGS). The formula of TAGS is (GeTe)$_{0.85}$(AgSbTe$_2$)$_{0.15}$. This material has been reported to have *ZT* values of greater than 1.2 at 400 K [65].

However, this group of materials is not CMOS compatible, thereby limiting its possibility for mass production. As a result, more researchers have become interested in the optimization of CMOS-compatible semiconductors using some novel technologies.

Recently, the development of nanostructures has brought new research into thermoelectric materials because of their significantly reduced lattice thermal conductivity. There are three general methods to achieve the low lattice thermal conductivity.

The first method is enhancing phonon scattering by utilizing methods of mass fluctuation scattering, enhancing phonon-boundary scattering in nanowires or enhancing phonon-grain-boundary scattering by minimizing the grain boundary size.

Akram I. Boukai [66] and his colleagues measured the thermoelectric properties of single-crystal Si nanowires. In Akram's study, the authors reported excellent thermoelectric performance from a single-component system of Si nanowires for cross-sectional areas of 10 nm$\times$20 nm and 20 nm$\times$20 nm. An approximately 100-fold improvement compared with bulk Si was achieved over a broad temperature range. The best *ZT* reported was approximately 1 at 200 K, which surpasses the *ZT* values of most alloys at the same range of temperature. Their structure for testing single-crystal Si nanowires, which has now become a standard setup for testing the thermoelectric properties of nanowires, is presented below.
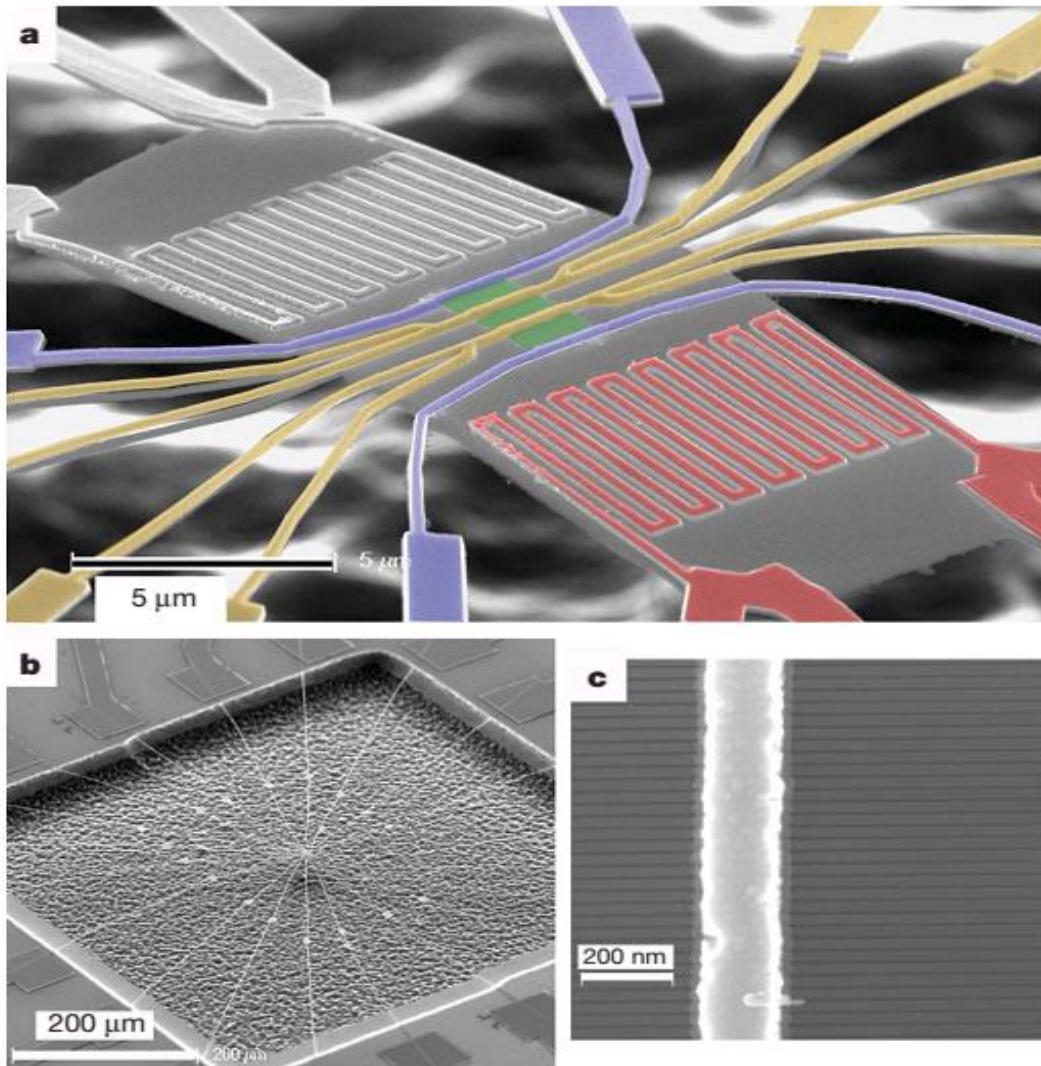
Figure 1.6. Scanning electron micrographs of the device used to quantify the thermopower and electrical and thermal conductivity of Si nanowire arrays. A) This false-color image of a suspended platform shows all electrical connections. The central green area is the Si nanowire array, which is not resolved at this magnification. The four-lead yellow electrodes are used for thermometry to quantify the temperature difference across the nanowire array. The thermal gradient is established using either of the two Joule heaters (the right-hand heater is colored red). The yellow and blue electrodes are combined to perform four-point electrical conductivity measurements on the nanowires. The grey region underneath the nanowires and electrodes is the 150-nm-thick SiO2 insulator that is sandwiched between the top Si(100) single-crystal film, from which the nanowires are fabricated, and the underlying Si wafer. The underlying Si wafer is etched back to suspend the measurement platform, thereby placing the background of this image out of focus. B) Low-resolution micrograph of the suspended platform. The electrical connections radiate outward and support the device. C) High-resolution image of an array of 20-nm-wide Si nanowires with a Pt electrode [66].
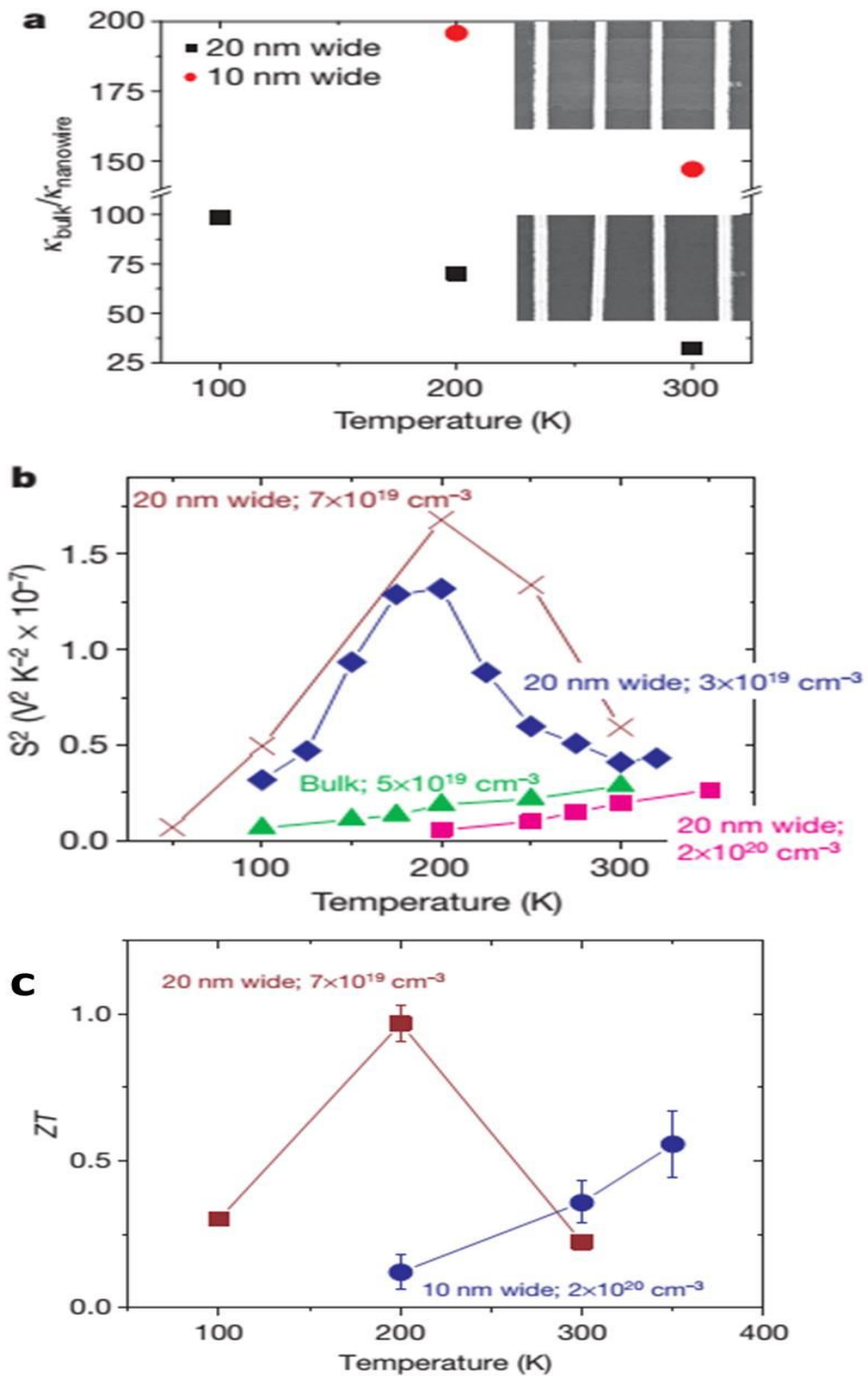
Figure 1.7. Experimental results of the thermoelectric properties of SiNW.(a) The temperature dependence of the thermal conductivity (b) The temperature dependence of S2 for 20-nm-wide Si nanowires at various p-type doping concentrations (c) Temperature dependence of ZT for two different groups of nanowires. [66].

The measurement results are shown in Figure 1.7. The main enhancement is a reduction in thermal conductivity. In this paper, the authors achieved a thermal conductivity of 0.76±0.15 w/mK for 10-nm-wide Si nanowires, which is less than the theoretical limit of 0.99 W/mK for bulk Si [66]. This result is possible because the small-dimension nanowire induces high phonon drag, which leads to a sharp reduction in the thermal conductivity.

In addition to Si nanowires, Jen-Kan Yu et al. reported a nanomesh structure that also has a relatively low thermal conductivity. Unfortunately, they did not measure other thermoelectric properties of the Si nanomesh, but its superior thermoelectric properties can also be ascertained.

Although nano-structured Si has great thermoelectric properties, it is a great challenge to fabricate such structures for mass production when it is desirable to incorporate Si nanowires or Si nanomeshes into thermopile design. As mentioned before, the thermoelectric characteristics of Si nanowires depend highly not only on their dimensions but also on the nanoscopic surface morphology [47-49]. In consideration of the strong demand for high ZT CMOS thermoelectric materials, in my study, I investigate nanometer-thick poly-Si to increase the ZT value based on phonon-boundary scattering. Subsequently, I present a scalable design for a thermopile that can be fabricated in a CMOS mass production line using the nanometer-thick poly-Si with optimized ZT and device configurations. This design will be discussed in details in Chapter IV.

1.2.2 Design and applications of thermoelectric devices

The capability of thermoelectric devices in mutual conversion of temperature differences and voltage biases allows them to be utilized for multiple applications. The applications can be classified into three categories, coolers, power generators and sensors. As introduced in the previous section, the thermoelectric effect can be generalized in two opposite behaviors, the Seebeck effect and Peltier effect. The Seebeck effect describes the conversion of temperature differences directly into electricity. This effect provides opportunities for utilizing thermopiles as self-power generators and various types of sensors. When two ends of a thermopile have different temperatures, there is a voltage output at these two ends, and the device becomes a self-powered generator or contact temperature sensor. If one end of the thermopile has a constant temperature but the other end receives external heat flow of IR radiation, the readout of the output voltage can reflect the intensity of the received heat flux or IR radiation. Then, the thermopile becomes a non-contact temperature sensor or IR detector. In contrast, the Peltier effect describes the heating or cooling effect at an electrified junction of two different conductors, based on which, many electrical coolers have been developed, resulting in a prosperous industry. The applications mentioned above are only some examples of thermopile-based applications. To give a comprehensive review of thermopile applications, I will provide a few examples that are representative in their functions and their working principles in the following text.

1.2.2.1 Thermoelectric cooling/heating system

As discussed above, a thermoelectric cooling/heating system creates a thermal

18

gradient between the junctions of two different materials based on the Peltier effect. By applying different current directions, the current in a thermopile can act as a heat pump, which can be used for either heating or cooling, with consumption of electrical energy. Therefore, thermoelectric cooling/heating systems are also called Peltier devices, Peltier heat pumps, solid-state refrigerators, or thermoelectric coolers [70]. Figure 1.8 shows the working principles of the thermoelectric cooler system.
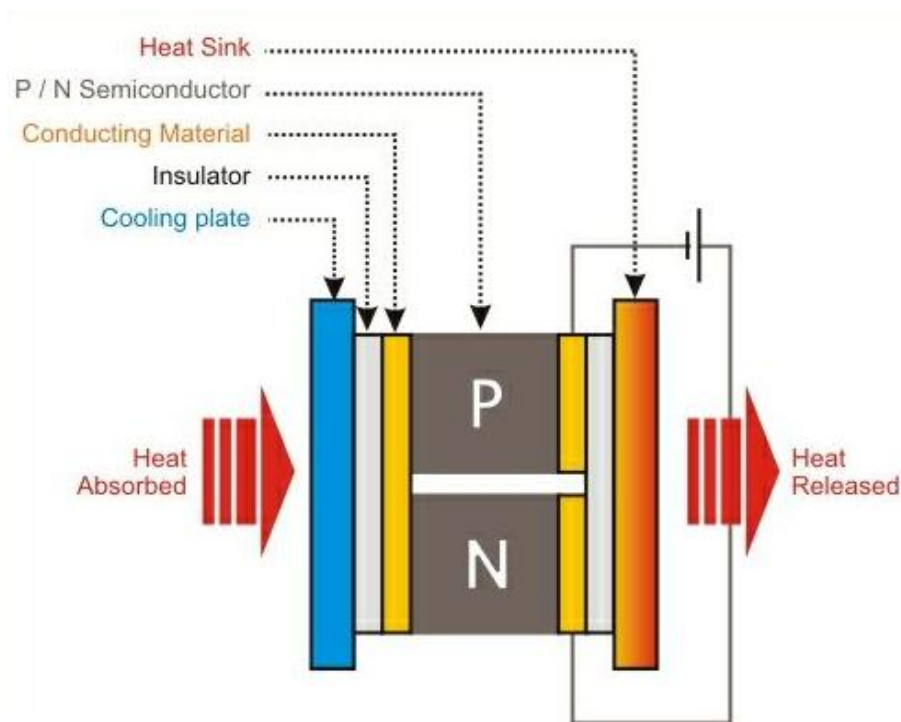
Figure 1.8. The working principles of a thermoelectric cooler system.

Peltier refrigerators are not commonly used as compared to refrigeration based on vapor compression. However, the advantage of Peltier refrigerators is that there is no need for moving parts or circulating liquid, which prevents significant risks of potential leaks, which makes them less prone to maintenance. In addition, their relatively small footprint and flexibility allow them to be used in a wide variety of fields. However, their relatively high power consumption and relatively low energy

efficiency of these devices has limited their applications. Figure 1.9 shows a complete thermoelectric cooling system; the part that is circled in red is the thermoelectric cooler module.

In this system, a voltage is applied to the free ends of the thermoelectric module, thereby resulting in a Direct Current (DC) flow of electricity through it. As a result, there is a temperature difference between the top and bottom of the thermoelectric module. As such, the large heat sink equipped with a fan removes the heat from the top of the module; subsequently the entire system acts as a heat pump that transfers the heat of the object from the bottom to the air.
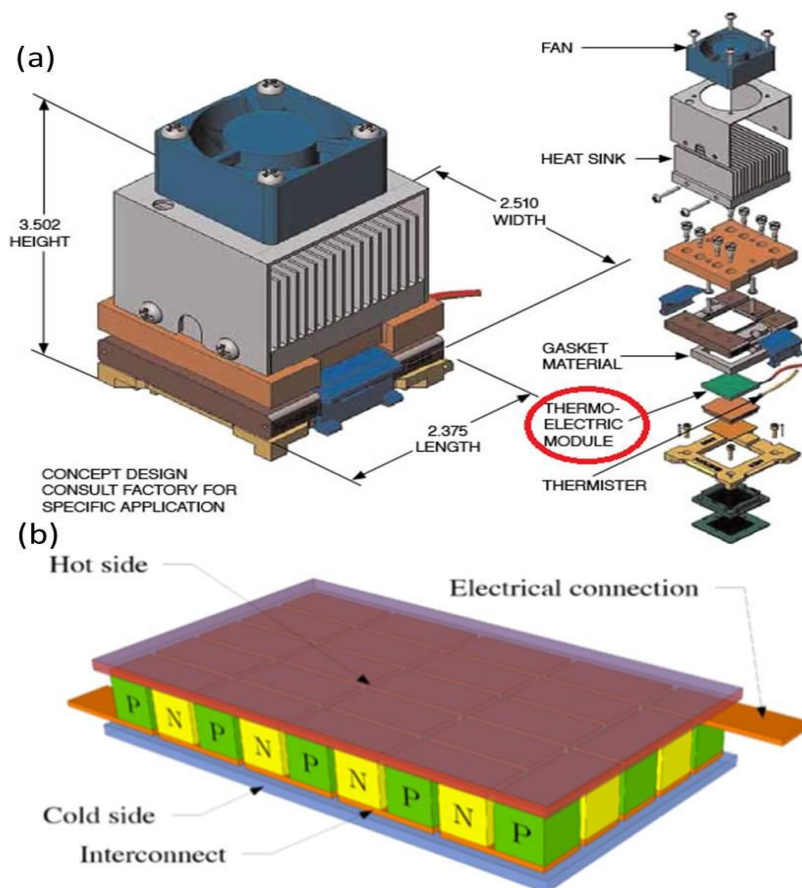
Figure 1.9. A schematic of (a) a complete thermoelectric cooling system and (b) a standard thermoelectric module [71,72].

1.2.2.2 Thermoelectric flow sensors

Flow sensors can be widely used in applications like environmental control, air conditioning, and industrial control; thermopile is one good candidate for flow sensors. Thermopile flow sensors are based on heat transfer from a heated part, typically a microheater, to the downstream end of the thermopile through a moving fluid. There will be a temperature difference between this end and the upstream end, creating a voltage output. The heat transfer through the moving fluid is contributed by two mechanisms: conduction and convection. Conduction is the transfer of heat between substances that are in direct contact with each other. How well conduction works is dependent on the nature of the fluid as well as the heat source; it is, however, irrelevant to the flow speed of the fluid. Convection, on the other hand, highly depends on the fluid speed.

Figure 1.10 shows a standard thermopile-based flow sensor. Part A in Figure 1.10(b) is the porous Si isolation layer. The thermal conductivity of porous Si is 1% of that of single-crystal Si, which makes it good at thermal isolation. Another effective method to achieve thermal isolation is to separate the microheater and thermopile structure. It is because that the thermal conductivity of air is even lower than that of porous Si. Part B in Figure 1.10(b) is the poly-Si part of the thermopile and microheater, and part C is the aluminum (Al) wire and electrical contact pads. In this example, Al and poly-Si form the thermopile structure.
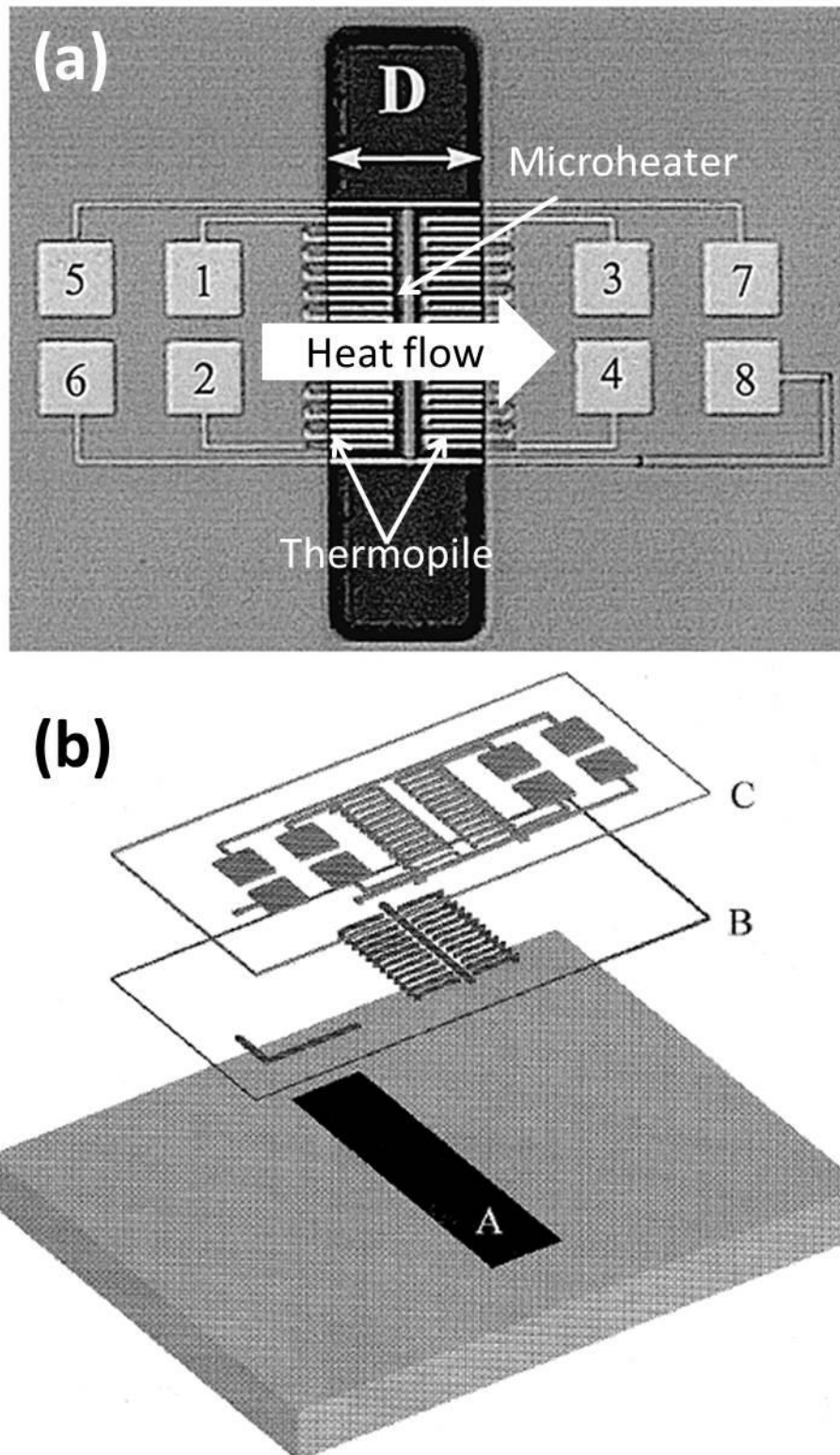
Figure 1.10. Example of a thermopile-based flow sensor. (a) Top view and (b) exploded view [73].

As shown in Figure 1.10, the microheater is heated by applying a bias on pads 5 and 6. Pads 7 and 8 are connected to a compensation resistor with the same characteristics as the microheater. The resistor is directly lying on the Si substrate without thermal isolation, such that the change in the resistance of the heater can be compensate. The heat flow shown in Figure 1.10 transfers the heat from the microheater to the right junction of the thermopile; as such, the left part is the cold junction and the right part is the hot junction. As the output voltage of the thermopile is proportional to the temperature difference, the temperature difference can be obtained straightforwardly. Furthermore, the temperature difference is proportional to the flow rate [73]. As a result, the flow rate is easy to obtain. Figure 1.11 shows the experimental results of the thermopile flow sensor shown in Figure 1.10 above.
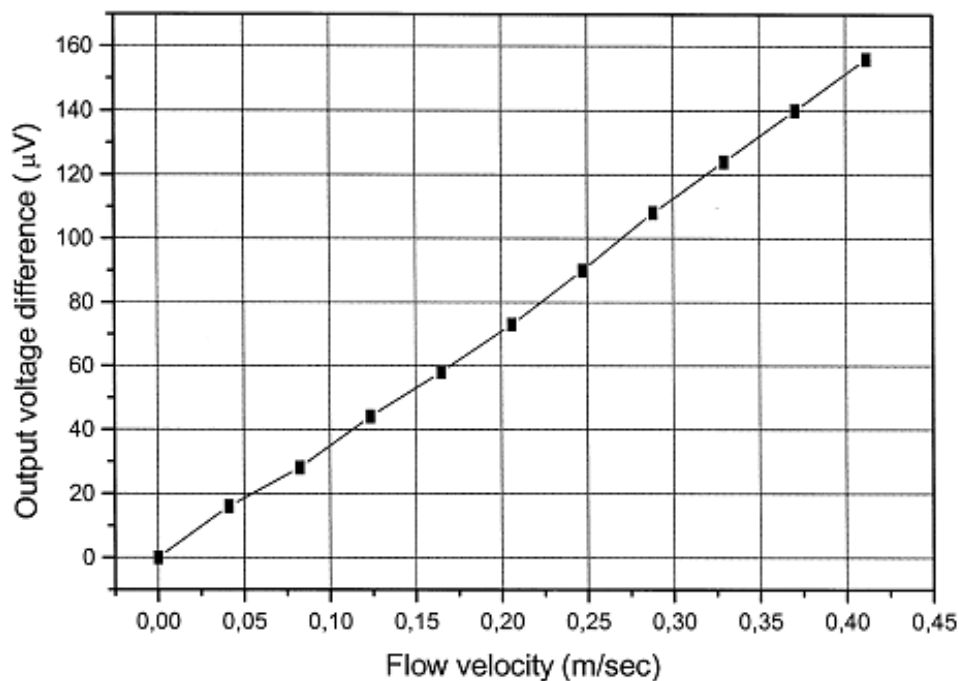
Figure 1.11. Experimental results of the thermopile flow sensor example shown described in the previous text [73].

1.2.2.3 Thermoelectric accelerometers

The thermopile accelerometer, which was first reported by Hiratsuka [74] in 1992, is a simple structure for converting acceleration into a temperature difference that is sensed by a thermopile. Compared with the capacitive accelerometer, the thermopile accelerometer has the advantage of avoiding the influence of electromagnetic interference [75]. A standard example of a thermopile accelerometer is shown in Figure 1.12.

As shown in Figure 1.12, a suspended microheater is placed at the center of the sensor, and a thermopile is placed on the both sides of the microheater. The structure looks similar to the flow sensor shown previously, but the sensing mechanism is slightly different. As for the other type of accelerometer, the thermopile accelerometer uses a seismic mass to sense the acceleration. In the design of a thermopile accelerometer, the microheater acts as the seismic mass. When acceleration is applied to the device, the suspended microheater moves closer to one of the ends of the thermopile. As such, the end of thermopile that is closer to the heater will have a higher temperature than the other end. As a result, the acceleration can be calculated by measuring the voltage generated by the thermopile.
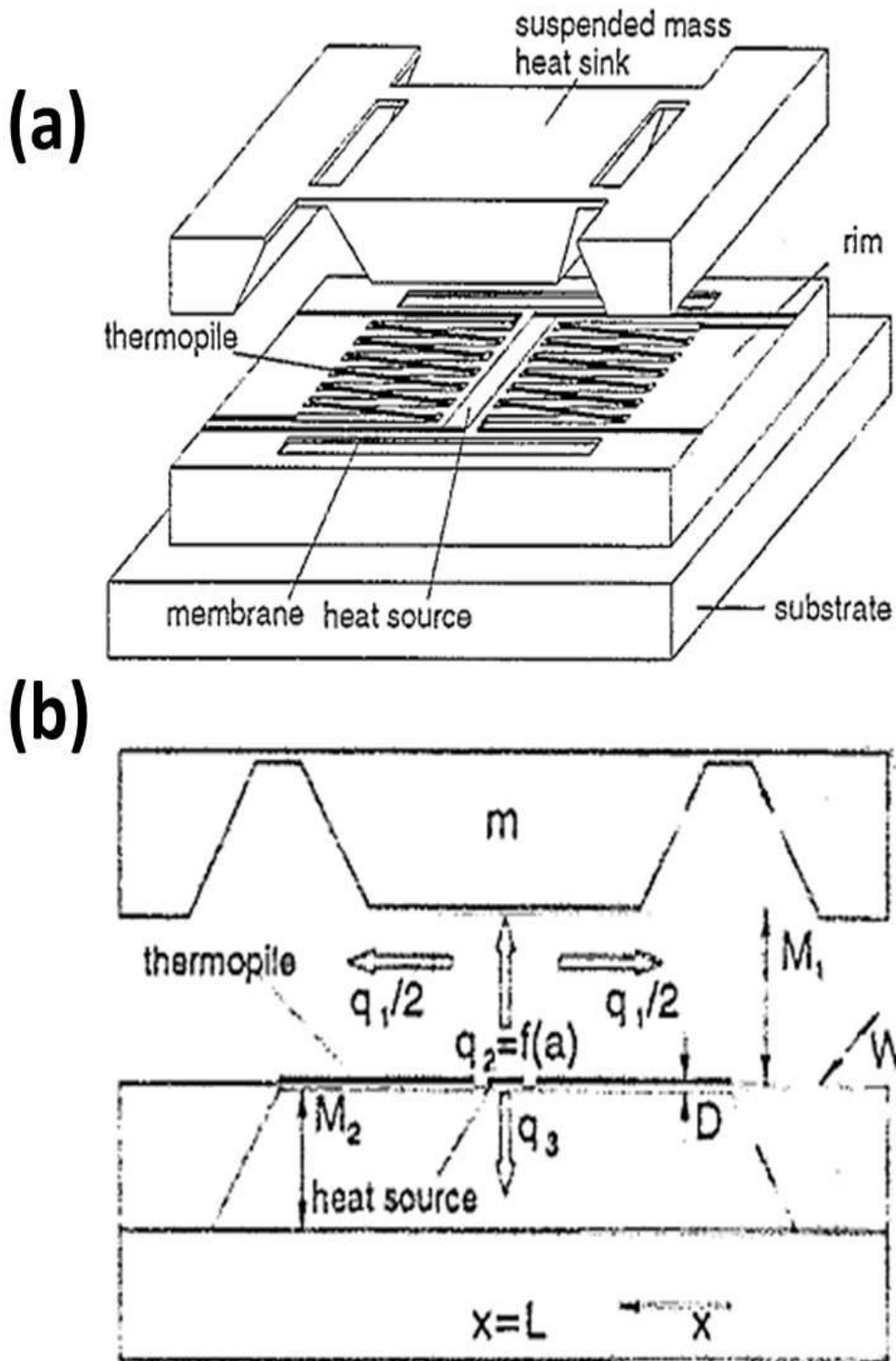
Figure 1.12. Schematic drawing of an example of thermopile accelerometer. (a) 3D view, (b) cross-sectional view and the presentation of heat flow [76].

Because the temperature difference is proportional to the displacement of the microheater until the acceleration is sufficiently large that the microheater contacts the thermopile. There is nonlinearity once contact occurs. Figure 1.12 demonstrates this phenomenon. When the acceleration is less than 0.4 times the acceleration due to gravity, this accelerometer has good linearity. Beyond this threshold, the microheater will have contacted with the thermopile, which leads to nonlinearity.
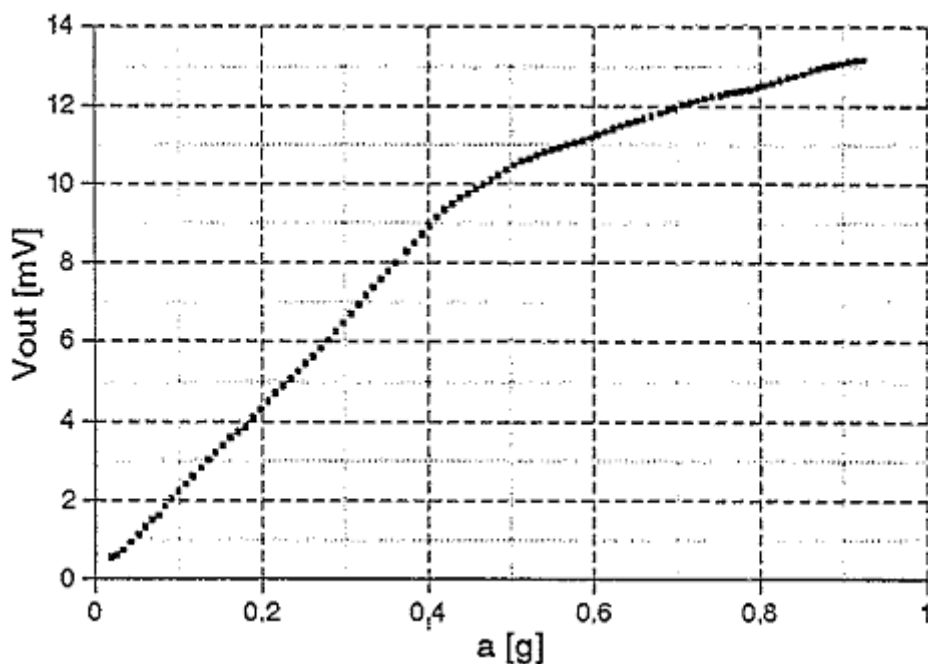
Figure 1.13. Experimental results of the example of thermopile accelerometer [76].

1.2.2.4 Thermoelectric power generator

Currently, the development of wireless wearable and implanted electrical devices indicates the high demand for light, portable self-power generators with high reliability and long life-cycles. Thermopile is one of the best solutions for these applications. As compared to traditional portable power supply devices, e.g., batteries and mechanical energy harvesters, thermopile power generators are more compact and

have nearly unlimited life-cycles. Thermopile power generators also make use of the Seebeck effect. To use a thermopile as a power generator, the heat path through the device needs to be optimized to ensure that one end of the thermopile is attached to heated object, such as a human body, to serve as the hot junction, whereas the other end needs to be left alone to serve as the cold junction. Figure 1.14 shows an example of a thermopile power generator.
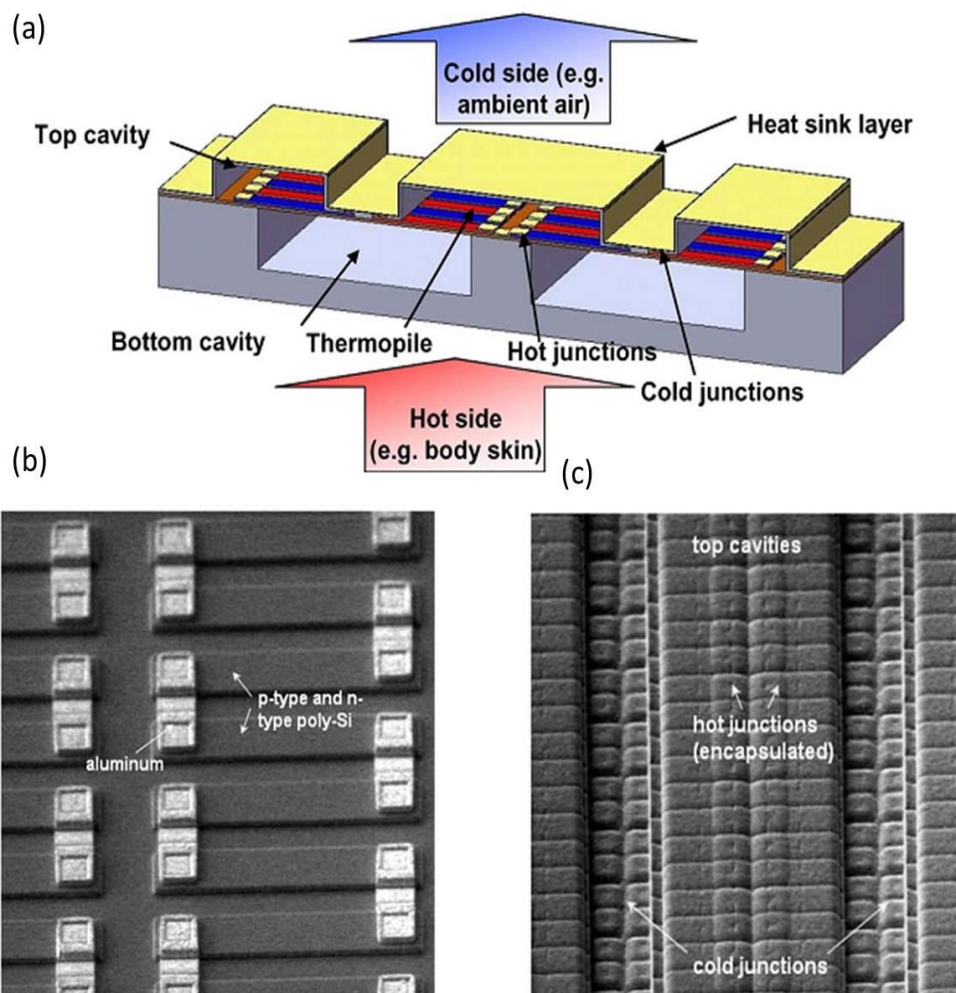
Figure 1.14. Example of a thermopile power generator. (a) 3D schematic drawing, (b) scanning electron microscope (SEM) image of the thermopile power generator before vacuum sealing, and (c) SEM image of the thermopile power generator after vacuum sealing [77].

Xie Jin and his colleagues came up with the thermopile power generator design shown in the above figure. Because thermopile power generators are used in wearable devices, the thickness of the entire device should be minimized to ensure the flexibility of the device. As such, the length of the heat path is limited. In the design developed by Xie Jin, the combination of a lateral thermopile structure and thin-film vacuum encapsulation provides a solution for this problem because the heat path is not limited by the device thickness, as the lateral structure and vacuum sealing provide great thermal isolation. However, a problem associated with thermopile power generators remains unresolved. Because thermopile power generators typically contain a large number of thermocouples to provide sufficient voltage output, the high internal electrical resistance of thermopile power generators is always a problem [77]. For example, in Xie Jin's design, the output voltage of the power generator is extremely high (16.7 V), but the internal electrical resistance is in the range of 23-52.8 MΩ; this limits the output power of the device, which is only 0.052 μW/cm^{-2}K^{-2}. As a result, balance between the output voltage and internal electrical resistance becomes an important consideration in thermopile power generator design.

1.2.2.5 Thermoelectric IR sensors and related applications

Apart from all of the applications introduced above, thermopiles have been widely used in IR detection and numerous applications that are related to IR radiation. My research is related to this field.

Since 1800, when Herschel developed the very first IR detector by using a glass liquid thermometer [78], various IR sensors have been developed. The IR sensors are categorized into two groups: thermal IR sensor and quantum IR sensor. Thermal IR

sensors mainly rely on MEMS technology. Thus we focus on thermal IR sensors in this section. Table 3.1 shows the comparison among four major thermal IR sensors types [79].

Table 1.2. Features of IR sensors[79].

Type		Operation principle	Operation temperature	Sensitivity	Spectral response	Response time	FPA structure	Typical materials
Thermal	Ferroelectric	Temperature dependence of spontaneous polarization (pyroelectric) Temperature dependence of dielectric constant (dielectric bolometer)	Room temperature	Low	Depending on absorber	Slow	Hybrid	BST, PST, PZT, PVDF
	Resistance bolometer	Temperature dependence of resistance						VO_x, a-Si
	Thermoelectric	Seebeck effect					Monolithic	Al/poly-Si n poly-Si/p poly-Si
	Diode	Temperature dependence of I–V characteristic						Si

IR radiation can be detected by thermal IR sensor because the absorbed IR radiation makes a temperature change to the suspended absorber membrane of IR radiation sensor. The conversion from the induced temperature change to electrical signal change could be explained by several different sensing mechanisms. One of the most representative IR sensors is the thermopile IR sensor that is used in this work. By connecting two thermoelectric materials with different Seebeck coefficients, a thermocouple can be formed. A series of connected thermocouples in micrometer scale is called a thermopile. Since the thermopile is a passive sensor and can generate thermoelectric voltage due to received IR radiation energy; it has a great advantage over the other kinds of IR sensors. Unlike the resistive bolometer based IR sensor, thermopile does not face the self-heating issue which demands extra effort in readout circuits.

In comparison with the applications stated in previous sections, the major difference in thermopiles used for IR-related applications is the existence of integrated IR absorber [80, 81]. In a thermopile IR sensor, the absorber layer absorbs the IR

radiation from the IR source and turns the radiation power into heat, which causes the temperature of the hot junction to increase. Because of the suspended thermopile structure, the hot junction and cold junction are thermally isolated. Thermal isolation leads to a relatively high temperature difference between these two junctions. Because of the Seebeck effect, as discussed above, the thermopile will generate an output voltage without any applied voltage bias.

In recent years, IR sensors fabricated with CMOS-compatible processes are widely used for various applications [82-84)]. CMOS-compatible IR sensors have relatively small footprints, lower weights and faster response speeds as compared to traditional sensors. In addition, these IR sensors can be monolithically integrated with readout ICs for further signal amplification or other processing [85, 86)]. In addition to the traditional applications of IR sensors, e.g., imaging, target surveillance and temperature monitoring, research of substance detectors using wavelength-selective sensing to analyze specific molecular bonds has increased [87,88]. Various general applications of thermopile IR detectors are discussed below.

Non-contact or remote temperature sensing is the one of the main applications of micromachined thermopiles. This application can be used widely in areas ranging from everyday life to industry. In home applications, non-contact thermopile IR sensors can be used in control units for microwave ovens to monitor cooking temperatures, control units for tumble dryers to detect when laundry is dry, and control units in toasters and stoves to reduce the risk of overheating. In the area of medicine and health, such sensors can be used in body temperature monitoring units, such as for respiration and non-contact fever thermometers. In addition, industrial

applications such as process liquid/gas flow detection in pipes and heat flow detectors also have great needs for thermopile non-contact temperature sensors. Thermopile remote temperature sensors often contain one single thermopile detector only because they do not need to provide an entire thermal image. In addition, a thermal resistor must be integrated into the sensor as a temperature reference such that the temperature difference measured by the thermopile can be translated into an absolute temperature. Figure 1.15 shows an example of a thermopile remote temperature sensor [89].

As shown in this figure, a black IR absorber is incorporated onto the thermopile structure. The thermal resistor is placed on the back of the thermopile, separated from the thermopile with an insulation layer to avoid short-circuiting. A protection layer covers the thermal resistor, thereby preventing damage that could arise from further activities, such as handling or mounting.
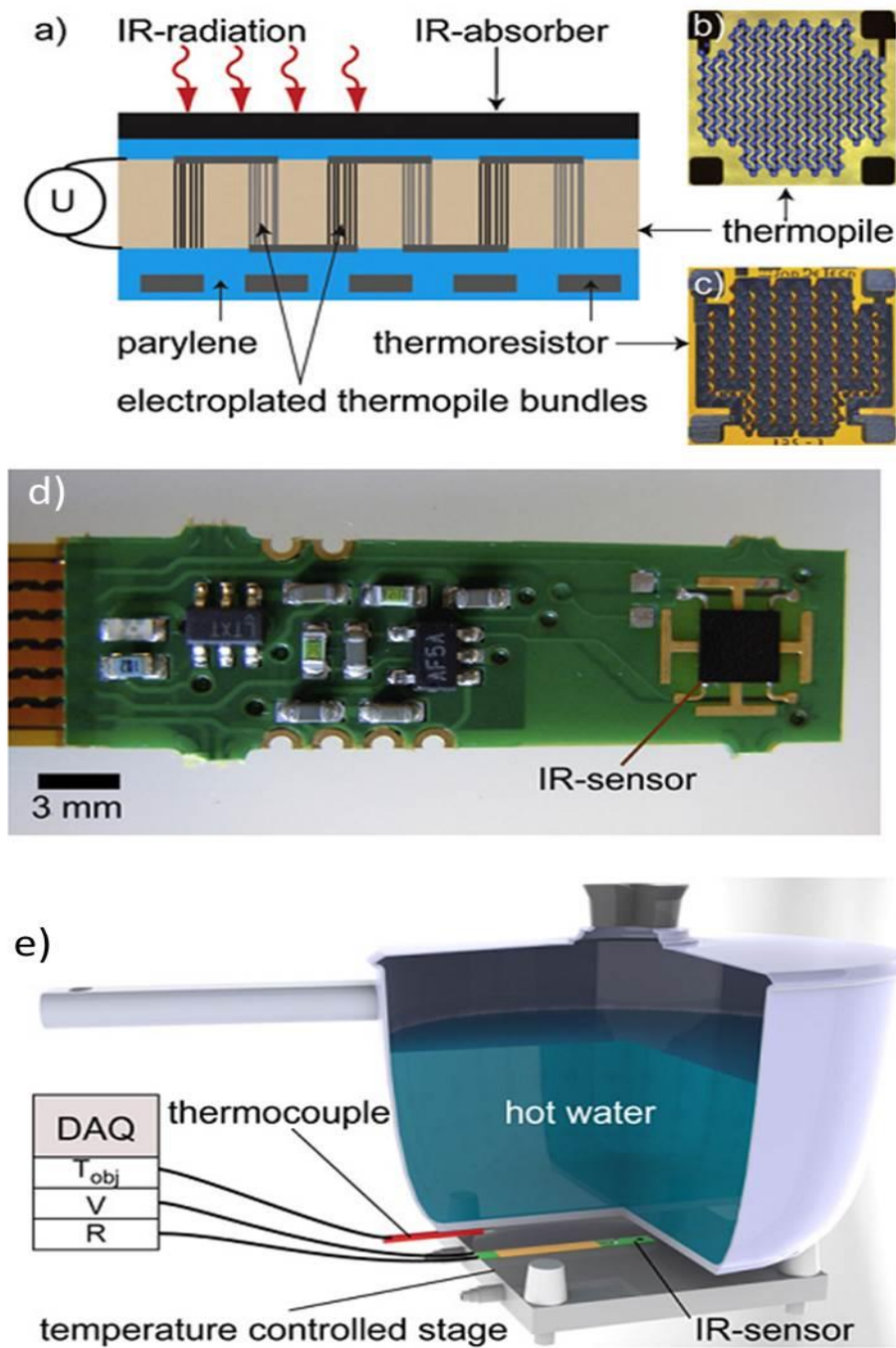
Figure 1.15. Example of a thermopile remote temperature sensor. (a) Schematic drawing of the cross-section of the IR sensor, which consists of a thermopile and an integrated thermal resistor. (b) Optical image of the thermopile, which consists of bundles of submicron strands connected in series to form a long chain. (c) The thermal resistor is deposited on the back of the IR sensor, where connection pads for both the thermal resistor and thermopile are located. (d) The IR sensor mounted on a PCB card with the amplification circuit. (e) Testing setup to show its applications [89].

Another popular application of thermopile IR sensors is IR imaging arrays, which will be the focus of my future work. IR image sensing has a large market with infinite possibility. Thermopile IR imaging sensors can be applied in many fields, such as proximity sensors for entrance detection, human body detection systems, fire detection systems, wake-up circuits for electronic door locks, and motion detectors. Although the sensitivity of thermopile IR sensors is typically less than that of traditional resistive-type IR bolometers, thermopile IR sensors also have a big market. Research about resistive-type IR bolometers has already reached its bottleneck. The size of each bolometer pixel has been reduced to the IR diffractive limitation, e.g., 15 μm for long-wavelength IR radiation, and research into the materials used to build bolometers has been paused for some time. As a result, the spatial resolution and sensitivity of resistive-type bolometers have reached their limits. In contrast, thermopile IR sensors do not have such limitations. Currently, the size of typical thermopile IR imaging sensors is approximately 200-300 μm, which means that there is a significant possibility for the spatial resolution of thermopile IR imaging sensors to be improved. The potential of thermopile IR image sensors also lies in the great progress of thermoelectric materials. Many thermoelectric materials with great performance but that are not CMOS compatible, which were introduced in the previous section, have not been applied to build the thermopile IR sensors because of some limitations of the fabrication process. However, there are great advantages and potential to use such types of materials to build thermopile IR imaging sensors.

Another application of gas sensors based on the Lambert–Beer law of absorption has opened a new door for thermopile IR sensing.

In physical optics and transport theory, the Beer-Lambert law also known as Beer's law, the Lambert–Beer law, or the Beer-Lambert-Bouguer law (named after August Beer, Johann Heinrich Lambert, and Pierre Bouguer) is related to the attenuation of light based on the properties of the material through which a substance, such as light, neutrons or host rarefied gases, is traveling. Gas sensors based on this concept are widely used for the detection of oxocarbon (CO_x) [90], with applications such as fire alarms, monitoring of air pollution and providing essential information regarding a patient's condition. Figure 1.16 shows an example of the absorption spectrum of a primary alcohol.
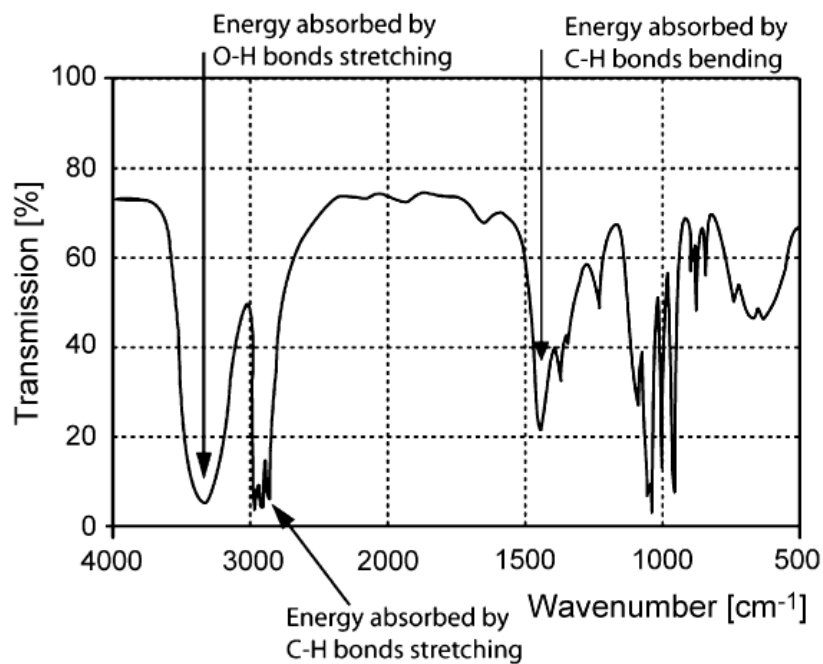
Figure 1.16. IR absorption spectrum of a primary alcohol (1-propanol) [91].

The technology that detects gases based on their unique IR absorption is called non-dispersive infrared (NDIR) gas detection. A typical schematic of an integrated NDIR gas detection system is shown in Figure 1.17. The entire system comprises four key parts: an IR emitter, a tube for confining the optical path, a bandpass IR filter and

an IR detector. The characteristics of the IR emitter spectrum can be predicted using the blackbody emission theory. The emission spectrum of a blackbody is determined by the temperature of the blackbody [92]. IR radiation that passes through the optical path, which is filled with the gas to be measured, will be absorbed if the photon energy of the particular wavelength corresponds to the energy of quantized vibrations or rotations of the gas molecules. The IR bandpass filter can be tuned to filter out and transmit the desired wavelength, which is in line with the absorption wavelength of the gas. Therefore, the IR radiation contains only the information of the wavelength of specific gas absorption once it passes through the filter. The intensity of the IR radiation can be quantitatively detected by an IR radiation sensor [93]. The output signal of the IR sensor decreases with increases in the gas concentration. The relationship between the gas concentration and the output of the IR sensor can be calculated based on the Lambert-Beer law [94].
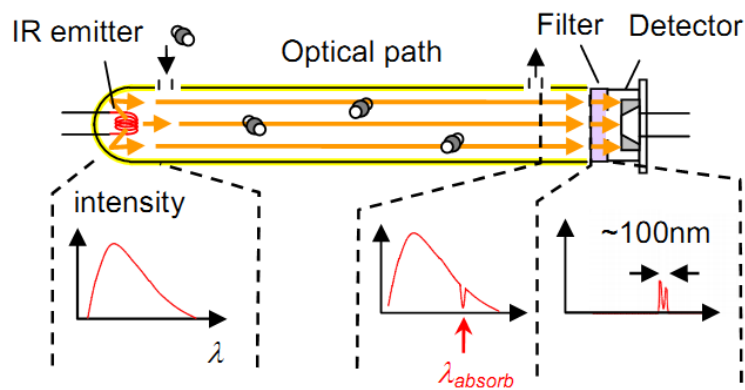
Figure 1.17. Schematic drawing of NDIR gas sensor [94].

For this application, the sensors must work in some rather harsh environments, e.g., high temperature up to 300°C for oil gas detection. However, most IR sensors, especially quantum sensors cannot work properly at high temperatures [92(95]. Therefore, in my study, one of the objectives is to explore the characteristic of

thermopile-based IR sensors at high temperature for potential applications in harsh environments.

1.3 Summary of the thesis

In this thesis, I mainly focused on four areas of the development of MEMS technology-based thermopiles and IR-related applications. First, I optimized the structure design of thermopiles by proposing a stacked double layer (SDL) thermopile with a 100% performance increase relative to conventional coplanar thermopiles. Secondly, I further developed the thermopile wavelength-selective IR sensor to demonstrate one of the applications of MEMS technology-based thermopiles. Thirdly, I studied the nanometer-thick poly-Si film. My work demonstrated the superior thermoelectric properties of nanometer-thick poly-Si. Finally, I studied the use of various IR absorbers on thermopiles to explore more applications of thermopiles. The contents of the following chapters are described below.

Chapter II describes the design, fabrication and characterization of the SDL thermopile structure, describing the working principles and advantages of this novel design.

Chapter III presents a use of the SDL thermopile as a single IR sensor integrated with a wavelength-selective IR absorber. To study the performance of the thermopile IR sensor at high temperatures, an experiment that determines the dependence of the temperature was also conducted, as documented in this chapter.

Chapter IV proposes a nanometer-thick poly-Si layer with enhanced phonon-boundary scattering that can be used as an effective thermoelectric material. A theoretical

analysis and characterization of the material were conducted and presented. Furthermore, the design, fabrication and characterization of a thermopile IR sensor constructed with a nanometer-thick poly-Si layer are provided to demonstrate the advantages of this material.

Chapter V examines two different types of IR absorbers with two different concepts of IR absorber design. The first is a broadband IR absorber that uses mixed SU-8 and carbon nanotubes (CNTs). The other is a wavelength-selective interferometric absorber that only absorbs the IR radiation with selected absorption peak.

Reference

[1] Wood R A, Han C J, Kruse P W. Integrated uncooled infrared detector imaging arrays, Solid-State Sensor and Actuator Workshop, 1992. 5th Technical Digest., IEEE. IEEE, 1992: 132-135.

[2] Wood R A. Uncooled thermal imaging with monolithic silicon focal planes, SPIE's 1993 International Symposium on Optics, Imaging, and Instrumentation. International Society for Optics and Photonics, 1993: 322-329.

[3] Xu D, Xiong B, Wang Y, et al. Robust array-composite micromachined thermopile IR detector by CMOS technology. Electron Device Letters, IEEE, 2011, 32(12): 1761-1763.

[4] Wu H, Emadi A, Sarro P M, et al. A surface micromachined thermopile detector array with an interference-based absorber. Journal of Micromechanics and Microengineering, 2011, 21(7): 074009.

[5] Du C H, Lee C K. Optimization criteria of CMOS-compatible thermopile sensors, Asia Pacific Symposium on Microelectronics and MEMS. International Society for Optics and Photonics, 1999: 116-126.

[6] Xie J, Lee C, Wang M F, et al. Microstructures for characterization of seebeck coefficient of doped polysilicon films. Microsystem technologies, 2011, 17(1): 77-83.

[7] Leonov V, Torfs T, Fiorini P, et al. Thermoelectric converters of human warmth for self-powered wireless sensor nodes. Sensors Journal, IEEE, 2007, 7(5): 650-657..

[8] Leonov V, Torfs T, Fiorini P, et al. Thermoelectric converters of human warmth for self-powered wireless sensor nodes. Sensors Journal, IEEE, 2007, 7(5): 650-657.

[9] Xu D, Xiong B, Wang Y. Modeling of front-etched micromachined thermopile IR detector by CMOS technology. Microelectromechanical Systems, Journal of, 2010, 19(6): 1331-1340.

[10] Suman S, Gaitan M, Joshi Y, et al. Wire-bonding process monitoring using thermopile temperature sensor. Advanced Packaging, IEEE Transactions on, 2005, 28(4): 685-693.

[11] Du C H, Lee C. Characterization of thermopile based on complementary metal-oxide-semiconductor (CMOS) materials and post CMOS micromachining. Japanese journal of applied physics, 2002, 41(6S): 4340.

[12] Du C H, Lee C K. Investigation of thermopile using CMOS compatible process

and front-side Si bulk etching, Micromachining and Microfabrication. International Society for Optics and Photonics, 2000: 168-178.

[13] Du C H, Lee C K. Optimization criteria of CMOS-compatible thermopile sensors, Asia Pacific Symposium on Microelectronics and MEMS. International Society for Optics and Photonics, 1999: 116-126.

[14] Zhou, H., Kropelnicki, P., Lee, C., CMOS Compatible Mid-infrared Wavelength-Selective Thermopile for High Temperature Applications J. Microelectro mech. Syst., 2014, 24(1): 144 - 154.

[15] Nguyen N T. Micromachined flow sensors—a review. Flow measurement and Instrumentation, 1997, 8(1): 7-16.

[16] [16] Hagleitner C, Hierlemann A, Lange D, et al. Smart single-chip gas sensor microsystem. Nature, 2001, 414(6861): 293-296.

[17] Dauderstädt U A, De Vries P H S, Hiratsuka R, et al. Silicon accelerometer based on thermopiles. Sensors and actuators A: Physical, 1995, 46(1): 201-204.

[18] Milanović V, Bowen E, Zaghloul M E, et al. Micromachined convective accelerometers in standard integrated circuits technology. Applied Physics Letters, 2000, 76(4): 508-510.

[19] Klonz M. Ac-dc transfer difference of the PTB multijunction thermal converter in the frequency range from 10 Hz to 100 kHz. Instrumentation and Measurement, IEEE Transactions on, 1987, 1001(2): 320-329.

[20] DiSalvo F J. Thermoelectric cooling and power generation. Science, 1999, 285(5428): 703-706.

[21] Li J F, Liu W S, Zhao L D, et al. High-performance nanostructured thermoelectric materials. NPG Asia Materials, 2010, 2(4): 152-158.

[22] Li J F, Liu W S, Zhao L D, et al. High-performance nanostructured thermoelectric materials. NPG Asia Materials, 2010, 2(4): 152-158.

[23] Harman T C, Taylor P J, Walsh M P, et al. Quantum dot superlattice thermoelectric materials and devices. Science, 2002, 297(5590): 2229-2232.

[24] Snyder G J, Toberer E S. Complex thermoelectric materials. Nature materials, 2008, 7(2): 105-114..

[25] Tritt T M, Subramanian M A. Thermoelectric materials, phenomena, and applications: a bird's eye view. MRS bulletin, 2006, 31(03): 188-198.

[26] Cooling H. Generating Power, and Recovering Waste Heat with Thermoelectric Systems Bell, Lon E. Science (Washington, DC, United States), 2008, 321(5895): 1457-1461.

[27] Xie J, Lee C, Wang M F, et al. Microstructures for characterization of seebeck coefficient of doped polysilicon films. Microsystem technologies, 2011, 17(1): 77-83.

[28] Xie J, Lee C, Feng H. Design, fabrication, and characterization of CMOS MEMS-based thermoelectric power generators. Microelectromechanical Systems, Journal of, 2010, 19(2): 317-324.

[29] Xie J, Lee C, Wang M F, et al. Characterization of heavily doped polysilicon films for CMOS-MEMS thermoelectric power generators. Journal of Micromechanics and Microengineering, 2009, 19(12): 125029.

[30] Glatz W, Muntwyler S, Hierold C. Optimization and fabrication of thick flexible polymer based micro thermoelectric generator. Sensors and Actuators A: Physical, 2006, 132(1): 337-345.

[31] Yousef H, Hjort K, Lindeberg M. Vertical thermopiles embedded in a polyimide-based flexible printed circuit board. Microelectromechanical Systems, Journal of, 2007, 16(6): 1341-1348.

[32] Lan Y, Minnich A J, Chen G, et al. Enhancement of Thermoelectric Figure‐of‐Merit by a Bulk Nanostructuring Approach. Advanced Functional Materials, 2010, 20(3): 357-376.

[33] Pei Y, Lensch‐Falk J, Toberer E S, et al. High thermoelectric performance in PbTe due to large nanoscale Ag2Te precipitates and La doping. Advanced Functional Materials, 2011, 21(2): 241-249.

[34] Girard S N, Schmidt‐Rohr K, Chasapis T C, et al. Analysis of Phase Separation in High Performance PbTe–PbS Thermoelectric Materials. Advanced Functional Materials, 2013, 23(6): 747-757.

[35] Hu L, Zhu T, Liu X, et al. Point Defect Engineering of High‐Performance Bismuth‐Telluride‐Based Thermoelectric Materials. Advanced Functional Materials, 2014, 24(33): 5211-5218.

[36] Peranio N, Leister E, Töllner W, et al. Stoichiometry controlled, single‐crystalline Bi_2Te_3 nanowires for transport in the basal plane. Advanced Functional Materials, 2012, 22(1): 151-156.

[37] Kastbjerg S, Bindzus N, Søndergaard M, et al. Direct evidence of cation disorder in thermoelectric lead chalcogenides PbTe and PbS[J]. Advanced Functional Materials, 2013, 23(44): 5477-5483.

[38] Kastbjerg S, Bindzus N, Søndergaard M, et al. Direct evidence of cation disorder in thermoelectric lead chalcogenides PbTe and PbS. Advanced Functional Materials, 2013, 23(44): 5477-5483.

[39] Cook B A, Kramer M J, Harringa J L, et al. Analysis of Nanostructuring in High Figure‐of‐Merit Ag1–xPbmSbTe2+ m Thermoelectric Materials. Advanced Functional Materials, 2009, 19(8): 1254-1259.

[40] Bux S K, Blair R G, Gogna P K, et al. Nanostructured bulk silicon as an effective thermoelectric material. Advanced Functional Materials, 2009, 19(15): 2445-2452.

[41] Medlin D L, Snyder G J. Interfaces in bulk thermoelectric materials: a review for current opinion in colloid and interface science. Current Opinion in Colloid & Interface Science, 2009, 14(4): 226-235.

[42] C. Dames, G. Chen, in Thermoelectrics Handbook: Macro to Nano (ed. Rowe, D. M.) CRC Press, Cleveland 2006, Ch. 42.

[43] Ju Y S, Goodson K E. Phonon scattering in silicon films with thickness of order 100 nm. Applied Physics Letters, 1999, 74(20): 3005-3007.

[44] Boukai A I, Bunimovich Y, Tahir-Kheli J, et al. Silicon nanowires as efficient thermoelectric materials. Nature, 2008, 451(7175): 168-171.

[45] Yu J K, Mitrovic S, Tham D, et al. Reduction of thermal conductivity in phononic

nanomesh structures. Nature nanotechnology, 2010, 5(10): 718-721.

[46] Tang J, Wang H T, Lee D H, et al. Holey silicon as an efficient thermoelectric material. Nano letters, 2010, 10(10): 4279-4283.

[47] Hochbaum A I, Chen R, Delgado R D, et al. Enhanced thermoelectric performance of rough silicon nanowires. Nature, 2008, 451(7175): 163-167.

[48] Li D, Wu Y, Kim P, et al. Thermal conductivity of individual silicon nanowires. Applied Physics Letters, 2003, 83(14): 2934-2936.

[49] Chen R, Hochbaum A I, Murphy P, et al. Thermal conductance of thin silicon nanowires. Physical review letters, 2008, 101(10): 105501.

[50] Liu W, Asheghi M. Thermal conductivity measurements of ultra-thin single crystal silicon layers. Journal of heat transfer, 2006, 128(1): 75-83.

[51] Völklein F, Baltes H. Optimization tool for the performance parameters of thermoelectric microsensors[J]. Sensors and Actuators A: Physical, 1993, 36(1): 65-71.

[52] Völklein F, Baltes H. Optimization tool for the performance parameters of thermoelectric microsensors. Sensors and Actuators A: Physical, 1993, 36(1): 65-71.

[53] Uma S, McConnell A D, Asheghi M, et al. Temperature-dependent thermal conductivity of undoped polycrystalline silicon layers. International Journal of Thermophysics, 2001, 22(2): 605-616.

[54] Mandurah M M, Saraswat K C, Helms C R, et al. Dopant segregation in

polycrystalline silicon. Journal of applied physics, 1980, 51(11): 5755-5763.

[55] Seebeck T J. Ueber die magnetische Polarisation der Metalle und Erze durch Temperaturdifferenz. Annalen der Physik, 1826, 82(3): 253-286.

[56] Peltier, J.C., Nouvelles experiences sur lacaloriecete des courans electriques. Ann. Chem. LVI, 1834, 371-387

[57] Slack G A. The thermal conductivity of nonmetallic crystals. Solid state physics, 1979, 34: 1-71.

[58] Cutler M, Leavy J F, Fitzpatrick R L. Electronic transport in semimetallic cerium sulfide. Physical Review, 1964, 133(4A): A1143.

[59] Alam H, Ramakrishna S. A review on the enhancement of figure of merit from bulk to nano-thermoelectric materials. Nano Energy, 2013, 2(2): 190-212.

[60] Snyder G J, Toberer E S. Complex thermoelectric materials. Nature materials, 2008, 7(2): 105-114.

[61] Mahan G D, Sofo J O. The best thermoelectric. Proceedings of the National Academy of Sciences, 1996, 93(15): 7436-7439.

[62] Shakouri A, Li S. Thermoelectric power factor for electrically conductive polymers, Thermoelectrics, 1999. Eighteenth International Conference on. IEEE, 1999: 402-406.

[63] Yang B, Ahuja H, Tran T N. Review Article: Thermoelectric Technology Assessment: Application to Air Conditioning and Refrigeration. HVAc&R Research, 2008, 14(5): 635-653.

[64] Chung D Y, Hogan T, Brazis P, et al. CsBi4Te6: A high-performance thermoelectric material for low-temperature applications. Science, 2000, 287(5455): 1024-1027.

[65] E.A. Skrabek, D.S. Trimmer, in: D.M. Rowe (Ed.), CRC Handbook of Thermoelectrics, CRC Press, 1995.

[66] Boukai A I, Bunimovich Y, Tahir-Kheli J, et al. Silicon nanowires as efficient thermoelectric materials. Nature, 2008, 451(7175): 168-171.

[67] Callaway J. Model for lattice thermal conductivity at low temperatures. Physical Review, 1959, 113(4): 1046.

[68] Holland M G. Analysis of lattice thermal conductivity. Physical Review, 1963, 132(6): 2461.

[69] McConnell A D, Uma S, Goodson K E. Thermal conductivity of doped polysilicon layers. Microelectromechanical Systems, Journal of, 2001, 10(3): 360-369.

[70] Taylor R A, Solbrekken G L. Comprehensive system-level optimization of thermoelectric devices for electronic cooling applications. Components and Packaging Technologies, IEEE Transactions on, 2008, 31(1): 23-31.

[71] http://www.arieselec.com/

[72] http://en.wikipedia.org/wiki/Thermoelectric_cooling

[73] Kaltsas G, Nassiopoulou A G. Novel C-MOS compatible monolithic silicon gas flow sensor with porous silicon thermal isolation. Sensors and Actuators A:

Physical, 1999, 76(1): 133-138.

[74] Hiratsuka R, Van Duyn D C, Otaredian T, et al. Design considerations for the thermal accelerometer. Sensors and Actuators A: Physical, 1992, 32(1): 380-385.

[75] Van Kampen R P, Vellekoop M J, Sarro P M, et al. Application of electrostatic feedback to critical damping of an integrated silicon capacitive accelerometer. Sensors and Actuators A: Physical, 1994, 43(1): 100-106.

[76] Dauderstädt U A, De Vries P H S, Hiratsuka R, et al. Silicon accelerometer based on thermopiles. Sensors and actuators A: Physical, 1995, 46(1): 201-204.

[77] Xie J, Lee C, Feng H. Design, fabrication, and characterization of CMOS MEMS-based thermoelectric power generators. Microelectromechanical Systems, Journal of, 2010, 19(2): 317-324.

[78] Roncaglia A, Mancarella F, Cardinali G C. CMOS-compatible fabrication of thermopiles with high sensitivity in the 3–5μm atmospheric window. Sensors and Actuators B: Chemical, 2007, 125(1): 214-223.

[79] Boukai A, Xu K, Heath J R. Size-dependent transport and thermoelectric properties of individual polycrystalline bismuth nanowires. Advanced Materials, 2006, 18(7): 864-869.

[80] Shea R, Gawarikar A, Talghader J. Process Integration of Co-Sputtered Bismuth Telluride/Antimony Telluride Thermoelectric Junctions. Microelectromechanical Systems, Journal of, 2014, 23(3): 681-688.

[81] Gawarikar A S, Shea R P, Talghader J J. High detectivity uncooled thermal

detectors with resonant cavity coupled absorption in the long-wave infrared. Electron Devices, IEEE Transactions on, 2013, 60(8): 2586-2591.

[82] Wood R A, Han C J, Kruse P W. Integrated uncooled infrared detector imaging arrays, Solid-State Sensor and Actuator Workshop, 1992. 5th Technical Digest., IEEE. IEEE, 1992: 132-135.

[83] Schaufelbuhl A, Schneeberger N, Munch U, et al. Uncooled low-cost thermal imager based on micromachined CMOS integrated sensor array. Microelectromechanical Systems, Journal of, 2001, 10(4): 503-510.

[84] Eminoglu S, Tanrikulu M Y, Akin T. A low-cost 128 128 uncooled infrared detector array in CMOS process. Microelectromechanical Systems, Journal of, 2008, 17(1): 20-30.

[85] C.H. Du, C. LEE, "Characterization of Thermopile Based on Complementary Metal-Oxide-Semiconductor (CMOS) Materials and Post CMOS Micromachining", Jpn. J. Appl. Phys.,Vol. 41, pp.4340-4345, 2002.

[86] Du C H, Lee C. Characterization of thermopile based on complementary metal-oxide-semiconductor (CMOS) materials and post CMOS micromachining. Japanese journal of applied physics, 2002, 41(6S): 4340.

[87] Neumann N, Ebermann M, Kurth S, et al. Tunable infrared detector with integrated micromachined Fabry-Perot filter. Journal of Micro/Nanolithography, MEMS, and MOEMS, 2008, 7(2): 021004-021004-9.

[88] F. A. Carey, "Organic chemistry", Chapter 13, McGraw-Hill, 2000.

[89] Mao F, Lindeberg M, Hjort K, et al. A polymer foil non-contact IR temperature

sensor with a thermoresistor integrated on the back of a vertically configured thermopile. Sensors and Actuators A: Physical, 2012, 179: 56-61.

[90] Vukmir R B, Heller M B, Stein K L. Confirmation of endotracheal tube placement: a miniaturized infrared qualitative CO_2 detector. Annals of emergency medicine, 1991, 20(7): 726-729.

[91] De Graaf G, der Vlist W, Wolffenbuttel R F. Design and fabrication steps for a MEMS-based infrared spectrometer using evanescent wave sensing. Sensors and Actuators A: Physical, 2008, 142(1): 211-216.

[92] E. Hecht, "Optics", Chapter 13 (Addison Wesley, 2002).

[93] Arndt M, Sauer M. Spectroscopic carbon dioxide sensor for automotive applications, IEEE Sensors conference. 2004.

[94] Masuno K, Sawada T, Kumagai S, et al. Indirect wavelength selective infrared emitter using surface plasmon polariton, Solid-State Sensors, Actuators and Microsystems Conference (TRANSDUCERS), 2011 16th International. IEEE, 2011: 1586-1589.

[95] Rogalski A. Infrared detectors: status and trends. Progress in quantum electronics, 2003, 27(2): 59-210.

Chapter II: Theory and improvement of the thermopile structure design

2.1 Theory of thermopile design

A thermopile consists of many pairs of thermocouples that are electrically connected in series. A thermocouple comprises a pair of materials with different Seebeck coefficients. Figure 2.1 shows the typical structure of a thermopile. The red and yellow parts are the two different thermoelectric materials, which are connected in series.
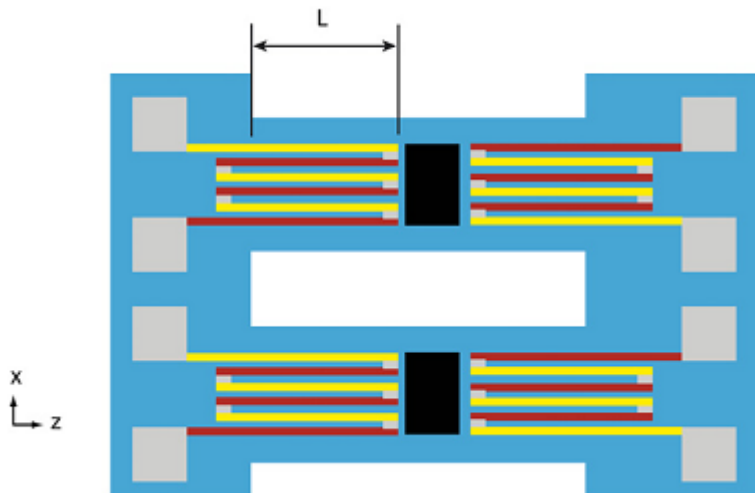
Figure 2.1 Schematic drawing of a typical thermopile.

According to the Seebeck effect, thermoelectric power is generated when there is a temperature difference between the two ends. The output voltage of a single thermocouple V_{out_single} can be described mathematically as [1]

$$V_{out\_single} = \Delta T(\alpha_1 - \alpha_2) = \Delta T\alpha_{12}, \tag{2.1}$$

where ΔT is the temperature difference between the two ends of the thermocouple. The end that has a higher temperature is known as the "hot junction", whereas the other end is known as the "cold junction". α_1 and α_2 are the Seebeck coefficients of the two materials, and the difference between α_1 and α_2 is defined to be α_{12}. In an IR radiation sensor that uses a thermopile design, the hot junction is the end that is close to the radiation absorber, whereas the cold junction is the end that is connected to a heat sink, e.g., the single crystal Si substrate, which represents the ambient temperature. The absorber layer absorbs IR radiation from the IR source and converts radiation power into heat, which causes the temperature of the hot junction to increase. In our experiment, the hot junction can also be connected to a microheater to create the desired temperature at the hot junction in a controlled manner. Thus, we can precisely calibrate the responsivity of the thermopile versus temperature difference between the hot junction and cold junction, which will be introduced in detail below.

Because of the suspended thermopile structure, the hot junction and cold junction are thermally isolated. Thermal isolation leads to a relatively high temperature difference between these two junctions. Due to the Seebeck effect, as we discussed above, the thermopile will generate an output voltage without any applied voltage bias. The thermopile is an array of thermocouples; thus, the output voltage of the thermopile, V_{out}, is

$$V_{out} = NV_{out\_single} = N\Delta T\alpha_{12}, \tag{2.2}$$

where N is the number of thermocouples.

The responsivity R_v can be expressed as

$$R_v = \frac{V_{out}}{P_{absorb}}, \tag{2.3}$$

where P_{absorb} is the IR power that is absorbed by the thermopile and can be calculated as

$$P_{absorb} = \eta\varphi_0 A, \tag{2.4}$$

where η is the absorption rate of the absorber, φ_0 is the IR radiation power density, and A is the area of absorber.

According to the Stefan-Boltzmann law, the radiance power density from the source to the thermopile can be expressed as

$$\varphi_0 = \sigma(T_s^4 - T_0^4)A_s/(\pi l^2), \tag{2.5}$$

where σ is the Stefan-Boltzmann constant, T_s is the temperature of source, T_0 is the ambient temperature, A_s is the area of the source and l is the distance between the source and thermopile.

The field of view is 2θ; thus, we can replace A_s with the detectable target area A_s', which is less than A_s. A_s' can be calculated with equation 2.6:

$$A_s' = \pi l^2 \sin^2\theta. \tag{2.6}$$

By substituting (2.6) into (2.5), φ_0 can be derived as

$$\varphi_0 = \sigma(T_s^4 - T_0^4)\sin^2\theta, \tag{2.7}$$

so

$$P_{absorb} = \eta\sigma(T_s^4 - T_0^4)\sin^2\theta\, A. \tag{2.8}$$

Then, we can calculate the responsivity as [2]

$$R_v = \frac{N\Delta T\alpha_{12}}{\eta\sigma(T_s^4 - T_0^4)\sin^2\theta\, A}, \tag{2.9}$$

where ΔT can be calculated as [3]

$$\Delta T = P_{absorb} * R_{ther} = \eta \varphi_0 A R_{ther}, \tag{2.10}$$

where R_{ther} is the thermal resistance.

The thermal resistance consists of 3 parts, K_s, K_g and K_r, which are the thermal conductance of the structure, caused by the atmosphere and the radiation, respectively.

$$R_{ther} = \frac{1}{K_s + K_g + K_r}. \tag{2.11}$$

The thermal conductance of the structure is expressed by Equation 2.12:

$$K_s = \sum \frac{k_i t_i w_i}{l_i}, \tag{2.12}$$

where k_i, t_i, w_i, l_i, are the thermal conductivity, thickness, width and length of each component.

Using the parallel plate approximation of air conduction, the thermal conductance of the atmosphere can be expressed by Equation 2.13:

$$K_g = (A + w_{SiO2} l_{SiO2}) k_g \left(\frac{1}{d_1} + \frac{1}{d_2} \right), \tag{2.13}$$

where w_{SiO2}, and l_{SiO2} are the width and length of the silicon dioxide (SiO_2) dielectric membrane (respectively), k_g is the thermal conductance of the atmosphere, d_1 is the distance between the membrane and the bottom of the release cavity, and d_2 is the distance between the top of the sensor and the cover of the package. The thermal cross-talk through air has been studied carefully by other researchers [4, 5].

Assuming that the ambient temperature, T_0, is much smaller than the temperature of the thermopile, T, ($T_0 \ll T$), the thermal conductance of the radiation is expressed by equation 2.14:

$$K_r = 4 w_{SiO2} l_{SiO2} \xi \sigma T^3, \tag{2.14}$$

where ξ is the emissivity of the thermopile. In most of the condition, the thermal

conductance of the radiation is much smaller than the thermal conductance of structure and atmosphere. Therefore, the thermal conductance of the radiation is normally ignored [3].

Another important parameter is the detectivity, D^*, which is expressed as

$$D^* = \sqrt{A\Delta f}/NEP, \qquad (2.15)$$

where Δf is the frequency bandwidth of the read-out system and *NEP* is the noise-equivalent power, which can be expressed as

$$NEP = V_n/R_v. \qquad (2.16)$$

V_n is the noise-equivalent voltage. There are three major types of noise source of thermopile: fluctuations of the sensor's temperature, fluctuations of the incident radiation and the electrical noise [6].

The thermopile is based on a thermal mass with heat capacity, *C,* and a non-ideal thermal conductance, *K,* to the surrounding environment (which has constant temperature T_0). According to the laws of statistical thermodynamics, the energy of the system fluctuates because energy can be transferred between the thermal mass and the ambient. The variation in the energy causes a variation in the system temperature (δT) with regard to its heat capacity [7]:

$$\delta T^2 = \frac{k_B T_0^2}{C}, \qquad (2.17)$$

where k_B is Boltzmann's constant and C is the heat capacity. In such system the transfer function between the input power and the resulting temperature difference in the frequency domain is a simple one-pole response that results in a power spectral density of temperature of:

$$S_{\delta T}(f) = \frac{4k_B T_0^2}{K} * \frac{1}{1+(2\pi f C/K)^2}. \tag{2.18}$$

The temperature fluctuations induce voltage fluctuations between the sensor electrodes due to the Seebeck effect with a power spectral density of:

$$S_{\Delta v,temp}(f) = N^2 \alpha_{12}^2 S_{\delta T}, \tag{2.19}$$

Fluctuations of the incident radiation power are another main noise source of thermopile IR sensor as well. The uncertainty in the incident radiation electrical field results in temperature fluctuations of the thermopile, which can be expressed as input radiation power fluctuations with power spectral density, $S_{\Delta P}$ [7]:

$$S_{\Delta P}(f) = 8\sin^2\left(\frac{\theta}{2}\right) WL\varepsilon_1 \varepsilon_{ob}\sigma k_B T_{ob}^5 + 8\cos^2\left(\frac{\theta}{2}\right) WL\varepsilon_1 \varepsilon_{ambient}\sigma k_B T_{ambient}^5 +$$

$$8WL\varepsilon_1 \sigma k_B (T_0 + \Delta T_1)^5, \tag{2.20}$$

where W is the total width of thermopile, L is the total length of thermopile, θ is the field of view of the thermopile IR sensor, σ is the Stefan–Boltzmann constant, T_{ob} is the temperature of the target object, ΔT_1 is temperature difference between the sensor and the ambient, $\varepsilon_1, \varepsilon_{ob}$ and $\varepsilon_{ambient}$ are the emissivity of the thermopile IR sensor, target object and ambient, respectively.

The contribution of radiation fluctuation to the output voltage can be calculated as:

$$S_{\Delta v,radiation}(f) = N^2 \alpha_{12}^2 S_{\Delta P}\left(\frac{\Delta T}{P_{absorb}}\right)^2, \tag{2.21}$$

The electrical noise of thermopile is mainly contributed by Johnson noise that is caused by the resistance of thermopile,

$$S_{\Delta v,electric} = 4kTR\Delta f, \tag{2.22}$$

where k is the Boltzmann constant and T is the temperature of the thermopile (in kelvin) and Δf is the noise bandwidth of the readout system.

The total noise of the thermopile IR sensor is

$$V_n = \sqrt{S_{\Delta v,temp} + S_{\Delta v,radiation} + S_{\Delta v,electric}} \ . \qquad (2.23)$$

Generally, the electrical noise is much higher than the other two kinds of noise. Therefore, most of the other researches only take into account the electrical noise [2-5,8,9]. Besides, the electrical noise measured by our testing setup is also very high because of the relatively large noise bandwidth ($\Delta f \sim 400 Hz$), such that the thermal noise and the radiation noise is negligible in my work. Therefore, in my study I make an approximation that there is only electrical noise V_n:

$$V_n \approx \sqrt{4kTR\Delta f} \ . \qquad (2.24)$$

Then, we can calculate the detectivity as

$$D^* = R_v\sqrt{A/4kTR} \ . \qquad (2.25)$$

The responsivity, R_v, detectivity, D^*, and noise-equivalent power, *NEP*, are the main parameters that are used to characterize the thermopile. R_v stands for the output of the thermopile, which corresponds to the output efficiency of the sensor. *NEP* represents the input power when the output voltage is equal to the noise power. D^* is the inverse of the *NEP* and is normalized by the absorption area and signal frequency. The *NEP* indicates the value of signal that can be detected by the sensor.

2.2 Improvement on structure design: stacked double-layer (SDL) thermopile structure

As described in section 2.1, the research directions of achieving a highly effective thermoelectric sensor rely on two main approaches: 1) having low thermal conductance and 2) using n- and p-type thermoelectric materials with large difference in the Seebeck coefficients (α_{12}) to form the thermocouple. While conventional coplanar thermopiles using Al and doped poly-Si have both of the above-mentioned drawbacks, we propose a stacked double-layer (SDL) thermopile in order to remedy this issue.

Figure 2.1 shows a schematic drawing of the conventional coplanar thermopile and the SDL thermopile. Both thermopiles are formed in a plus-shaped structure in which the central part forms an absorber that absorbs the IR radiation, thereby causing a temperature increase at the hot junction. The entire thermopile is suspended on a thin membrane such that the heat can be transferred from the hot junction to the cold junction only through the thermopile. The cold-junction is thermally connected to the single-crystal Si substrate (heat sink), as shown in Figure 2.1. The Si substrate has high thermal conductance and a large thermal mass to maintain a relatively constant temperature at the cold junction. Thus, there will be temperature difference between the hot and cold junctions, thereby inducing a voltage decrease between these two junctions.
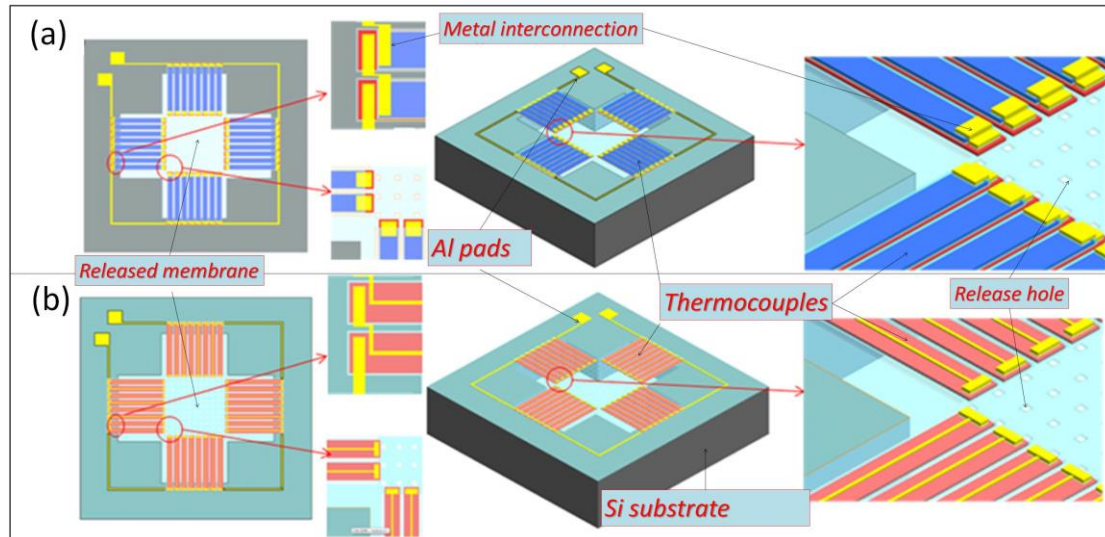
Figure 2.1. Schematic drawing of the (a) SDL thermopile and (b) conventional coplanar thermopile

The poly-Si strips are interconnected by Al lines in series; thus, the thermopile might suffer from the problem of high contact resistance between the Al and poly-Si [8], thereby causing a high Johnson noise, which might undermine the device performance. Hence, the process condition was optimized to increase the surface doping concentration through high doping dosage and low implantation energy to achieve a shallow doping but with very high doping concentration (so called "contact doping"). This contact doping reduces the contact resistance between the Al and poly-Si. [9].
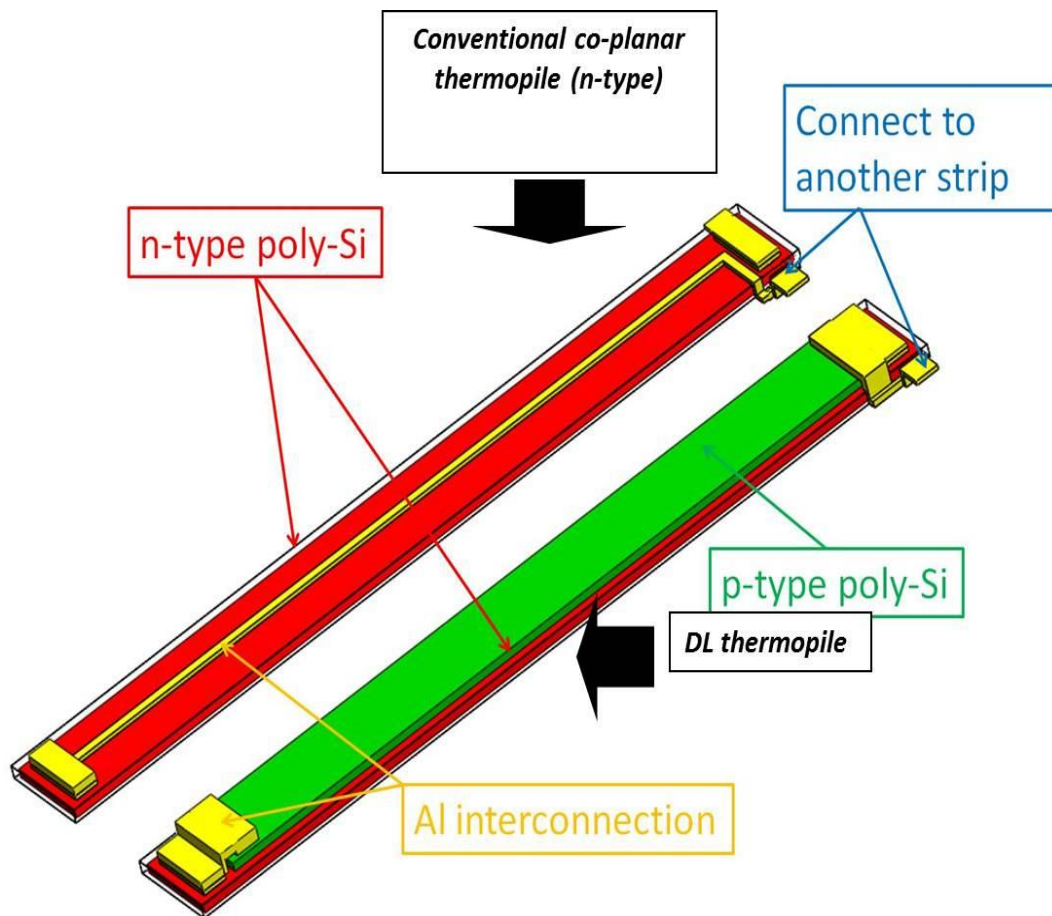
Figure 2.2. Comparison between a single thermocouple of the conventional coplanar thermopile and SDL thermopile designs.

Figure 2.2 shows a comparison between a single thermocouple in the conventional coplanar thermopile and SDL thermopile designs, respectively. The coplanar thermopile utilizes doped poly-Si and Al as the thermocouple, whereas the thermocouples in the SDL thermopile are formed by pairs of n-type poly-Si and p-type poly-Si. The difference in the properties of Al and that of the doped poly-Si is what makes a significant difference in the performance of the conventional coplanar thermopile and SDL thermopile. The details of the material properties that are used in the thermopile design are shown in Table 2.1. Both n- and p-type poly-Si are studied in this work. Table 2.1 indicates that the absolute value of the Seebeck coefficient of

Al is considerably less than that of the doped poly-Si, whereas the thermal conductance of Al is considerably greater than that of the poly-Si. As indicated by Equations 2.1 and 2.9, both the low Seebeck coefficient and the high thermal conductance (low thermal resistance) decrease the performance of the thermopile. In the convectional coplanar thermopile, metal wires are used for the electrical connection between the hot and cold junctions. As such, a large amount of heat will be transferred through the metal line from the hot junction to the cold junction. This condition causes a smaller temperature difference between them and thus a smaller output voltage.

Table 2.1. Material properties used for the thermopile design.

	n-type poly-Si	p-type poly-Si	Al	SiO$_2$	Si
Thermal conductivity (W/mK)	29.7	28.4	237	1.25	149
Seebeck coefficient (μV/K)	−110	130	-1.8	-	-
Resistivity (μΩm)	8.9	13.7	0.03	-	-

However, the stacked thermopile does not have such disadvantages. The Al acts as a connector between the n- and p-type Si such that the heat transfer between the hot and cold junctions only occurs through the doped Si (Figure 2.2). Although the thickness of poly-Si in this design is two times greater than that of the planar structure, the thermal conductance between the hot junction and cold junction is less because of the relatively low thermal conductivity of poly-Si compared with Al.

The SDL thermopile also has advantages in terms of the Seebeck coefficient difference, α_{12}. The α_{12} of the thermocouple formed by the doped poly-Si and Al

(shown in the left of Figure 2.2) is only half of the value of the Seebeck coefficient difference of the thermocouple formed by a pair of n- and p-type poly-Si (shown in the right of Figure 2.2). Hence, the output voltage of the SDL thermopile will also be higher, according to Equation 2.2.

Although the SDL thermopile has advantages in terms of the thermal conductance and Seebeck coefficient difference, there is still a drawback in terms of the electric conductance. As indicated by Table 2.1, the electrical resistivity of poly-Si is greater than that of Al, which means that the electrical resistance of the SDL thermopile is nearly double of that of a conventional coplanar thermopile if we omit the contact resistance. The electrical resistivity, as indicated by Equation 2.24, affects the noise. Therefore, the noise will increase by a factor of $\sqrt{2}$ at most. However, according to the above discussion, the R_v of the SDL thermopile will at least be double of that of a conventional coplanar thermopile, which means that the D^* will also increase, according to Equation 2.25. In summary, the performance of the SDL thermopile is better overall.

The dimension parameters were optimized with the ANSYS-12.0 finite element simulation software package and MATLAB 7.0. To obtain the temperature difference between the hot junction and cold junction of the thermopile, the simulation was performed in two dimensions (2D) because the thermopile design is symmetrical. An example of the simulation result is shown in Figure 2.3.
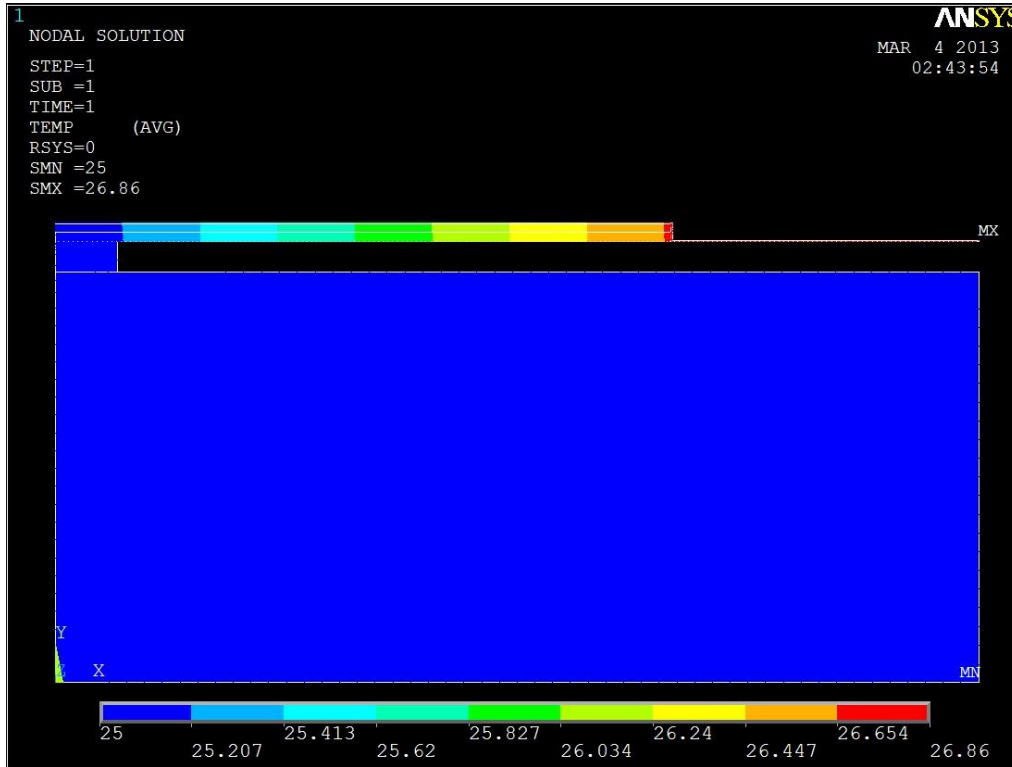
Figure 2.3. 2D ANSYS simulation result showing the crossing-sectional view of the temperature difference in the thermopile.

Using the derived the data of temperature difference obtained from the simulations, the R_v and D^* values were calculated using MATLAB based on the equations given above, and an evaluation of the performance of the thermopiles with different dimensions was performed. The optimal result is obtained when the length of the thermopile is 600 μm, the width of the thermopile is 12 μm, and the number of thermocouples is 96. The thickness of the poly-Si strips is 0.7 μm, and the thickness of the SiO_2 electrical isolation layer is 0.15 μm. Based on these parameters, the simulation was conducted, and the results indicate that the responsivity of the n-type coplanar thermopile is 37.08 V/W and the detectivity is 0.93×10^8 cm×$Hz^{1/2}$×W^{-1}, whereas the responsivity of the SDL thermopile is 76.9 V/W and the detectivity is 1.53×10^8 cm×$Hz^{1/2}$×W^{-1}. Although all properties of the materials in the simulation are

estimated values, such as the electric resistivity, thermal conductivity and Seebeck coefficient, the simulation can still provide significant insights and hints for future designs.

The mechanical strength of the device need be studied as well. Because the membrane is large, e.g., close to 1mm and the thickness is thin, e.g., less than 2 μm, the membrane may suffer from break because of stress. To study the mechanic strength of the structure, a simulation with COMSOL 4.3 was conducted. The simulation result is shown in Figure 2.4. Figure 2.4 illustrates that the largest stress in the membrane is 240 MPa under 10% atmospheric pressure; the number is less than the fracture strength of 364±57 MPa [10]. The mechanical strength of the structure is quite good.
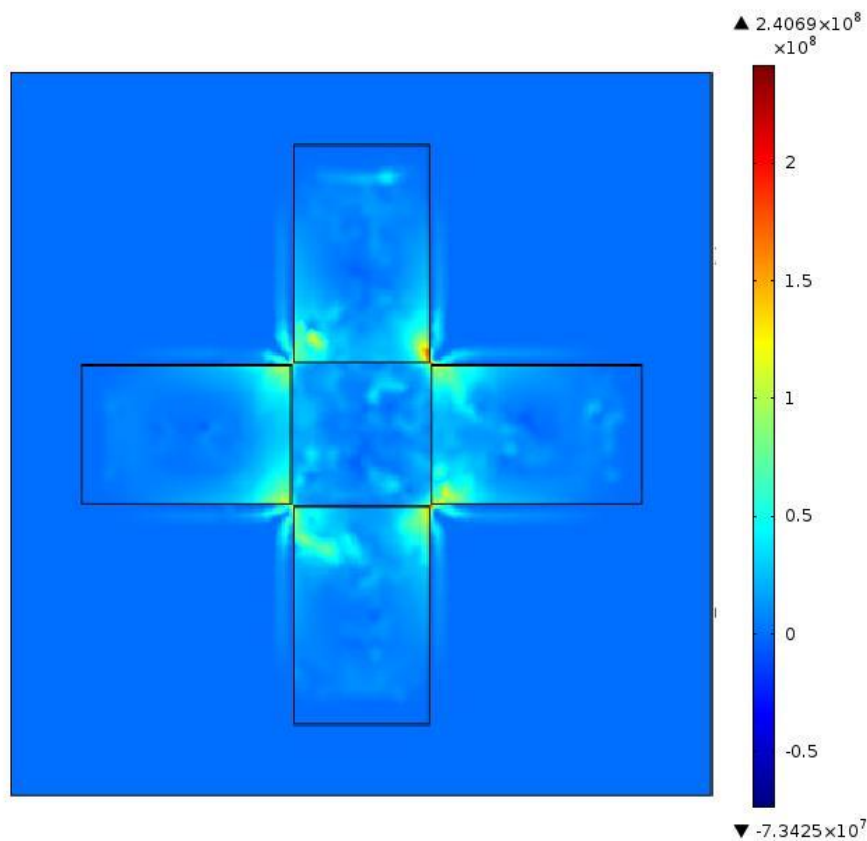
Figure 2.4. 3D COMSOL simulation result that shows the stress distribution on the thermopile with a load of 10 times the atmospheric pressure (top view).

2.3. Fabrication of the thermopile structure

Figure 2.5 shows the CMOS-compatible microfabrication process flow of the SDL thermopiles reported in this Chapter. An 8" Si wafer with a thickness of 725 μm was used as the substrate. First, a 0.2-μm-thick thermal insulating SiO_2 layer was deposited on the front side of the wafer by low-pressure chemical vapor deposition (LPCVD) at 600°C to serve as an electrical isolation and mechanical supporting layer [Figure 2.5(a)]. Then, the 0.7-μm-thick poly-Si, which was used as the thermoelectric layer, was deposited at 580°C in a furnace by LPCVD. The poly-Si layer was implanted with phosphorus at 120 KeV energy and patterned by reactive ion etching (RIE) to form n-type thermoelectric strips with pattern dimensions of 12 μm in width and 600 μm in length [Figure 2.5(b)]. A 0.15-μm-thick SiO_2 layer, which serves as electrical insulation, was further deposited by plasma-enhanced chemical vapor deposition (PECVD) [Figure 2.5(c)]. A second poly-Si layer was deposited by LPCVD; it was then boron-implanted using energy of 50 keV and patterned to form the p-type thermoelectric strips. Subsequently, a 0.15-μm SiO_2 layer was further deposited by PECVD as an electrical insulation layer [Figure 2.5(d)]. A doping dosage of 10^{15} cm^{-2} was used in both implantation steps.

After the step of contact-via-opening for n-type poly-Si strips, n++ heavy doping was performed with 40 KeV at contact via region. Then, contact-via-opening for p-type poly-Si strips was conducted. Subsequently, a p++ contact via doping was performed with 20 KeV. A doping dosage of 10^{16} cm^{-2} was used in both cases. An annealing step was conducted at 1,000°C for 30 min. [Figure 2.5(e)]. Then, an Al layer was deposited by sputtering and patterned to form a metal interconnection between the n-

and p-type poly-Si strips [Figure 2.5(f)]. To establish good ohmic contact between the Al and poly-Si, the wafer was annealed at 420°C for 30 min. To confine the heat flux within the thermopile beams, the underlying Si was etched to form a cavity, and the etching steps were conducted by depositing the 0.5-µm-thick SiO_2 hard mask first [Figure 2.5(g)]. After that, a deep Si trenches etched via deep reactive ion etching (DRIE) based on Sulfur Hexafluoride (SF_6) and Octafluorocyclobutane (C_4F_8) gases were etched until a 10 µm etch depth was attained. Then, the wafer was isotropically etched by SF_6 to remove the Si trench structures [Figure 2.5(h)].
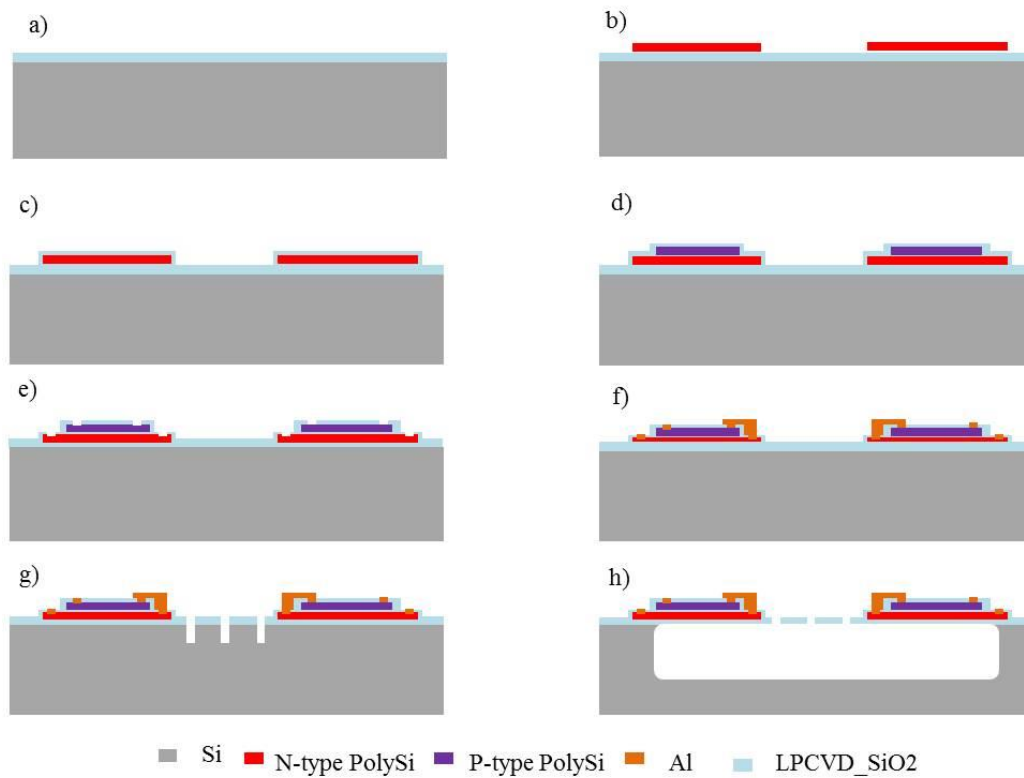
Figure 2.5. Fabrication process flow: (a) deposition of thermal SiO_2 on a Si wafer by LPCVD. (b) Poly-Si deposition, n doping and etching, along with simultaneous fabrication the microheater. (c) PECVD SiO_2 dielectric layer deposition. (d) Poly-Si deposition, p doping and etching, covered by PECVD SiO_2. (e) Contact via open and contact doping. (f) Al wire and absorber layer deposition. (g) Release holes opening. (h) Front-side release.

2.4 Experimental results

2.4.1 Thermoelectric properties of heavily doped bulk poly-Si

Both The electrical resistivity and specific contact resistivity between Al and poly-Si are crucial to the design of thermopiles because these two parameters determine the *NEP* and *D**. As discussed in section 2.1, the low electric resistivity and specific contact resistivity between Al and poly-Si are desirable to improve the design of thermopiles. In my study, the resistivity was determined by the van-der-Pauw structure [Figure 2.6(a)][11]. The resistivity values of the n- and the p-type poly-Si are 9.6 and 15.9 μΩ×m, respectively. The electric contact resistance was derived based on the Kelvin structure [Figure 2.6(b)] [7]. The specific contact resistivity values of Al-to-n-type-poly-Si and Al-to-p-type-poly-Si are 10.4 and 4.3 μΩ×cm^2, respectively, indicating that both of the surface doping concentrations are approximately 10^{20} cm^{-3} [12].
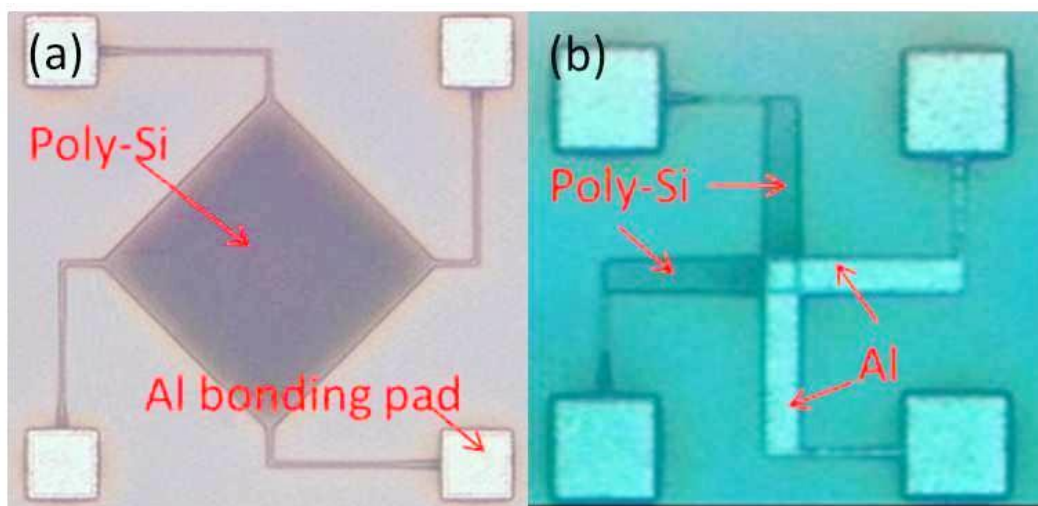
Figure 2.6. Test structures for resistivity and contact resistivity: (a) van-der-Pauw structure to measure the resistivity of the poly-Si and (b) Kelvin structure to test the contact resistivity.

The Seebeck coefficient and thermal conductance were determined by a cantilever test structure, as shown in Figure 2.7, which is a single thermocouple using poly-Si and Al as the two thermoelectric materials. The cantilever comprises three layers: thermal SiO_2, doped poly-Si and PECVD SiO_2. The narrow Al line connects the hot junction and the cold junction for electric signal readout. The geometries of the n- and p-type cantilever test structures are the same. The thickness, width, and length of the poly-Si in the test structure are 300 nm, 90 µm and 300 µm, respectively. The width of the Al line is 1 µm, and the thickness is 300 nm. The theoretical thermal conductance of SiO_2 is considerably lower than that of the doped poly-Si, and the dimensions of Al metal line are smaller than those of the cantilever by nearly two orders of magnitude. It is expected that the cantilever can reflect the thermal conductance of the poly-Si.

A microheater is arranged at the end of the hot junction, as shown in Figure 2.7, to heat up the hot junction of the test structure. Although the Seebeck coefficient of the poly-Si varies with the temperature of the device, the temperature rise caused by the microheater during testing is minimized such that the output voltage at different temperatures is linearly correlated with the applied input power (Figure 2.9 and 2.10). The above testing results indicate that reliable data can be derived by our test key and testing approach.
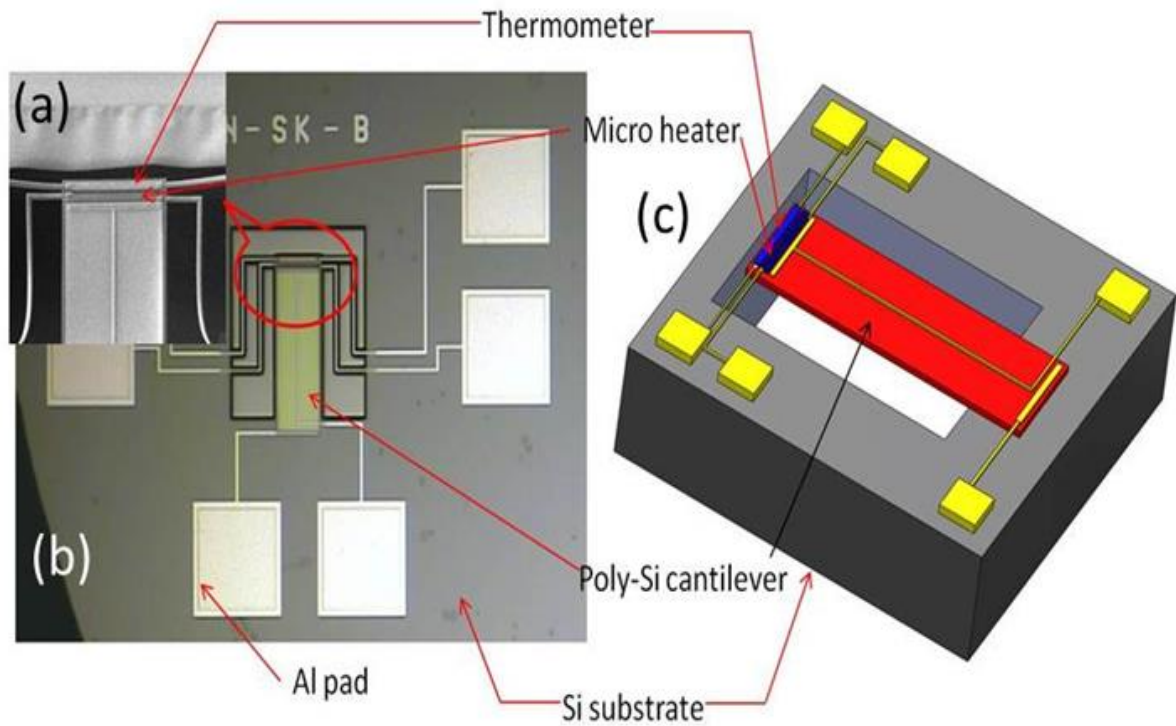
Figure 2.7. SEM image (a), optical microscope image (b) and drawing (c) of a test key for thermal conductivity and Seebeck coeffcient.
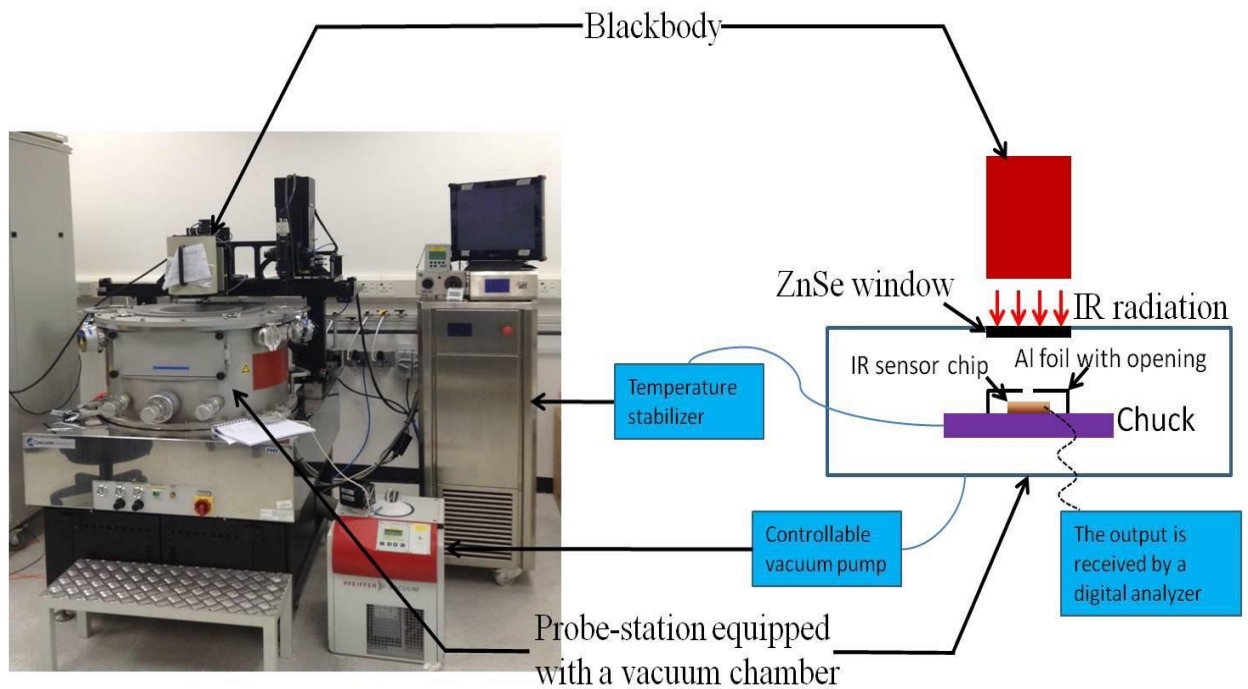
Figure 2.8. Equipment for testing.

The electrical measurement was performed using a semiconductor parameter analyzer (Agilent technology, 4156C) equipped with a probe station (Cascade Microtech, PMV200) [Figure 2.8]. The blackbody was used for infrared test which will be introduced in Chapter III.

Figure 2.9 shows the measurement results of the n-type cantilever test structure. To observe the thermocouple's performance, a bias voltage of -5 V to 5 V with increments of 0.1 V was applied. The hot junction was connected to the ground, which resulted in a positive output voltage because the Seebeck coefficient of the n-type poly-Si is negative. Figure 2.9 shows the curve of output voltage vs. input power; it shows a good linear relationship.
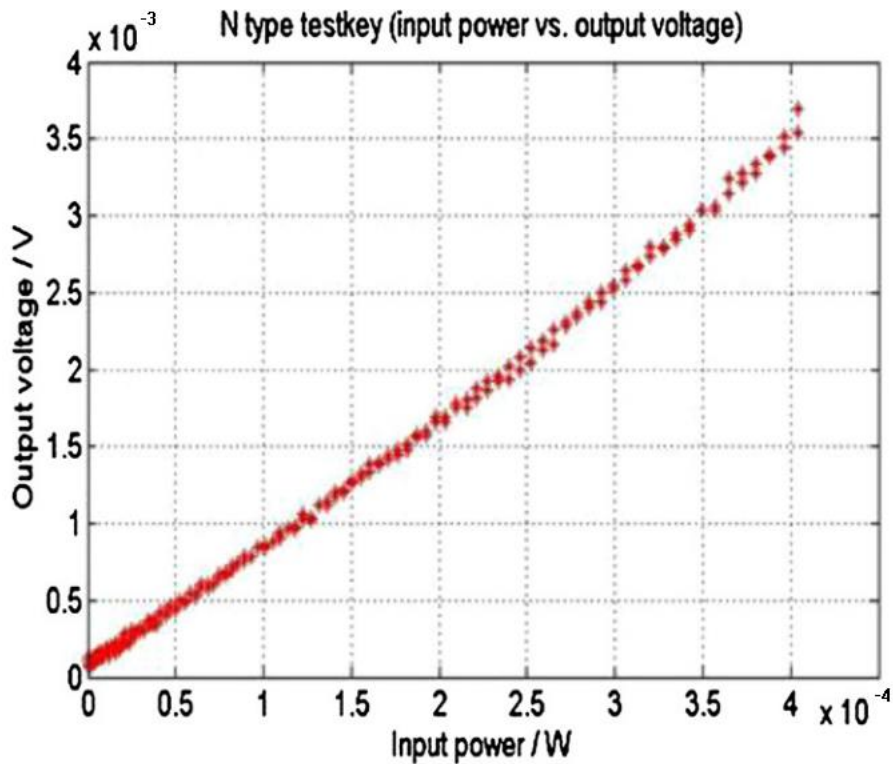
Figure 2.9. n-type thermopile test structure characterization of input power vs. output voltage.

Figure 2.10 shows the testing results of the p-type single thermocouple. The results are opposite to those obtained from the n-type single thermocouple because the Seebeck coefficient of p-type poly-Si is positive.

The measurements to determine the Seebeck coefficient and thermal conductance were conducted in vacuum to eliminate the influence of the conductance of air. The entire measurement was performed at a pressure of less than 1×10^{-4} mbar.
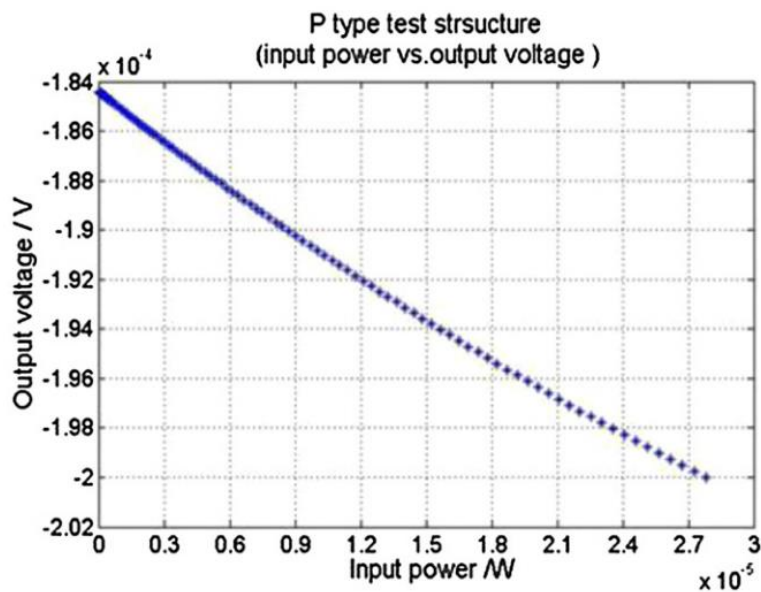
Figure 2.10. p-type thermopile test structure characterization of input power vs. output voltage.

In order to determine the Seebeck coefficient and thermal conductivity of the poly-Si, the temperature at the hot junction must be measured, because the temperature at the cold junction equals the temperature of the substrate, which reflects the ambient temperature. As shown in Figure 2.7, a thermometer made of poly-Si is arranged at the end of the hot junction to monitor the temperature. TCRs of the poly-Si are needed to monitor the temperature. The Van-der-Pauw test structure, shown in Figure 2.6(a), was used to determine the TCRs of the heavily doped poly-Si, which is approximately -0.22%/K and -0.17%/K for n- and p-type poly-Si, respectively.

69

The temperature difference between the cold junction and the hot junction can be derived by using Equation 2.26:

$$R(T) = R(T_0) * (1 + TCR * (T - T_0)), \qquad (2.26)$$

where, $R(T)$ is the resistance at temperature T and $R(T_0)$ is the resistance at the original temperature. Equation 2.26 can be used to calculate the temperature difference between the cold junction and the hot junction. Additionally, the thermal conductance can be calculated with Equation 2.27:

$$K_{S_i} = P_{in} * \Delta T = P_{electric} * (T - T_0), \qquad (2.27)$$

where K_{S_i} is the thermal conductance of the poly-Si and $P_{electric}$ is the electrical energy applied in the experiment, which can be calculated with the applied voltage, V_{in} and the electrical resistance of the heater, R_{heater}, as

$$P_{electric} = V_{in}^2 / R_{heater}. \qquad (2.28)$$

The temperature of the hot junction can then be obtained by the I/V curve of the thermal sensor. The thermal conductivity values of the n- and the p-type poly-Si are 31.8 and 30.7 W/mK, respectively. The Seebeck coefficient can be calculated using Equation 2.1; the Seebeck coefficients of n- and p-type poly-Si are -118 and 137 µV/K, respectively. The results are shown in Table 2.2.

Table 2.2. Thermal conductivity and Seebeck coefficient of the n- and p-type poly-Si.

	n-type poly-Si	p-type poly-Si
Thermal conductivity (W/mK)	31.9	33.6
Seebeck coefficient (µV/K)	−118	137

2.4.2 Characterization of the thermopile structures at atmospheric pressure

The micro-heater was placed at the central part of the thermopile sensor [Figure 2.11]. A voltage bias was added to the micro-heater to heat it. The microheater acted as a heat source, thus imitating an IR source. A semiconductor parameter analyzer equipped with a probe station was used to conduct the measurements.
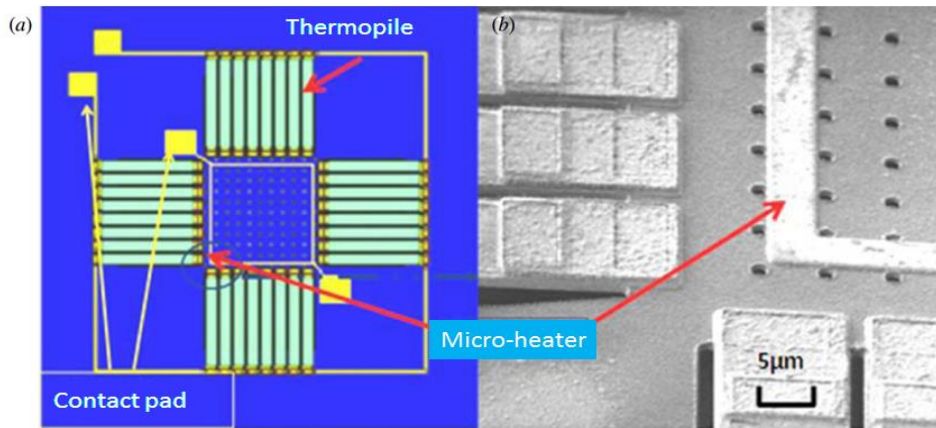
Figure 2.11. (a) Schematic and (b) SEM image of the micro-heater.

The thermal transfer in the thermopile is different when a microheater is used instead of a real IR source. To address the difference, a simulation was performed with the ANSYS software package. A microheater was added near the hot junction of the thermopile, while the heat flux was added to this heater instead of the entire absorber. The total power added to the thermopile was the same as used in the simulation as discussed in section 2.2. Figure 2.12 shows the simulation results of the microheater. The temperature difference between the hot junction and cold junction was 1.5499 K for microheater and 1.5603 K in the case of an IR source. The difference was less than 1%, which means that the use of a microheater to imitate the IR source is reasonable.

71
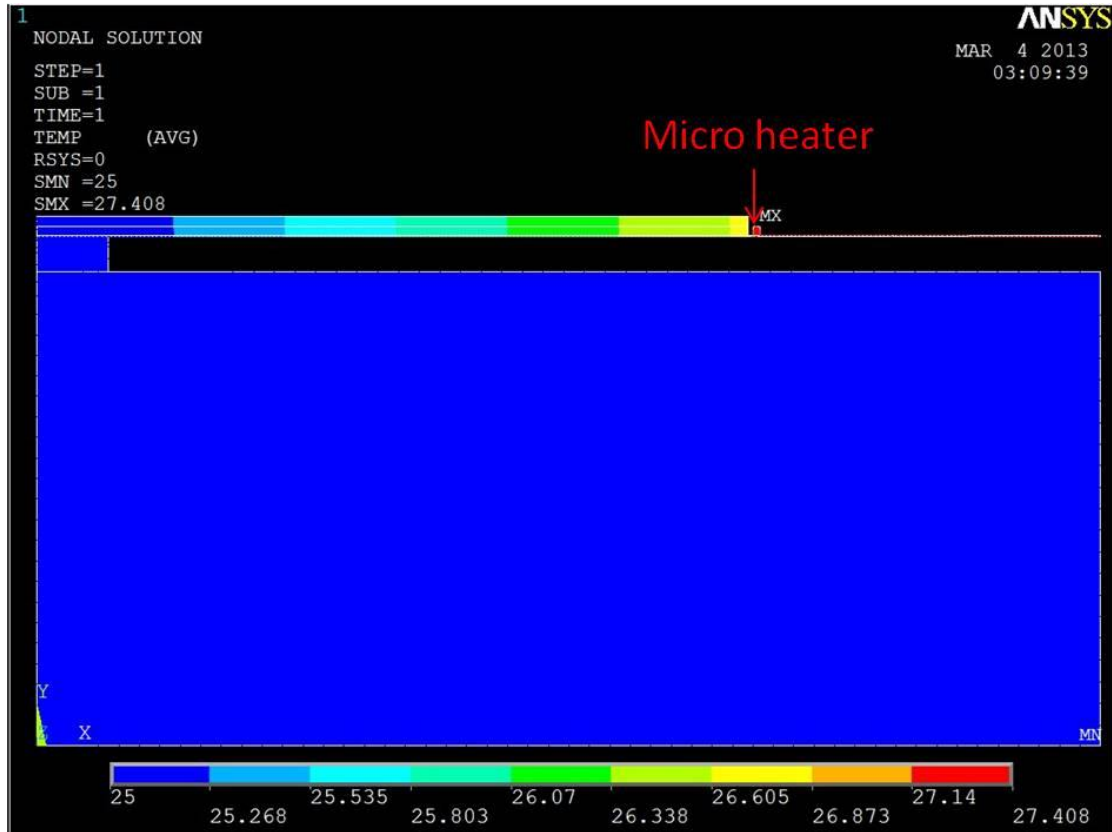
Figure 2.12. 2D ANSYS simulation results with a micro-heater to show the cross-sectional view of the temperature difference in the thermopile.

Figure 2.13 shows the measurement results of the n-type conventional coplanar thermopile sensors in atmosphere. The voltage bias was varied from -5 V to 5 V with increments of 0.1 V. The responsivity of the n-type conventional coplanar thermopile sensors was obtained using Equations 2.3 and 2.25. The derived R_v of the n-type thermopile working at atmospheric pressure was 31.9 V/W. The electrical resistance of the n-type thermopile was measured to be 190 kΩ. Then, the *NEP* of the n-type thermopile was derived to be 1.76×10^{-6}W at atmospheric pressure. The *D**, at atmospheric pressure, was derived using Equations 2.14 and 2.15. The calculated *D** value is 0.58 cmHz$^{1/2}$W^{-1}. R_v, *D** and *NEP* are shown in Table 2.3.
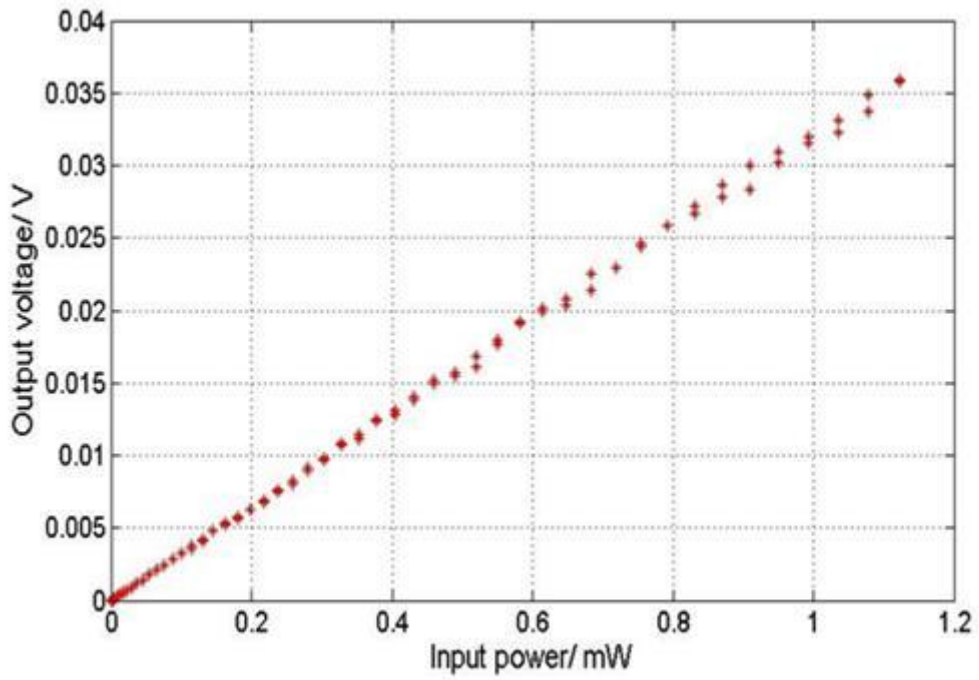
Figure 2.13. Thermopile sensor characterization of input power vs. output voltage for the n-type thermopile.
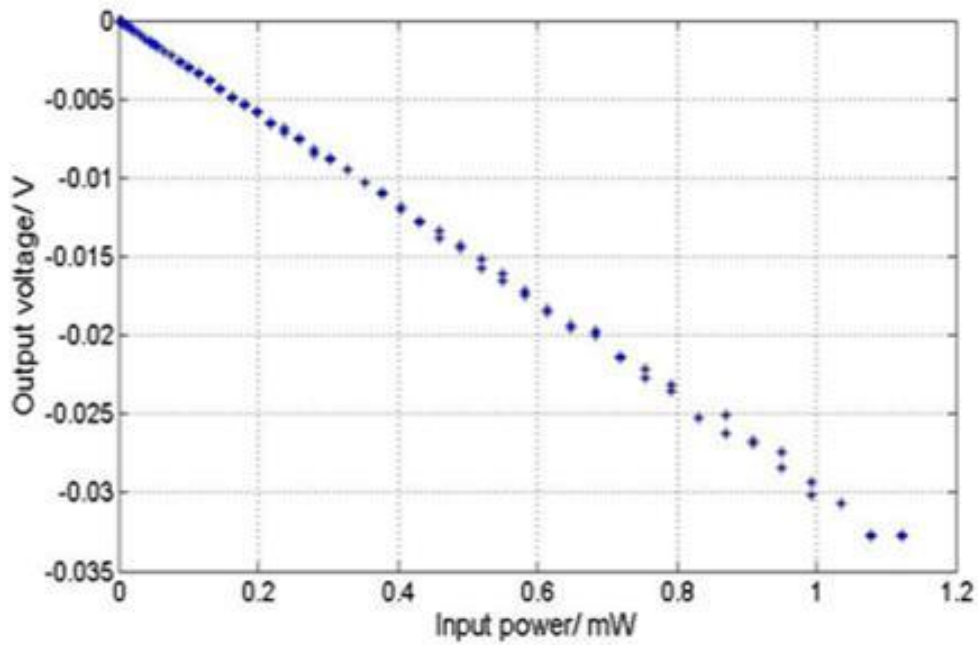
Figure 2.14. Thermopile sensor characterization of input power vs. output voltage for the p-type thermopile.

The measurement results of the p-type coplanar thermopile are shown in Figure 2.14. R_v, *NEP* and *D** were all measured or derived in the same manner as for the n-type thermopile. The estimated R_v of the p-type thermopile at atmospheric pressure was 30.0 V/W. The electrical resistance of the p-type thermopile was measured to be 115 kΩ. Then, the *NEP* of the n-type thermopile was derived to be 1.45×10^{-6}W at atmospheric pressure, and the *D** was 0.69 cmHz$^{1/2}$W^{-1} with the same value for the absorber area. The R_v, *NEP* and *D** values of the p-type thermopile are also showcased in Table 2.3.

Based on the same method stated above, characterization of the SDL thermopile was conducted. The measurement results at atmospheric pressure are shown in Figure 2.15. The output voltages are also proportional to the input power. The measured R_v of the SDL thermopile at atmospheric pressure was 88.5 V/W. The resistance of the SDL thermopile was 306 kΩ; it was determined to derive the *NEP*. The *NEP* of the SDL thermopile was 0.81×10^{-6}W at atmospheric pressure, and the *D** was 1.24 cmHz$^{1/2}$W^{-1}. The R_v, *NEP* and *D** values of the SDL thermopile are also shown in Table 2.3.
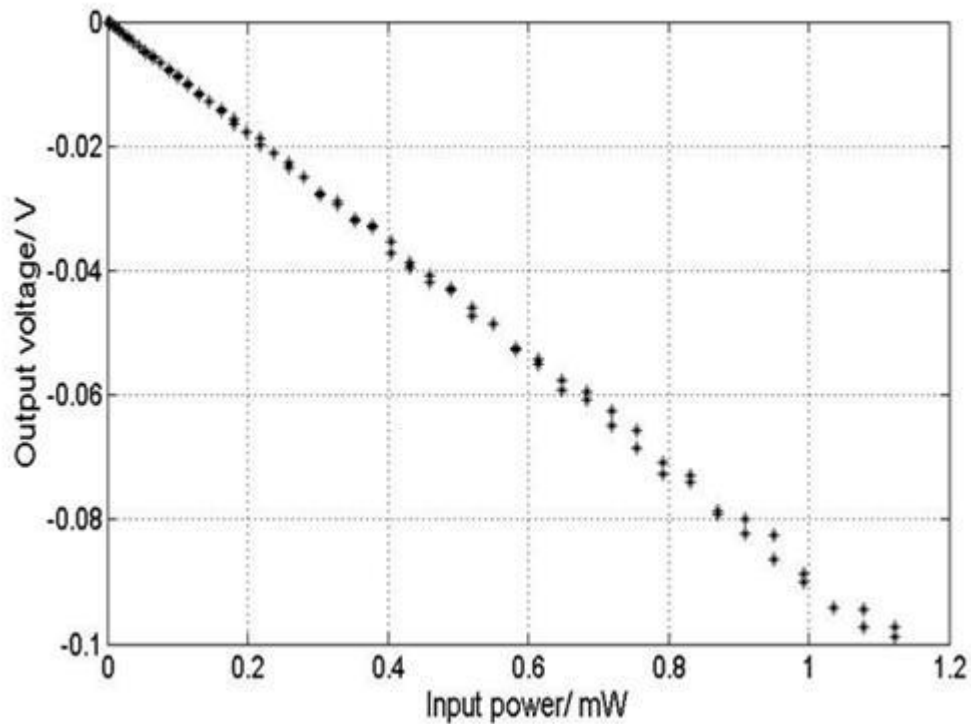
Figure 2.15. Thermopile sensor input power vs. output voltage for the SDL thermopile.

The SDL thermopile performed significantly better than both of the coplanar thermopiles. This superior performance originates primarily from two key parameters of the thermopile, namely, the low thermal conductance and high Seebeck coefficient difference.

As shown in Figure 2.2, there is no metal that connects the hot junction and cold junction in the SDL thermopile. The thermal conductance of a single thermocouple for the three types of thermopile were calculated based on the measured thermal conductance presented in Table 2.2. The thermal conductance of the SDL thermocouple was 0.1385×10^{-5} W/K, in juxtaposition with that of the n- and the p-type of thermocouples as 0.141×10^{-5} and 0.147×10^{-5} W/K, respectively. The thermal conductance of the SDL thermocouple was less than those of the coplanar thermopiles.

75

The SDL thermocouple was formed by a pair of n- and p-type poly-Si layers. The Seebeck coefficients of n- and p-type poly-Si are -118 and 137 µV/K, respectively [Table 2.3], whereas the Seebeck coefficient of Al is only -1.8 µV/K [Table 2.1]. Therefore, the Seebeck coefficient of the SDL thermopile is considerably greater than the coefficients of the coplanar thermopiles. The calculated Seebeck coefficient difference was 225 µV/K, compared with 116.2 and 138.8 µV/K for the n- and p-type thermocouples, respectively. The Seebeck coefficient difference for the SDL thermocouple was nearly double of that of the coplanar thermocouples.

Table 2.3. Performance of the 3 types of thermopiles.

	SDL thermopile			p-type thermopile			n-type thermopile		
	NEP (10^{-6}W)	D* ($cmHz^{1/2}W^{-1}$)	R_v (V/W)	NEP (10^{-6}W)	D* ($cmHz^{1/2}W^{-1}$)	R_v (V/W)	NEP (10^{-6}W)	D* ($cmHz^{1/2}W^{-1}$)	R_v (V/W)
Atmosphere (Assuming emissivity=1)	0.81	1.24×10^8	88.5	1.45	0.69×10^8	30.0	1.76	0.58×10^8	31.9
Vacuum (Assuming emissivity=1)	0.35	2.85×10^8	202.8	0.63	1.57×10^8	68.8	0.77	1.30×10^8	73.2
Atmosphere (Assuming emissivity=0.8)	0.82	0.99×10^8	70.8	1.62	0.55×10^8	24.0	1.73	0.45×10^8	25.6
Vacuum (Assuming emissivity=0.8)	0.35	2.28×10^8	162.3	0.63	1.26×10^8	55.1	0.77	1.04×10^8	58.6

2.4.3 Characterization of the thermopile structures in vacuum

Experiments on the three types of thermopiles were also conducted at different vacuum levels with the probe station mentioned in previous section equipped with a vacuum chamber. The measurement results are shown in Figure 2.16. The influence of the thermal conductance of air is significant. According to Equations 2.9 and 2.10, R_v is proportional to the thermal resistance, it also means that R_v is inversely proportional to the thermal conductance. As introduced in Chapter 2.1, K_r can be ignored, because it is two-orders smaller than $K_s + K_g$. Thus R_v is inversely proportional to the thermal conductance attributed to structure and air, i.e., $R_v \propto \frac{1}{K_s + K_g}$, when the thermopile is characterized in atmosphere. Therefore, the R_v is only inversely proportional to the solid thermal conductance of thermopile structure when the thermopile was characterized in vacuum, i.e., $R_v \propto \frac{1}{K_s}$ and the thermal conductance of air is zero. As shown in Figure 2.16, R_v obtained in atmosphere is less than half of R_v obtained in vacuum. It indicates that over 50% thermal conductance of the device is contributed by heat loss via air. Besides, the thermal conductance due to heat loss via air is proportional to the thermopile area according to Equation 2.13; hence, it is important to reduce the area of the thermopile so as to minimize the thermal conductance of air. The SDL thermopile has the advantage of a smaller footprint compared with the n- and the p-series coplanar thermopile, such as those used in [8,13-15].
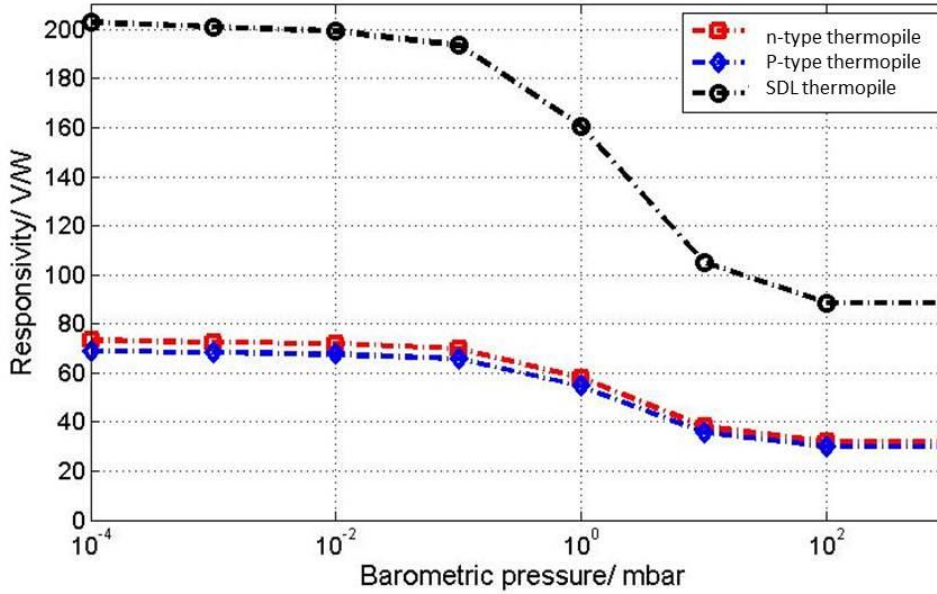
Figure 2.16. Thermopile characterization for different barometric pressures.

According to the dimensions and number of thermocouples used in this Chapter (600 μm in length, 12 μm in width and 96 thermocouples per thermopile), the areas of the n- and p-series coplanar thermopiles is calculated as 1.77×10^6 μm². This value is nearly 2.3 times higher than that of the SDL thermopile having the same dimension and number of thermocouples (7.89×10^5 μm²). In atmospheric conditions, the total thermal conductance of the SDL thermopile is 0.28×10^{-3} W/K, as derived from the measured Seebeck coefficient difference [Table 2.2] and responsivity (R_v) using Equations 2.9-2.13. In a vacuum chamber, the influence of the atmosphere is limited, and the thermal conductance of the SDL thermopile from the structure and radiation was determined to be 0.12×10^{-3} W/K. This result indicates that 56% of the thermal conductance was attributed to the air under atmospheric pressure. Thus, when the area of the coplanar thermopile becomes 2.3 times that of the SDL thermopile, the thermal conductance of the coplanar thermopile from the air, $K_{s\_coplanar}$, becomes 2.3 times of the thermal conductance of the SDL thermopile from the air, K_{g_SDL}, whereas the

79

area of the cross-section of the poly-Si remains the same. Thus, we can assume that the thermal conductance of the thermopile structure also remains the same, hence $K_{s\_SDL} = K_{s\_coplanar}$. With this assumption, the total thermal conductance of the n-/p-series coplanar thermopile will increase to 0.48×10^{-3} W/K, which means that the thermal conductance will increase by more than 70% as compared with that of the SDL thermopile. Thus, the responsivity R_v of the SDL is more than 70% greater than that of the n/p-series coplanar thermopiles; this indicates the great advantage of the SDL thermopile.

2.5. Conclusions

Using CMOS-compatible processes, the design, fabrication and testing of the micromachined n/p-type poly-Si thermopile in both the coplanar and SDL configurations have been reported. Both analytical calculations and experimental data suggest that the SDL thermopile has advantages in terms of the thermal conductance and Seebeck coefficient difference, which makes the SDL thermopile superior to conventional coplanar thermopiles. Although the resistance of the SDL thermopile is greater than that of coplanar thermopiles, both the responsivity and detectivity of the SDL thermopile are better. Characterization of the SDL thermopile indicated that the responsivity in vacuum and air were as high as 202.8 and 88.5 V/W, respectively; the detectivity in vacuum and air were as high as 2.85×10^{8} and 1.24×10^{8} cmHz$^{1/2}$W^{-1}, respectively.

This new SDL thermopile provides improved sensor performance as compared with the coplanar thermopiles in terms of a smaller footprint and smaller surface area

exposed to air. Thus, the SDL thermopile is a superior design in applications in which thermopiles are operated exposed to air.

Reference

[1]. Roncaglia A, Mancarella F, Cardinali G C. CMOS-compatible fabrication of thermopiles with high sensitivity in the 3–5μm atmospheric window. Sensors and Actuators B: Chemical, 2007, 125(1): 214-223.

[2]. Du C H, Lee C K. Optimization criteria of CMOS-compatible thermopile sensors, Asia Pacific Symposium on Microelectronics and MEMS. International Society for Optics and Photonics (SPIE 3893), 1999: 116-126.

[3]. Xu D, Xiong B, Wang Y. A CMOS compatible micromachined thermopile IR sensor with high sensitivity. Electrochemical and Solid-State Letters, 2010, 13(9): J106-J109.

[4]. Wu H, Grabarnik S, Emadi A, et al. Characterization of thermal cross-talk in a MEMS-based thermopile detector array. Journal of Micromechanics and Microengineering, 2009, 19(7): 074022.

[5]. Wu H, Emadi A, Grabarnik S, et al. Static and dynamic analysis of thermal cross-talk in an thermopile detector array for use in an microspectrometer. Procedia Chemistry, 2009, 1(1): 1139-1142.

[6]. Socher E, Degani O, Nemirovsky Y. Optimal design and noise considerations of CMOS compatible IR thermoelectric sensors. Sensors and Actuators A: Physical, 1998, 71(1): 107-115.

[7]. Kingston R H. Detection of optical and infrared radiation, Berlin and New York, Springer-Verlag (Springer Series in Optical Sciences. Volume 10), 1978. 150 p. 1978, 10.

[8]. Xie J, Lee C, Feng H. Design, fabrication, and characterization of CMOS MEMS-based thermoelectric power generators. Microelectromechanical Systems, Journal of, 2010, 19(2): 317-324.

[9]. Ford J M. Al/Poly Si specific contact resistivity. Electron Device Letters, IEEE, 1983, 4(7): 255-257.

[10]. Sharpe Jr W N, Pulskamp J, Gianola D S, et al. Strain measurements of silicon dioxide microspecimens by digital imaging processing. Experimental Mechanics, 2007, 47(5): 649-658.

[11]. van der PAUYV L J. A method of measuring specific resistivity and Hall effect of discs of arbitrary shape. Philips Res. Rep., 1958, 13: 1-9.

[12]. Proctor S J, Linholm L W, Mazer J A. Direct measurements of interfacial contact resistance, end contact resistance, and interfacial contact layer uniformity. Electron Devices, IEEE Transactions on, 1983, 30(11): 1535-1542.

[13]. Wang Z, Leonov V, Fiorini P, et al. Realization of a wearable miniaturized thermoelectric generator for human body applications. Sensors and Actuators A: Physical, 2009, 156(1): 95-102.

[14]. Wu H, Emadi A, Sarro P M, et al. A surface micromachined thermopile detector array with an interference-based absorber. Journal of Micromechanics

and Microengineering, 2011, 21(7): 074009.

[15].   Xu D, Xiong B, Wang Y, et al. Integrated micromachined thermopile IR detectors with an XeF2 dry-etching process. Journal of Micromechanics and Microengineering, 2009, 19(12): 125003.

Chapter III: Study of a thermopile infrared sensor and its temperature dependent characteristics

As introduced in Chapter I, one of the most representative applications of thermopile is IR sensor. By connecting two metals or semiconductors with different Seebeck coefficients, a thermocouple can be formed. A series of connected thermocouples is called a thermopile. Since the thermopile is a passive sensor and can generate thermoelectric voltage due to received IR radiation energy; it has a great advantage over the other three kinds of IR sensors. Unlike the quantum type IR sensor, thermopile does not demand a cooler to maintain a very low working temperature. Furthermore, thermopile sensors can work at high temperature without constraints. This advantage provides possibility to apply thermopile IR sensor in high temperature circumstances, e.g. down-hole drilling system.

In this chapter we have studied the structure improvement of the thermopile presented in the previous chapter. In Chapter 3.1, the SDL thermopile was used to build an IR sensor with an integrated wavelength selective absorber. In addition, to explore the feasibility of using a thermopile-based IR sensor in a harsh environment, e.g., for oil gas-sensing applications, I explore the temperature-dependent characteristics of a

heavily doped poly-Si thermopile structure using CMOS materials.

3.1 Design of the thermopile IR sensor

As introduced in Chapter II, the output of voltage of a thermopile depends on the temperature difference of hot junction and cold junction. In the design of an infrared sensor using a thermopile structure, the hot junction is typically close to an infrared absorber, which absorbs power from infrared radiation and converts it to heat. This causes a temperature increase at the hot junction. The cold junction is typically connected to a heat sink, e.g., a single crystal silicon substrate, which is at ambient temperature. In order to achieve a significant temperature difference between the cold junction and the hot junction, these two junctions should be isolated. One of the most widely used structures to isolate them is a suspended structure, which is what I used in my work.

3.1.1. Study on the materials used to build the thermopile

According to the equations provided in the Chapter II, the properties of the materials used for the thermocouple are crucial to the performance of the thermopile-based IR sensor. The efficiency of a thermoelectric material is determined by the dimensionless figure of merit, ZT [1],

$$ZT = \frac{\alpha^2}{\rho K}T,$$
(3. 1)

where α is the Seebeck coefficient, defined as the thermoelectric voltage produced per degree of temperature difference, ρ is the electrical resistivity, K is the thermal conductivity, and T is the temperature of the sensor [2,3].

Among the reported thermoelectric materials used in thermopiles, Bi_2Te_3 and Sb_2Te_3 are well-known n- and p-type materials that generate the highest figure of merit, i.e., ZT, within 200°C. However, these materials are not CMOS compatible. Thus, these two materials cannot be integrated into standard CMOS manufacturing lines. Although some thin-film metal materials, e.g., nickel and chromium, are also used in thermopiles, their low Seebeck coefficient limits them from achieving high performance. Recently, semiconductor-based thermopiles have been presented using germanium (Ge), silicon carbide (SiC) and poly-Si, which can be fabricated using a CMOS-compatible process. J. Xie et al. have studied the thermoelectric properties of heavily doped poly-Si at room temperature [4].

In this Chapter a study of the thermoelectric properties of heavily doped poly-Si up to 300°C is conducted to demonstrate the thermopile performance at different temperatures.

I studied heavily doped poly-Si because of its good thermoelectric performance [5]. The implantation conditions of the poly-Si test structures used in the experiment are the same as those introduced in Chapter II. The thickness of the poly-Si is 300 nm. To

study the electric resistivity of the heavily doped poly-Si, we used a van-der-Pauw structure, the same as what is introduced in Chapter II.

The Seebeck coefficient and thermal conductance were determined by a cantilever test structure, the same as shown in Figure 2.7. Using the same method introduced in Chapter II, we obtained the thermoelectric properties of the heavily doped poly-Si. These thermoelectric properties are shown in Table 3.1.

Figure 3.1 shows the average measurement results of the Seebeck coefficient of the n- and p-type poly-Si from four different test keys with the same design. According to Figure 3.1(a), the magnitude of the Seebeck coefficient of the p-type heavily doped poly-Si increases with temperature, but it becomes saturated and begins to decrease at temperatures greater than 250°C. A significant increase in the Seebeck coefficient of p-type heavily doped poly-Si from -50°C to 250°C can be observed. The increase in the Seebeck coefficient of the p-type heavily doped poly-Si is over 400% at 300°C relative to 0°C. Figure 3.1(b) shows the calculated Seebeck coefficient of the n-type heavily doped poly-Si. Likewise, the magnitude of the Seebeck coefficient of the n-type heavily doped poly-Si increases greatly with temperature initially, then saturates and decreases above 250°C. The Seebeck coefficient of the n-type heavily doped poly-Si does not increase as rapidly as that of the p-type. The magnitude of the Seebeck coefficient increases by only approximately 150% for n-type poly-Si.

To express the relationship between the Seebeck coefficient of the heavily doped n- and p-type poly-Si and temperature, a cubic polynomial curve was applied to fit the data. The solid lines in Figure 3.1 represent the fitted cubic polynomial curve.
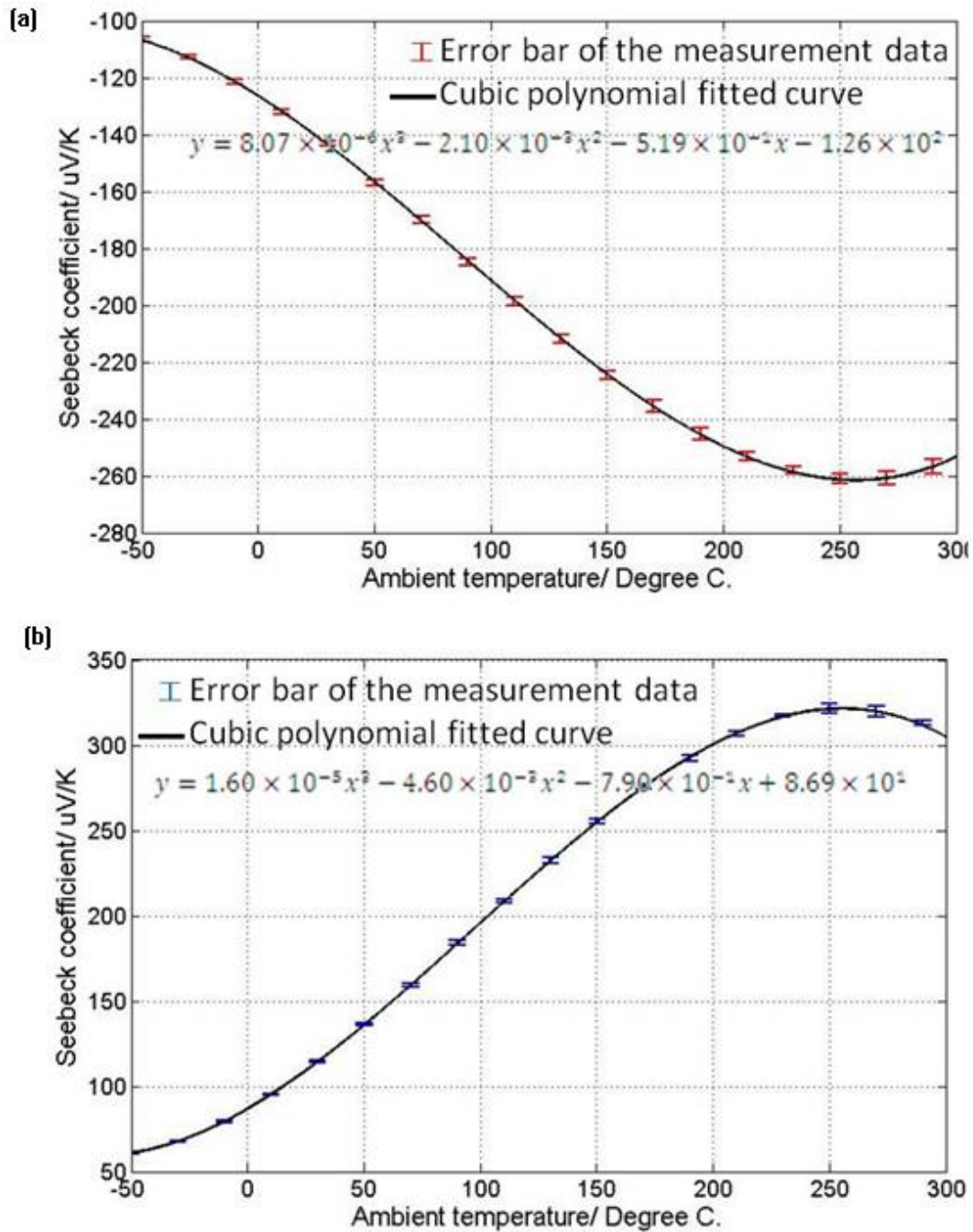
Figure 3.1. Seebeck coefficient of p-type (a) and n-type (b) heavily doped poly-Si at different temperatures.

The results show that the thermal conductivity of the heavily doped poly-Si does not

change significantly with temperature. The electrical resistivity at room temperature, TCR, Seebeck coefficient at room temperature and thermal conductivity are shown in Table 3.1.

Table 3.1. Thermoelectric properties of the heavily doped poly-Si at room temperature.

	Electric resistivity ($\mu\Omega m$)	TCR (%/K)	Seebeck coefficient ($\mu V/K$)	Thermal conductivity (W/mK)
p-type	13.7	-0.17	137	33.6
n-type	8.9	-0.22	−118	31.9

3.1.2 Design and configuration of the thermopile IR sensor

We use an SDL thermopile, which was introduced in Chapter II, to optimize the performance of the thermopile IR sensor. Figure 3.2(a) shows a cross-beam-like thermopile, which is comprised of an interferometric absorber. The absorber, which absorbs the infrared radiation, is placed on the central part of the cross, leading to an increase in temperature at the hot junction.

The entire thermopile is suspended on a thin SiO_2 membrane. The suspended structure allows the heat transfers only through the thermopile, which connects the hot junction and the cold junction. The silicon substrate connected to the end of the cross has high thermal conductance and a large thermal mass to maintain a relatively constant temperature at the cold junction. As a result, when the device is exposed to IR

radiation, there will be a temperature difference between the hot junction and the cold junction, leading to a voltage drop between these two junctions. The voltage drop could be read out from the contact pads.
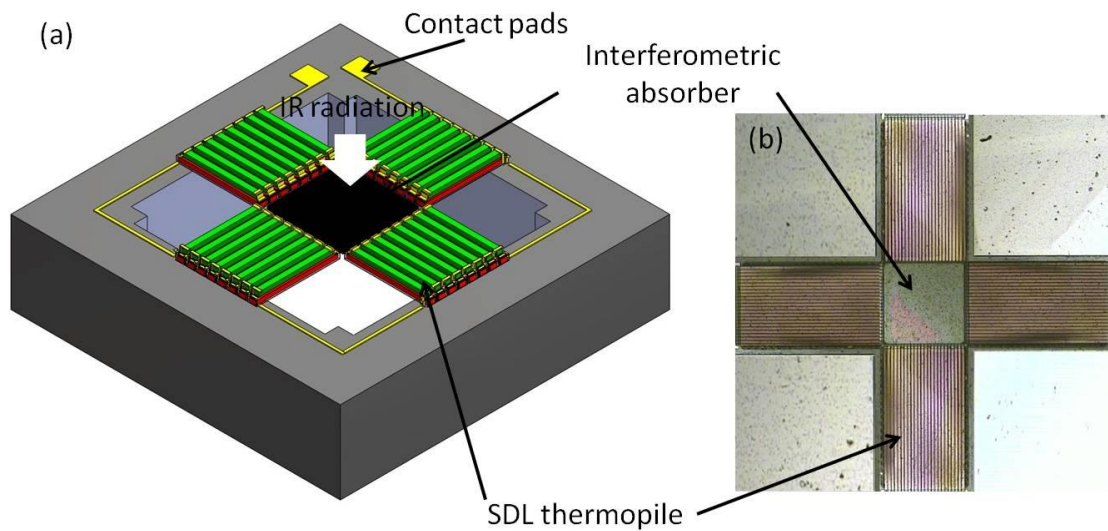
Figure 3.2. Diagram of the SDL mid-IR sensor (a) and an optical microscope photograph of the IR sensor after release (b).

The structure of the interferometric absorber will be discussed in Chapter V. According to Chapter II, the optimal dimension parameters are as follows: the length of the thermopile is 600 μm, the width of the thermopile is 12 μm and the number of thermopiles is 96. The thickness of the poly-Si strips is 300 nm, and the thickness of the SiO_2 electrical isolation layer is 150 nm.

3.1.3 Study on the thermopile mid-IR sensor at different temperatures

According to the measurement results of the thermal conductivity, Seebeck coefficient and electric resistivity, one may predict that the performance of the thermopile improves with temperature up to at least 250°C. However, according to Equation 2.5, the energy received by the sensor will decrease at an increase of the ambient temperature if the source temperature is fixed and that Equation 2.3 shows a decrease of output signal in proportional to the absorbed power received by the sensor.
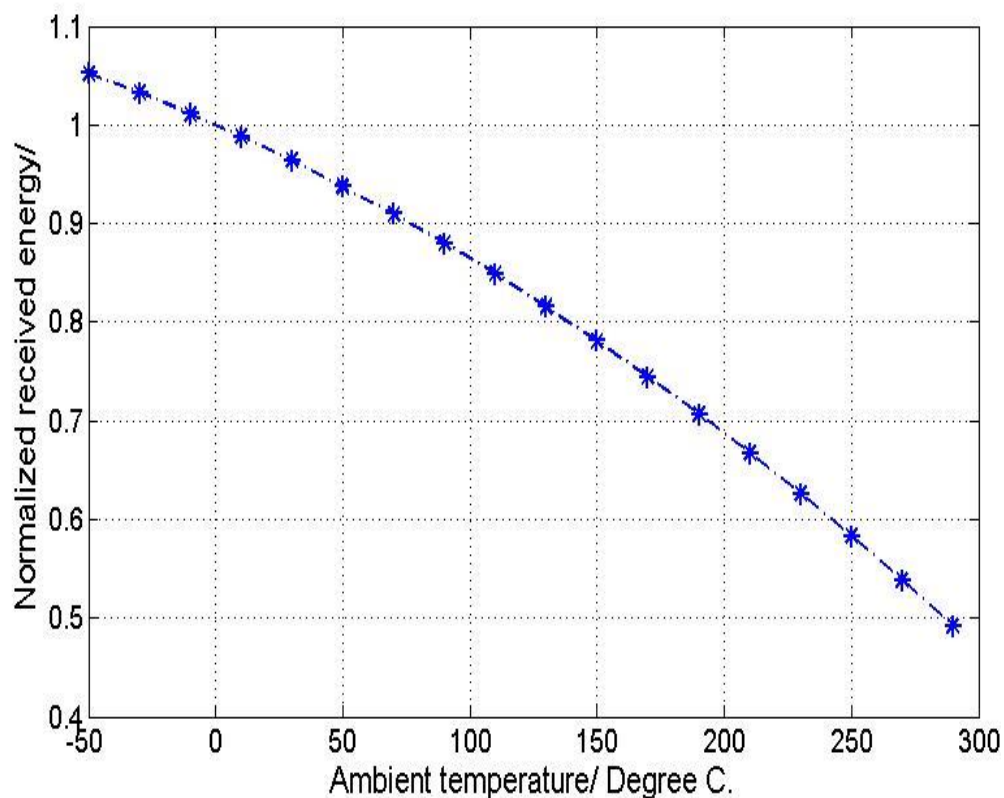
Figure 3.3. Normalized energy received by the mid-IR sensor at different temperatures.

A theoretical investigation of the energy received by the mid-IR sensor at different ambient temperatures was conducted by using the Stefan-Boltzmann law. The simulation results are normalized to the value of the energy received by the sensor at 0°C. The data shown in Figure 3.3 indicates that the energy received by the mid-IR sensor decreases significantly with increasing ambient temperature.

As illustrated by the above discussion, there is a trade-off between the performance of the thermopile structure and the energy received by the sensor. Therefore, it is reasonable to predict that there could be an optimal ambient temperature at which the sensor output voltage reaches its highest value. A simulation was conducted to predict this balance point. The material properties applied in the simulation come from the measurement data presented in Chapter 3.2, and the dimensions of the structure are the same as those presented in Chapter 3.2. The source temperature is fixed at 470°C, the same temperature used in the experiment introduced in Chapter 3.4. As shown in Figure 3.4, the output voltage begins to decrease when the ambient temperature is approximately 200°C.
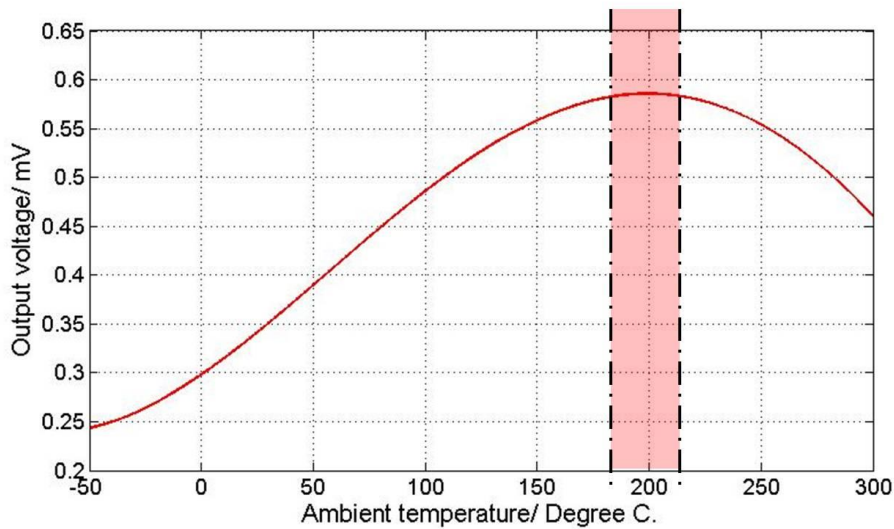
Figure 3.4. Simulation results of the thermopile mid-IR sensor at different temperatures.

3.1.4 Micro-fabrication process

Figure 3.5 shows the micro-fabrication process flow of the wavelength-selective thermopile-based IR sensor. The starting substrate is an 8'' silicon wafer with a thickness of 725 μm. Firstly, n/p-type poly-Si strips are deposited and structured with a thickness of 300 nm. The implantation condition is the same as that described in Chapter II. PECVD SiO_2, with a thickness of 150 nm, is deposited as an electrical insulation layer between the n- and p-type poly-Si and on top of the entire wafer [Figure 3.5(a)]. Then, the contact holes on the poly-Si strip are opened. After the contact holes are opened, a heavy implantation is conducted to reduce the contact resistance between poly-Si and Al. The implantation conditions are described in Chapter II.

a) Deposit and structure n/p-type poly-Si using PECVD SiO$_2$ as electric isolation

b) Open contact holes on the poly-Si, implement contact implantation and deposit Al to make a connection between the n/p-type poly-Si

c) Release the membrane with XeF$_2$ after DIRE of 10μm Silicon.

d) Seal the whole device with 2μm PECVD low stress SiO$_2$

e) Deposit the Al/A-Si/TiN three-layer interferometric mid-IR absorber

f) Define the area of absorber at the central part of the sensor structure

Si substrate   N-type Poly-Si   P-type Poly-Si   Aluminum   LPCVD SiO$_2$

Interferometric absorber

Figure 3.5. Micro-fabrication process flow for the thermopiles.

Afterwards, an Al layer was deposited by sputtering and patterning to form metal interconnections between the n- and p-type poly-Si strips. To establish good ohmic contact between the Al and poly-Si, the wafer is annealed at 420°C for 30 min [Figure 3.5(b)]. To confine the heat flux within the thermopile beams, the entire device is released with (Xenon difluoride) XeF$_2$ to form a cavity after the deep silicon trenches via deep reactive ion etching (DRIE) based on SF$_6$ and C$_4$F$_8$ gases for 10 μm [Figure 3.5(c)]. Following the release step, 2 μm PECVD SiO$_2$ is deposited to seal the release hole so that the mechanic strength is enhanced to support the further fabrication of the interferometric absorber [Figure 3.5(d)]. The pressure used in the PECVD process is

approximately 0.5 mbar, which makes the space essentially a vacuum. Therefore, the thermal conductance from the air is also minimized by the sealing process.

After the sealing process, the stacked three-layer absorption structure is deposited in the central part of the IR sensor, with the dimensions provided in the previous section [Figures 3.5(e) and (f)].

3.2 Experimental results

3.2.1 Electrical measurement

To characterize the thermopile-based IR sensor, the features of the thermopile structure must be measured at the first time. The testing setup is the same as what was introduced in Figure 2.8.

A bias voltage is applied from -5 V to 5 V in increments of 0.1 V to obtain the electrical response from the thermopile structure. The input voltage can be converted into input power using Equation 2.28 as introduced in Chapter II.

The responsivity of the thermopile can be calculated by substituting P_{in} and the measured output voltage, V_{out}, into Equation 2.3. The calculation results are shown in Figure 3.6. The dotted points are the measured responsivities, and the solid line is the simulated data.
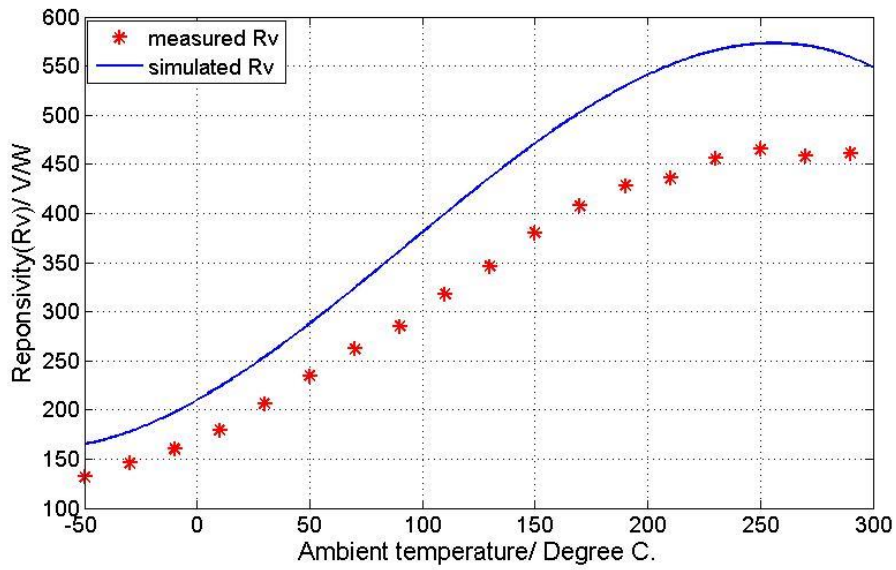
Figure 3.6. Electrical measurement and simulation results of the SDL thermopile.

The simulation was conducted by using the theory and the material properties described in Chapter II. The thermal conductivity of poly-Si is also discussed in Chapter II, and the Seebeck coefficient used in this simulation is that of the fitted cubic polynomial curve.

As shown in Figure 3.6, the responsivity of this thermopile mid-IR sensor varies from 130 to 463 V/W within the temperature range of -50°C to 300°C. In addition, the responsivities in the measurement and simulation results increase with temperature and decrease slightly after the temperature reaches 250°C. The highest responsivity, at an ambient temperature of 250°C, is approximately 350% of the lowest responsivity at -50°C. The simulated responsivity and the measured responsivity exhibit the same trend, but the simulated responsivities are slightly higher than the measured values.

This difference may be due to thermal cross talk between thermocouples, which is not considered in the simulation [6].

3.2.2 IR radiation measurement

After the electrical measurements, the measurement of thermopile-based IR sensor was conducted. The measurement setup is same as the setup shown in Figure 2.8. A blackbody IR source with a temperature of 470°C was fixed at the top of the vacuum chamber with a Zinc selenide (ZnSe) window. According to Planck's curve, the radiation peak is approximately 3.9 μm, which matches the design of the absorber. The IR transmission of the ZnSe window is approximately 80% to ensure that the response of the IR sensor is sufficiently large to be detected. To prevent areas other than the absorber in the detector chip from receiving an excessive amount of radiation from the blackbody, a piece of aluminum foil with a 0.4 mm by 0.4 mm open hole was placed on top of the chip, as shown in Figure 2.8. The blackbody IR source was equipped with a chopper. The experiment was conducted with a chopper frequency from 2 to 512 Hz, so that the time constant could be obtained from the IR measurement results. The IR measurements were conducted 1,000 times to test the working stability of the IR sensor. The time constant was determined based on the time required to reach 63% of the maximum detector output voltage [4]. According to the IR measurement results at room temperature (as shown in Figure 3.7), the cut-off

frequency is approximately 30 Hz, which means that the time constant is approximately 33 ms; the time constant is determined by the thermal conductance or resistance and thermal capacitance based on Equation 3.2:

$$\tau = R_{ther} \times C_{ther} \ , \tag{3.2}$$

Here, τ is the time constant, R_{ther} is the thermal resistance and C_{ther} is the thermal capacitance. The time constant as calculated by Equation 3.2 is 32.4 ms, which is close to the measured result.
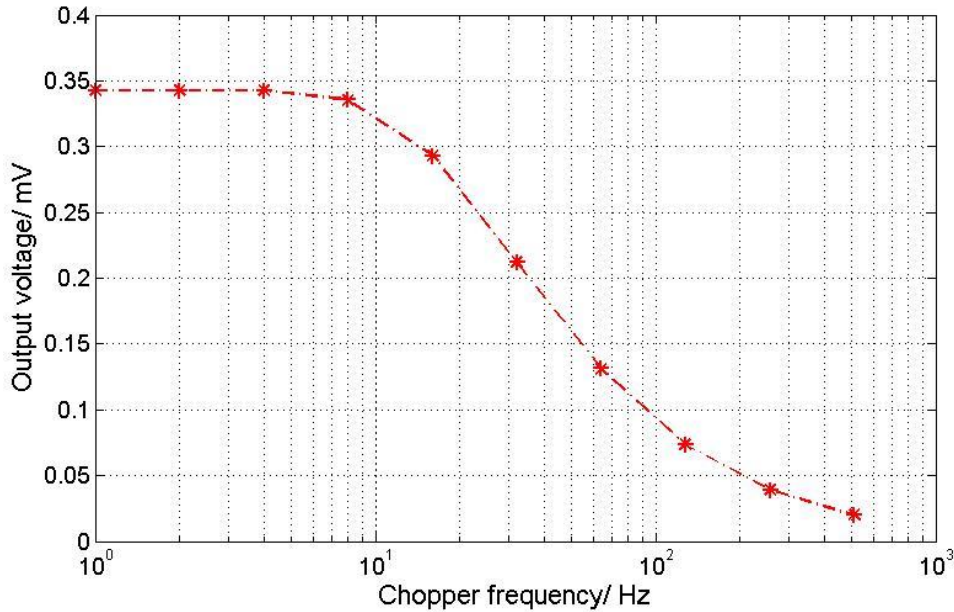
Figure 3.7. IR measurement results of the thermopile at room temperature.

To determine the detectivity of the mid-IR sensor, measurements of noise at different working temperatures were obtained, and the results are shown in Figure 3.8. According to the thermopile theory discussed in Chapter II, there is only Johnson

99

noise, which can be calculated by Equation 2.24. The measured overall electric resistance of the thermopile structure is 610 kΩ, and the theoretical noise at room temperature is estimated to be 0.2 $\mu V/\Delta f^{1/2}$. The electric bandwidth is given as 400 Hz for the Digital Analyzer 5000a (Agilent). We do not focus on the improvement of read-out circuit design here, thus, the optimized electric bandwidth of the read-out circuit is not explored. Generally speaking, when the optimized electric bandwidth of the readout circuit is limited to approximately 1 Hz, the noise is considerably less, and D^* can be one order of magnitude higher than the measured value. Using the measured noise shown in Figure 3.8 and the measured responsivity form Figure 3.6, the specific detectivity, D^*, can be calculated as 3.8×10^6 to 1.3×10^7 cmHz$^{1/2}$W^{-1} from -50ºC to 300ºC, as shown in Figure 3.9.
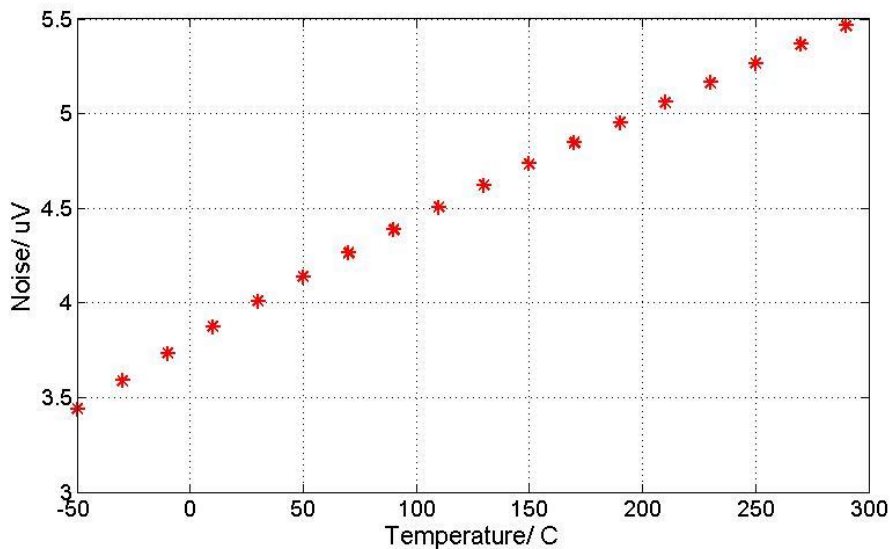
Figure 3.8. Noise of the thermopile mid-IR sensor at different temperatures.
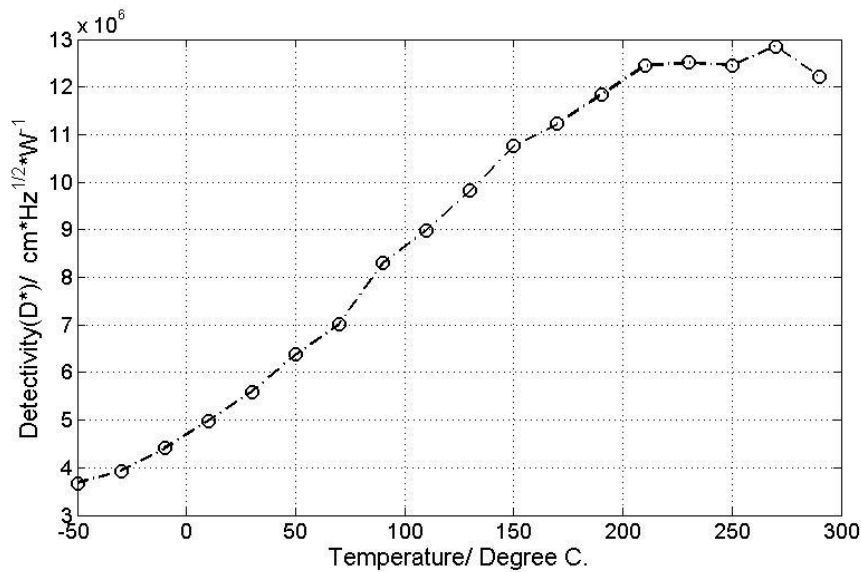
Figure 3.9. Calculated detectivity of the thermopile at different temperatures.

3.2.3 IR radiation measurements at different temperatures

According to the discussion at the end of section 3.2, the ambient temperature can be optimized to obtain the maximal output signal when the source temperature is fixed. This optimization is possible because the performance of the thermopile structure improves with temperature but the radiation strength decreases as the device temperature increases. To verify this prediction and find an optimal device temperature, an experiment with a blackbody IR source was conducted. The temperature of the blackbody source was 470°C, which is the same as that in the experiment discussed in the previous section.

The measurement results are shown in Figure 3.10. The output voltage decreases when the ambient temperature is greater than 190°C, the thermopile structure

101

provides the highest R_v at 250°C, as shown in Figure 3.6. The solid blue line

represents the simulated results, which are the same as those in Figure 3.4, and the red

stars represent the measurements. The results indicate that the impact of the

increasing thermopile structure performance is less than that of the decreasing

radiation intensity. Thus, the ambient temperature balance point is 190°C when the

source temperature is 470°C.   The small difference between the measurement results

and simulation results is due to the difference between the measured values and fitted

values of the Seebeck coefficient.
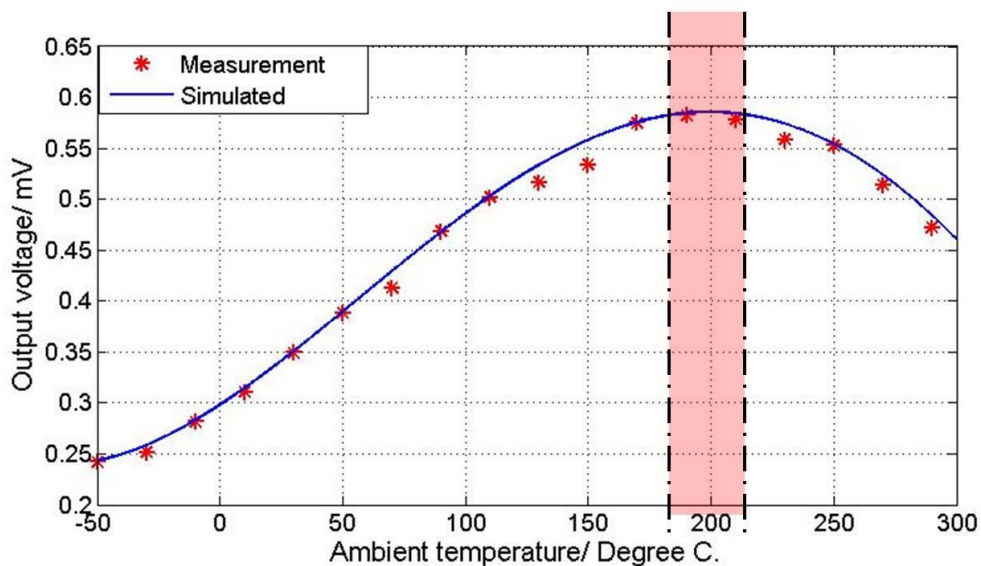
Figure 3.10. IR test and simulated results of the thermopile at different temperatures.

3.3. Conclusion

In   this   Chapter,   a   CMOS-compatible   mid-infrared   wavelength-selective

thermopile sensor comprising of an SDL thermopile and interferometric absorber is

reported. The entire process of design, analysis, micro-fabrication and testing of the SDL thermopile structure and the interferometric absorber are presented. The absorption peak of the three-layer interferometric absorber is approximately 3.9 μm, at which the absorption rate can reach approximately 99%. The study of the thermoelectric properties of heavily doped n- and p-type poly-Si indicates that the thermopile structures perform better at high temperature, which is in agreement with the electrical testing results of the thermopile structure. An experiment involving IR measurement at different temperatures was also conducted to determine the optimized ambient temperature when the source temperature is 470°C. The time constant is derived from the measurement results, and is found to be 33 ms. Considering the output voltage, the fabricated IR sensor yields a maximum value of 0.59 mV at a temperature of 190°C. At this temperature, the responsivity and detectivity are found to be 425.7 V/W and $1.25\times10^{7}\text{cmHz}^{1/2}\text{W}^{-1}$, respectively. These results suggest that the developed thermopile-based mid-IR sensor is useful for operations conducted at approximately 200°C.

Reference

[1]. van der PAUYV L J. A method of measuring specific resistivity and Hall effect of discs of arbitrary shape. Philips Res. Rep., 1958, 13: 1-9.

[2]. Du C H, Lee C K. Optimization criteria of CMOS-compatible thermopile sensors,

Asia Pacific Symposium on Microelectronics and MEMS. International Society for Optics and Photonics, 1999: 116-126.

[3]. Xu D, Xiong B, Wang Y. A CMOS compatible micromachined thermopile IR sensor with high sensitivity. Electrochemical and Solid-State Letters, 2010, 13(9): J106-J109.

[4]. Xu D, Xiong B, Wang Y. Modeling of front-etched micromachined thermopile IR detector by CMOS technology. Microelectromechanical Systems, Journal of, 2010, 19(6): 1331-1340.

[5]. Xie J, Lee C, Wang M F, et al. Characterization of heavily doped polysilicon films for CMOS-MEMS thermoelectric power generators. Journal of Micromechanics and Microengineering, 2009, 19(12): 125029.

[6]. Wu H, Grabarnik S, Emadi A, et al. Characterization of thermal cross-talk in a MEMS-based thermopile detector array. Journal of Micromechanics and Microengineering, 2009, 19(7): 074022.

Chapter IV: Development of a highly sensitive thermopile IR sensor with a phonon-scattering enhanced poly-Si layer

As introduced in Chapter I, although the SiNWs and Si nanomesh are quite promising CMOS-compatible thermoelectric materials, it is challenging to produce them at a large scale or use them in planar thermopile structures, which are the current mainstream configuration.

In addition, the high dependency of SiNWs on nanoscopic surface morphology limits the possibility of using SiNWs to fabricate thermopiles. However, bulk Si is also not perfect for thermoelectric applications because of its high thermal conductivity. As noted in Chapter I, the thermal conductivity of a single crystal of Si with thickness on the order of 100 nm has been studied, yielding a reduction in thermal conductivity of more than 50% to approximately 50 $Wm^{-1}K^{-1}$. This value is still considerably larger than the thermal conductivity of bulk poly-Si, which is approximately 30 $Wm^{-1}K^{-1}$. Because of the phonon-grain-boundary scattering, there is a reduction in thermal conductivity. A portion of the n-type dopants segregates to the grain boundaries in poly-Si, where they also contribute to greater phonon scattering. Advanced CMOS

manufacturing technology can allow features of a few tens of nanometers and thin
poly-Si layers of a few nanometers to be fabricated on a 12" wafer. In view of the
high demand for high-ZT CMOS thermoelectric materials, we investigate
nanometer-thick poly-Si in order to increase ZT based on phonon-boundary scattering.
To test our ideas, we developed a scalable design of thermopile and fabricated it using
a CMOS mass production line based on the nanometer-thick poly-Si with optimized
ZT and device configurations.

4.1 Study of the thermoelectric properties of nanometer-thick poly-Si layer

To investigate how the thickness of a thin poly-Si layer affects ZT, micro-fabricated
test keys were used to study the thermal conductivity, Seebeck coefficient and the
electrical resistivity of the n- and p-doped poly-Si layers. Both of the test key and the
testing setup are the same as the one introduced in Chapter II (Figure 2.7 and 2.8).

The measured thermal conductivities of n- and p-doped poly-Si with different
thicknesses at room temperature are shown in Figure 4.1 (a). The results show that the
thermal conductivity decreases with decrease in the poly-Si thickness.

This phenomenon becomes more significant when the thickness is less than 150 nm.
Using a frequency-dependent relaxation time to demonstrate the effects of
phonon-scattering events, Callaway reported a theoretical model with one

approximate solution to the Boltzmann transport equation for phonons in 1959 [1]. In

1963, Holland improved this method by considering phonon polarization [2].

Furthermore, A. D. McConnell and her colleagues expanded this model by adding in

the study on the effect of grain boundaries and dopant impurities [3].

Both mobile carriers and phonons contribute to the overall thermal conductivity of

poly-Si, as shown in Equation 4.1:

$$k = k_e + k_p, \tag{4.1}$$

where k_e is the thermal conductivity induced by electrons and k_p is the thermal

conductivity induced by phonons. According to the Wiedemann–Franz law, k_e at a

certain temperature, T, can be defined by Equation 4.2:

$$k_e = \frac{\pi^2 K_B^2 T}{3q^2 \rho}, \tag{4.2}$$

where K_B is the Boltzmann constant, q is the electron charge and ρ is the electric

resistivity of poly-Si. Because the electrical resistivity of doped poly-Si is on the order

of 10^{-5} Ωm [4], the estimated value of k_e is less than 1 Wm^{-1}K^{-1}, which is not

significant compared to the overall thermal conductivity.
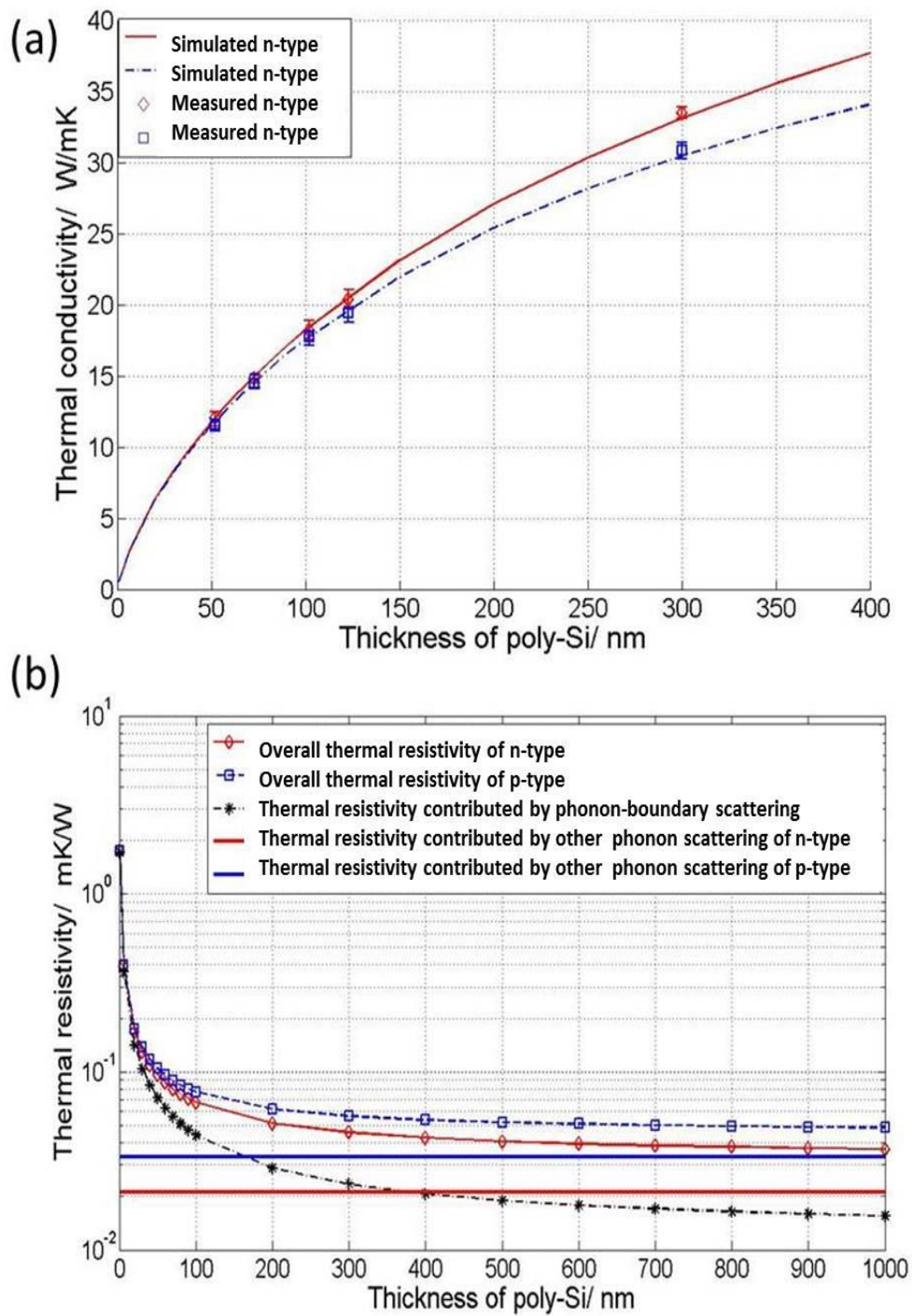
*Figure 4.1. Measured and simulated thermal conductivities of nanometer-thick poly-Si (a); and
thermal resistivity of poly-Si influenced by different types of phonon scattering (b) versus poly-Si
thickness.*

Using Callaway and Holland's model, the thermal conductivity induced by phonons,

k_p, can be calculated with Equation 4.3 below:

$$k_p = \frac{1}{3}\left(\frac{k_B T}{h/2\pi}\right)^3 \frac{k_B}{2\pi^2} \sum_{j=L,TO,TU} \frac{1}{v_j} \int_0^{\theta_j/T} \frac{x_\omega^4 e^{x\omega}\tau_j}{(e^{x\omega}-1)^2} \, dx_\omega. \qquad (4.3)$$

In this equation, x_ω is the dimensionless phonon angular frequency, which is defined

as $x_\omega = h\omega/2\pi K_B T$, h is Planck's constant, k_B is the Boltzmann constant, T is the

temperature and τ_j is the phonon relaxation time. This method presents the phonon

scattering events in a longitudinal model and a transverse model; the transverse model

is divided into a low-frequency model and high-frequency model. The symbols L, TO

and TU in Equation 4.3 refer to the longitudinal model, the low-frequency transverse

model and the high-frequency transverse model, respectively. The variable v_j is the

phonon group velocity in different modes. In silicon, v_L =8.84×10³ m/s,

v_{TO}=5.86×10³ m/s and v_U=2.0×10³ m/s.

The relaxation time τ_j for each model contains several phonon scattering events, as

shown in Equation 4.4:

$$\tau_j^{-1} = \sum_i \tau_{j,i}^{-1}. \qquad (4.4)$$

There are mainly phonon-phonon scattering, phonon-electron scattering,

phonon-boundary scattering and mass-difference impurity scattering [5]. Compared to

the other three factors, phonon-electron scattering is negligible [6]. Furthermore,

phonon scattering on a grain boundary and in segregated dopants also contribute to

the relaxation time in case of the doped poly-Si. Because the thickness that was used

is considerably less than the average mean free path of a phonon (~300 nm at room
temperature), the phonon-boundary scattering should be the key factor in this study.
Therefore, we focus on the study of the influence of phonon-boundary scattering. The
phonon relaxation time induced by phonon-boundary scattering is shown in Equation
4.5:

$$\tau_{boundary}^{-1} = \frac{v_s}{d}\left(\frac{1-p}{1+p}\right), \tag{4.5}$$

where d is the thickness of the poly-Si, v_s is an averaged phonon group velocity,
which can be defined as $v_s^{-1} = \frac{\frac{2}{v_{TO}}+\frac{1}{v_L}}{3}$, and p is a parameter with a value between 1
and 0, representing the surface roughness, which is the likelihood of specula being
reflected from the sample boundary. A value of $p=1$ corresponds to a perfectly smooth
surface that reflects all incoming phonons, whereas $p=0$ represents an entirely rough
surface that diffusely scatters all incident phonons like a blackbody.

The other phonon-scattering events were provided by Holland[2], as shown below.
The first one is Umklapp phonon-phonon scattering events[2]. Equation 4.6 describes
the phonon relaxation time induced by the phonon-phonon scattering events:

$$\tau_{Umklapp}^{-1} = 2\gamma^2 \frac{k_B T \omega^4}{\mu V_0 \omega_D}, \tag{4.6}$$

where γ is the Gruneisen anharmonicity parameter, μ is the shear modulus, V_0 is the
volume per atom, ω_D is the Debye frequency, T is the ambient temperature and ω is
the phonon angular frequency.

The second one is mass-difference impurity scattering events[7]; the phonon
relaxation time induced by this event is describe by Equation 4.7:

$$\tau_{defect}^{-1} = \frac{nV^2\omega^4}{4\pi v_s^3}\left(\frac{\Delta M}{M}\right)^2, \tag{4.7}$$

where v_s is an averaged phonon group velocity, n is the dopant concentration, V is the volume of the host (silicon) atom, M is the silicon atomic mass, and ΔM is the difference between the host and impurity atomic masses.

Another one is phonon-to-grain boundary scattering events[3]; the phonon relaxation time induced by this event is describe by Equation 4.8:

$$\tau_{grain}^{-1} = \int_0^d \frac{v_s}{d_g(z)} \left(\frac{1-p_{tr}}{1+p_{tr}}\right) d, \tag{4.8}$$

where $d_g(z)$ is the grain size at thickness z, p_{tr} is the probability of specular transmission ($0 \leq p_{tr} \leq 1$).

The last one is segregated dopants induced scattering events[7]; the phonon relaxation time induced by this event is describe by Equation 4.9:

$$\tau_{segragated\ dopants}^{-1} = \int_0^d \frac{2v_s}{\pi d_g(z)} \left\{1 + \left[e^{\left(\frac{\pi}{2}\right)^2 \delta(\omega,z)} - 1\right]^{-1}\right\}^{-1} dz, \tag{4.9}$$

where $\delta(\omega, z)$ is the grain boundary scattering strength.

Table 4.1. The parameters used for simulation.

Temperature (K)	Doping concentration (cm⁻³)	Maximum grain size (nm)	Minimum grain size (nm)
300	3×10^{19}	400	100

With the above-mentioned equations, we conducted a simulation to determine the thermal conductivity of poly-Si using Matlab 2010b. The simulation results of thermal conductivity for n- and p-doped poly-Si of different thicknesses are also shown in Figure 4.1(a). The thermal conductivity of n- and p-doped poly-Si decreases as the thickness of the poly-Si layer decreases. The results are in good agreement with the measured data. Equation 4.5 indicates that the phonon relaxation time induced by the phonon-boundary scattering event is inversely proportional to the thickness of the

111

poly-Si.

To understand how the phonon-boundary scattering affects the overall thermal
conductivity, a simulation of phonon-boundary scattering was used to determine its
contribution to the overall thermal conductivity relative to other phonon-scattering
events. Figure 4.1(b) shows the contribution of phonon-boundary scattering to the
overall thermal conductivity as compared to other phonon scattering events. The
thermal resistivity is dominated by the phonon-boundary scattering when the
thickness of poly-Si layer is less than 100 nm, and the other phonon-scattering events
are not affected by changes in the poly-Si layer thickness.

The electrical resistivity and Seebeck coefficients of poly-Si layers with different
thicknesses were also measured, and the results are shown in Figure 4.2 (a) and (b).
The results suggests that these two parameters are intrinsic properties that are subject
to doping concentration and they do not change with the poly-Si thickness. According
to the calculated *ZT* (Figure 4.2(c)), the n-doped poly-Si has a considerably higher *ZT*
than the p-doped poly-Si among measured data of all 5 types of thickness variation in
this experiment. This is because the n-doped poly-Si has a relatively low electrical
resistivity and a high Seebeck coefficient compared to p-doped poly-Si. In addition,
the trend of the change in *ZT* with poly-Si thickness reflects the trend of the change in
thermal conductivity with regard to the poly-Si thickness, as shown in Figure 4.2(a).
Maximum *ZT* values of 0.067 and 0.024 are obtained for the 52 nm-thick n- and

p-doped poly-Si layers, respectively. These results correspond to a 116% and 92%

increase in *ZT* when the thickness of the poly-Si layer decreases from 300 to 52 nm.

The *ZT* of bulk poly-Si is approximately 0.01 because of its relatively high thermal

conductivity (~30 Wm^{-1}K^{-1}) [7,9]. A comparison of the thermoelectric properties

obtained in this work and those from studies is shown in Table 4.2.
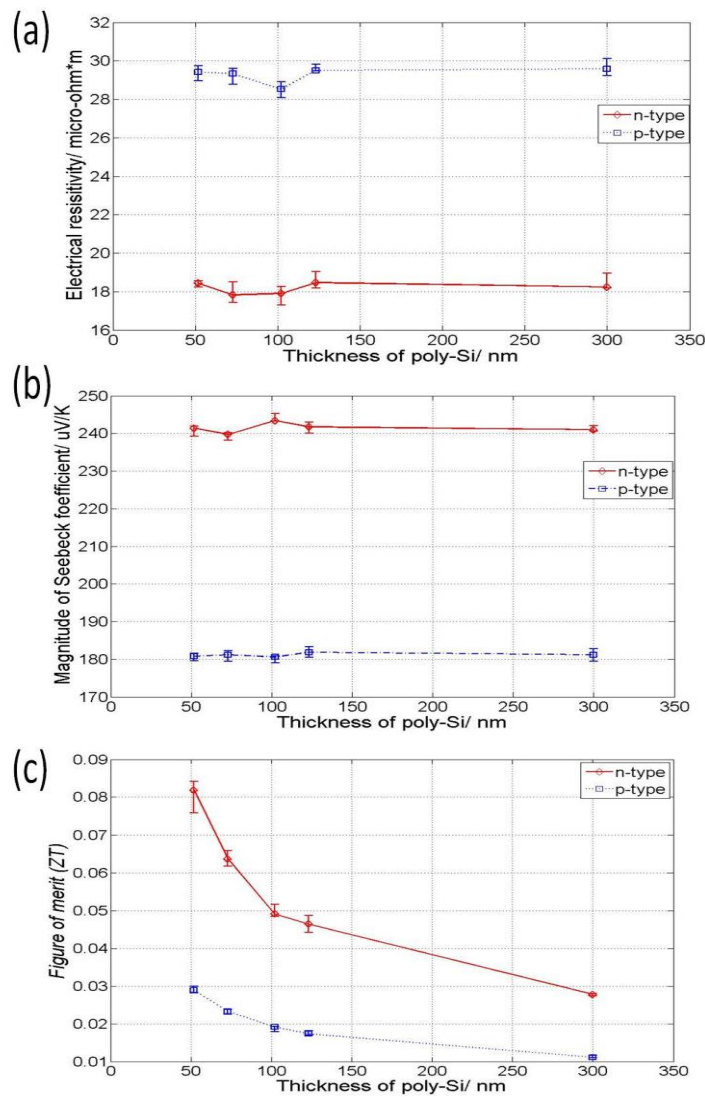
*Figure 4.2. Electrical resistivity (a) Seebeck coefficient (b) and ZT (c) measured at room
temperature.*

113

*Table 4.2. Comparison of the thermoelectric properties measured in this work
to other studies.*

Poly-Si type	**Thermal conductivity (W/mK)**	Seebeck coefficient (μV/K)	Electrical resistivity (μΩm)	Figure of merit ZT	Details
n-type	**12.1**	-242.1	18.3	0.067	This work: t=52 nm, heavily doped
	31.5	-57	8.1	0.004	Bulk, t>1μm, intrinsic[7]
	29.7	-110	8.9	0.014	Bulk, t~700 nm, heavily doped [9]
p-type	**12.0**	182.3	28.9	0.024	This work: t=52 nm, heavily doped
	31.2	103	22.1	0.005	Bulk, t>1 μm, intrinsic[7]
	28.4	130	13.7	0.012	Bulk, t~700 nm, heavily doped [9]

4.2 Design and experiment on the thermopile IR sensor using nanometer-thick poly-Si

4.2.1 Design and fabrication of a thermopile IR sensor using nanometer-thick poly-Si

Based on the above discussion of the nanometer-thick poly-Si thermoelectric data, a thermopile using a nanometer-thick poly-Si layer was developed and characterized for this section. Figure 4.3 shows a diagram of a thermopile that has a cross-like suspended membrane structure with an IR absorber built on the center square area. When the thermopile is exposed to IR radiation, the central absorber area absorbs the radiation and turns the radiation power into heat. The heat causes a temperature rise in the central part of the thermopile, and this part is defined as the hot junction of the thermocouples. The other end of the thermocouple in the thermopile is connected with the single crystalline Si substrate and is maintained at room temperature during the measurement because of the high thermal conductance and the large thermal mass of the Si substrate. As a result, there is a temperature difference between the hot junction and the cold junction; the difference creates a self-generated voltage between the two ends of the thermopile.
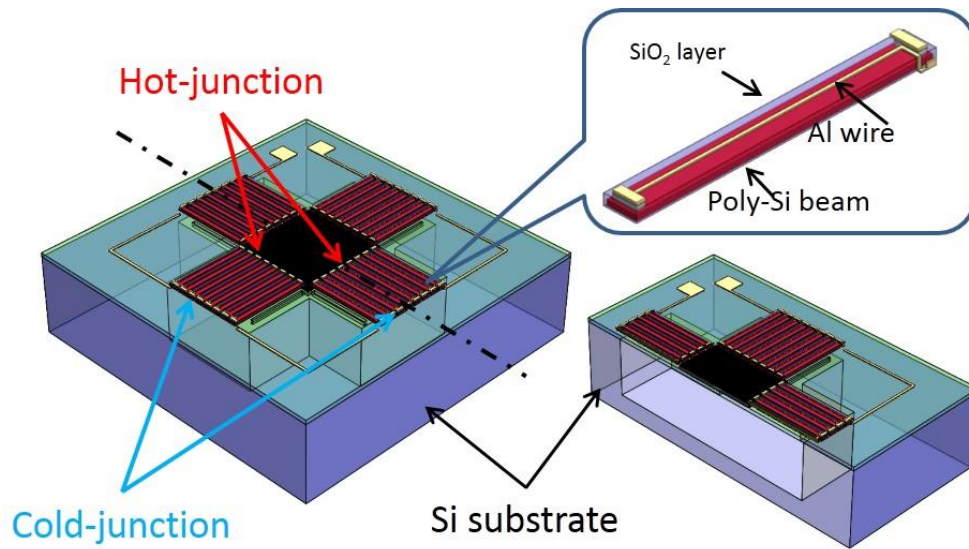
Figure 4.3. Schematic drawing of the IR sensor and single thermocouple.(not to scale).

Figure 4.3 illustrates the IR sensor and a single thermocouple (not to scale). The

thermopile comprises 128 pairs of thermocouples connected in series, and a diagram

of a single thermocouple is shown in Figure 4.3. The doped poly-Si strips are built at

the bottom as one of the materials from the thermocouple, Al is the other material that

forms an electrical connection between each thermocouple. According to the Seebeck

effect, the temperature difference between the two ends of the thermocouples will

induce a voltage drop, which can be read from the contact pads.
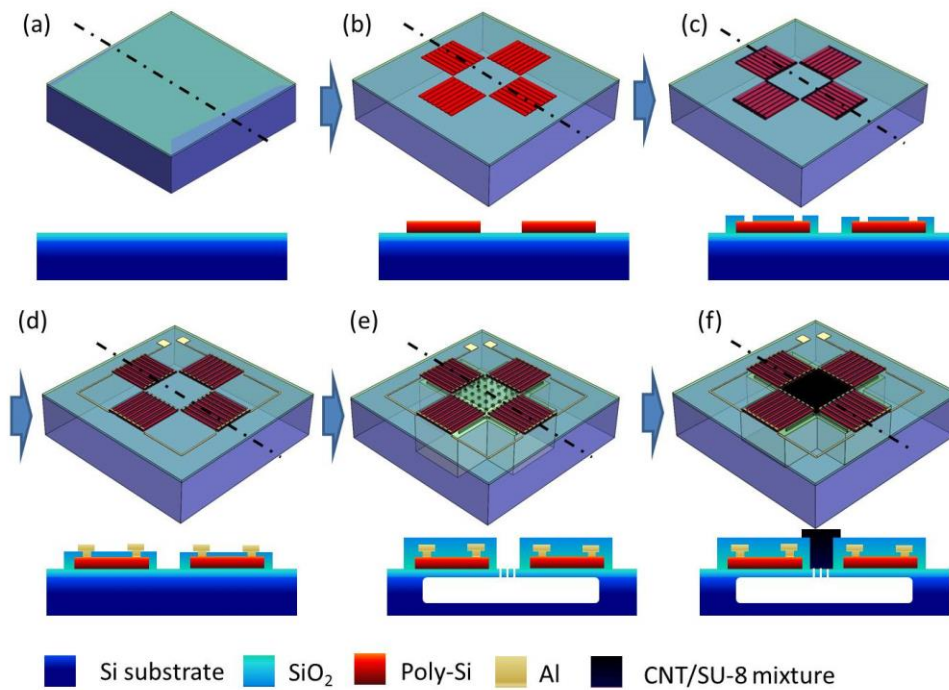
Figure 4.4. Process flow of the device. The process starts with a Si substrate covered by LPCVD SiO$_2$ (a); A poly-Si strip is deposited, doped and patterned (b); Then, a SiO$_2$ electrical isolation layer is deposited, and contact is opened (c); The Al wire is deposited and patterned (d); The SiO$_2$ passivation layer is doped, and the contact pad is opened, followed by the release with XeF$_2$ (e); A CNT/SU-8 IR absorber was deposited at the end of process(f).
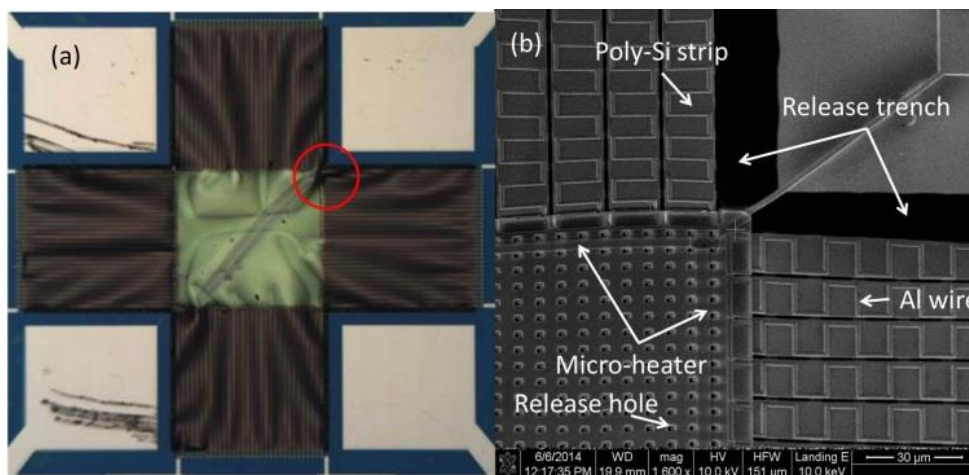
Figure 4.5. Optical microscope image of the thermopile structure without an absorber coating (a); SEM image of the zoomed-in view (b).

A fabricated device is shown in Figure 4.5. The parts that seem unsmooth in Figure 4.5 (a) are due to the stress induced by the SiO_2 and poly-Si layers. This stress can be reduced by using Aluminum oxide (Al_2O_3) as a dielectric layer instead of SiO_2. However, Al_2O_3 has a higher thermal conductivity than SiO_2. As discussed in previous chapters, high thermal conductivity is not what we want in the design of thermopile. Although the stress induced by SiO_2 in Figure 4.5(a) appears to be large, the SiO_2 membrane can provide sufficient mechanical strength to this structure [10]. That is exactly the reason why we chose SiO_2 as a dielectric layer to build the thermopile. The scanning electron microscope (SEM) image and the Fourier transform infrared spectroscopy (FTIR) characterization of the CNT/SU-8 mixture absorber are shown in Figure 4.6(a). SU-8 is a commonly used epoxy-based negative photoresist which is a very viscous polymer. The surface of the CNT/SU-8 mixture absorber is not smooth due to the manual process of coating the absorber onto the IR thermopile. The absorption of IR radiation is high, reaching greater than 98.5% from 2 to 8 µm.

To characterize the performance of the thermopile IR sensor using nanometer-thick poly-Si, an electrical measurement was conducted by using a microheater. It is placed at the central part of the thermopile to mimic the IR radiation, as shown in Figure 4.5(b). As explained above in our previous work [10], the use of a microheater to simulate IR radiation introduces only a 1% difference.

118
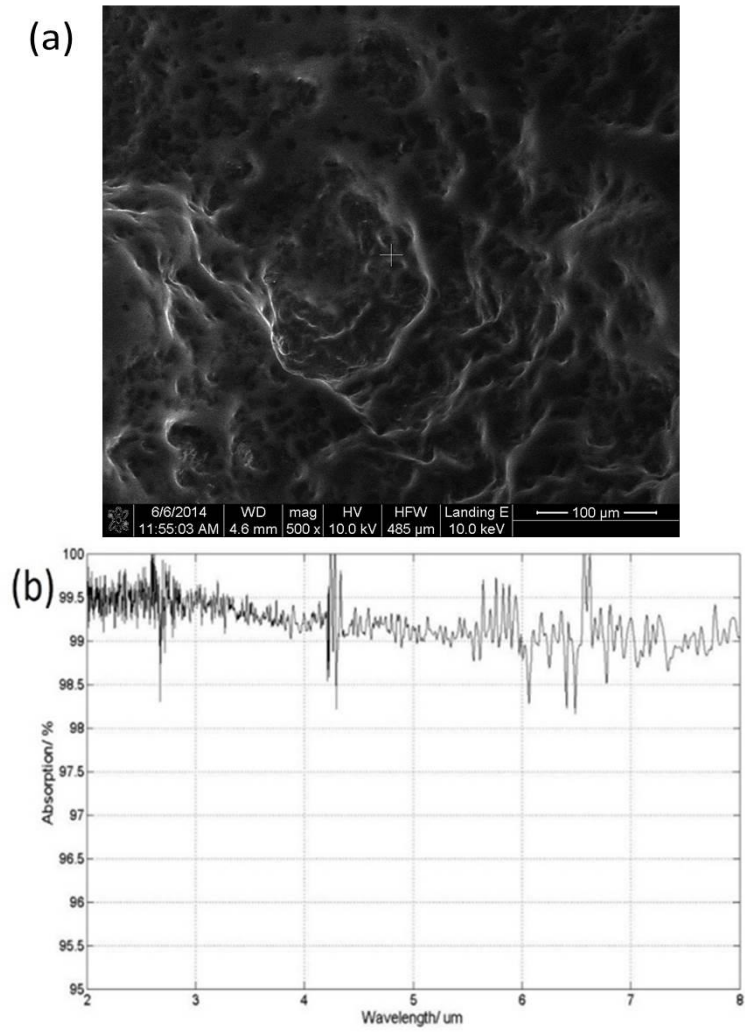
Figure.4.7. SEM image (a) and FTIR measurement results (b) for the CNT/SU-8 mixture absorber.
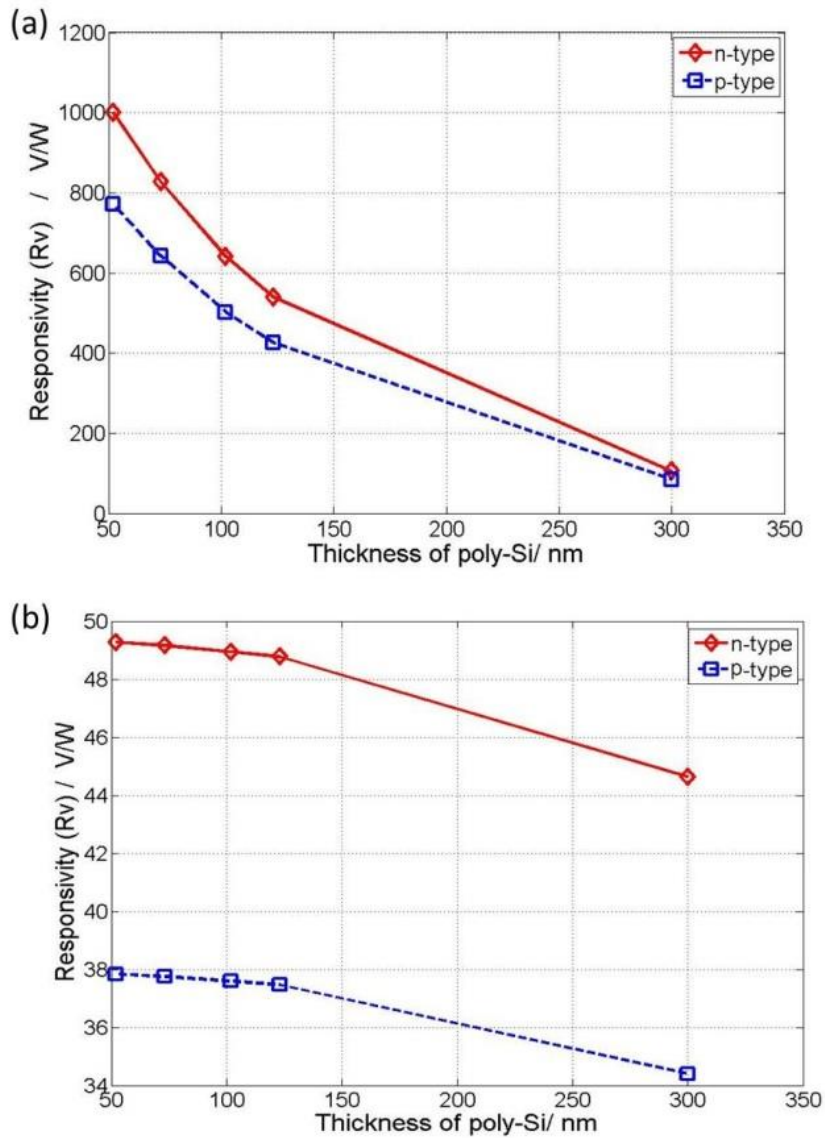
*Figure 4.7. Responsivity (R_v) of n- and p-type poly-Si measured by electrical testing under vacuum
(a) and at atmospheric pressure (b).*

4.2.2 Experiment on the IR sensor

As introduced in Chapter II, the efficiency of a thermopile is typically evaluated based

on two parameters: the responsivity, R_v, and specific detectivity, D^*. R_v represents the

efficiency of conversion from heat to electricity, and D^* represents the precision of

the sensor [9].

The electrical testing was conducted at room temperature, and the results of n- and
p-doped poly-Si-based thermopiles are shown in Figure 4.7. The results of the
experiment conducted in vacuum are shown in Figure 4.7 (a); the thermopile with the
thinnest (52 nm) poly-Si layer, regardless of being n- or p-doped, had the highest R_v.
The R_v of the thermopile with 52 nm-thick n-doped poly-Si was 1000.1 VW^{-1}; the R_v
of thermopile with 300 nm-thick n-doped poly-Si was 105.8 VW^{-1}. This indicates an
845% improvement due to the reduction in the poly-Si thickness. Similarly, the
thermopile using p-doped poly-Si also exhibited a large improvement compared to the
thinner poly-Si. The R_v were obtained as 772.5 and 84.4 VW^{-1} for the p-doped
thermopile with 52 nm-thick and 300 nm-thick poly-Si, respectively. This result
indicates an 815% improvement compared to the thinner p-doped poly-Si.

To study the influence of air on the performance of the thermopile, we conducted the
measurements again at atmospheric pressure. The results are shown in Figure 4.7 (b).
In contrast to the measurement results taken in a vacuum, the R_v values of all
thermopiles decrease by more than one order of magnitude. The increase in R_v caused
by the reduction of poly-Si thickness is not significant as compared to the results
achieved in vacuum because air contributes to most part of the overall thermal
conductivity when the thermopile is working at atmospheric pressure. The R_v values
of the n- and p-doped poly-Si, which have a thickness of 52 nm, decrease to 24.8 and

19.0 VW^{-1}, respectively. The reduction in R_v is more than 97% as compared to the R_v

achieved in the vacuum test. In contrast, the R_v of n- and p-doped poly-Si with a

thickness of 300 nm did not exhibit sharp reductions. They are 23.6 and 18.1 VW^{-1},

respectively, which are around 78% less of the results obtained from the test

conducted in vacuum. As the thermal conductance of the air is the same for all

thermopiles, the reduction in thermal conductance of the structure is not significant

compared to the overall thermal conductance.

Table 4.3. Calculated time constants of the thermopile IR sensors.

Thickness of poly-Si (*nm*)		52	73	102	123	300
Time constant in vacuum (*ms*)	n-doped	87	77	65	58	30
	p-doped	87	78	66	60	32
Time constant at atmospheric pressure (*ms*)	n-doped	0.85	0.89	0.94	0.98	1.27
	p-doped	0.85	0.89	0.94	0.98	1.27

After characterizing the thermopile structure, we conducted an IR radiation test using

a blackbody with a temperature of 470 °C. According to Planck's curve, the radiation

peak is approximately 3.9 μm, which is in the absorption range of the CNT/SU-8

mixture absorber. The details of the testing setup for the radiation test have been

described in our previous work [11].

The IR radiation test was conducted in a vacuum at the room temperature only. The

results are shown in Figure 4.8(a) and (b). The thermopile IR sensor using a

52-nm-thick poly-Si layers had the highest output. For n-doped and p-doped

microdevices, the values are approximately 890% and 700% of those obtained from

the thermopile IR sensor using a 300-nm-thick poly-Si layers, respectively. As shown

in Figure 4.8 (a) and (b), the output voltage decreases with increasing chopper

frequency because the thermopile requires time to heat up. The thermal time constant

of the thermopile IR sensor can be determined based on the time required to reach 63%

of the maximum detector output voltage [12]. Using the data shown in Figure 4.8 (a)

and (b) the time constant of the thermopile IR sensors, with different poly-Si

thicknesses and doping types, were calculated. The calculation results are shown in

Table 4.3.

As the absorption of the IR absorber had not achieved 100%, the responsivity, R_v, of

the IR sensor is different from the R_v measured by the electrical testing. Using

Planck's equation, we estimated that the power applied to the IR sensor is 29.7 μW.

The R_v of the IR sensor, derived from this value, are shown in Figure 4.9 (a).
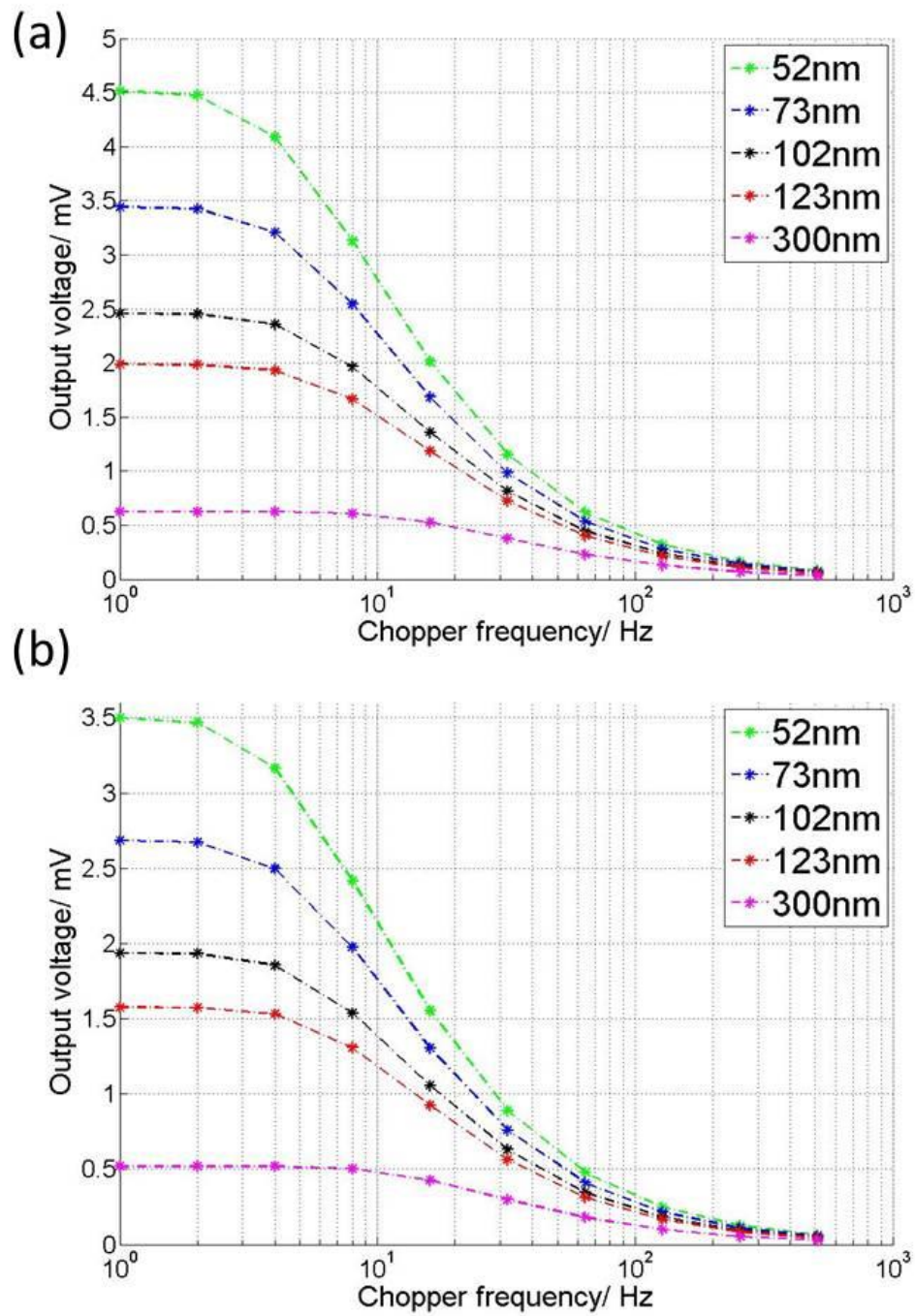
*Figure 4.8. IR responses of n-doped poly-Si (a) and p-doped poly-Si (b) thermopiles with different
chopper frequencies.*

According to the data shown in this figure, the R_v of the IR sensor is only slightly

smaller than the obtained R_v from the electrical test. The overall emissivity, ε, of the

IR sensor is calculated by using Equation 4.18-10:

$$\varepsilon = \frac{R_{v\_IR}}{R_{v\_electrical}} \ ,$$
(4.18-10)

where R_{v_IR} is the R_v of the IR sensor, and $R_{v\_electrical}$ is the R_v obtained in the

electrical test. The average overall emissivity is calculated as 95%.

The combined series of electrical resistances from all sensors are also measured, and

the results are shown in Table 4.4. As there is no current flow through the microdevice,

there is no *1/f* noise, only Johnson noise from the thermopile IR. The Johnson noises

are estimated based on the measured series electrical resistances, and they are shown

in Table 4.4. The specific detectivity, *D**, of each thermopile IR sensor was estimated

as shown in Figure 4.9 (b). The thermopile IR sensors with thinner poly-Si had higher

D*; this is consistent with the testing results of R_v. The *D** of n-doped poly-Si with

thicknesses of 52 and 300 nm are 3.00×10^8 and 5.75×10^7 cmHz$^{1/2}$W^{-1}, respectively;

the *D** of the p-doped poly-Si with thicknesses of 52 and 300 nm are 1.83×10^8 and

3.95×10^7 cmHz$^{1/2}$W^{-1}, respectively. As shown above, the increase in *D** of n- and

p-doped thermopiles with nanometer-thick poly-Si layers are 421% and 364%,

respectively. However, we do not see such significant increases in *D** as compared

with the stated value of R_v; it is because that higher amount of noise is induced by the

increase in electrical resistance due to a thinner poly-Si strip.
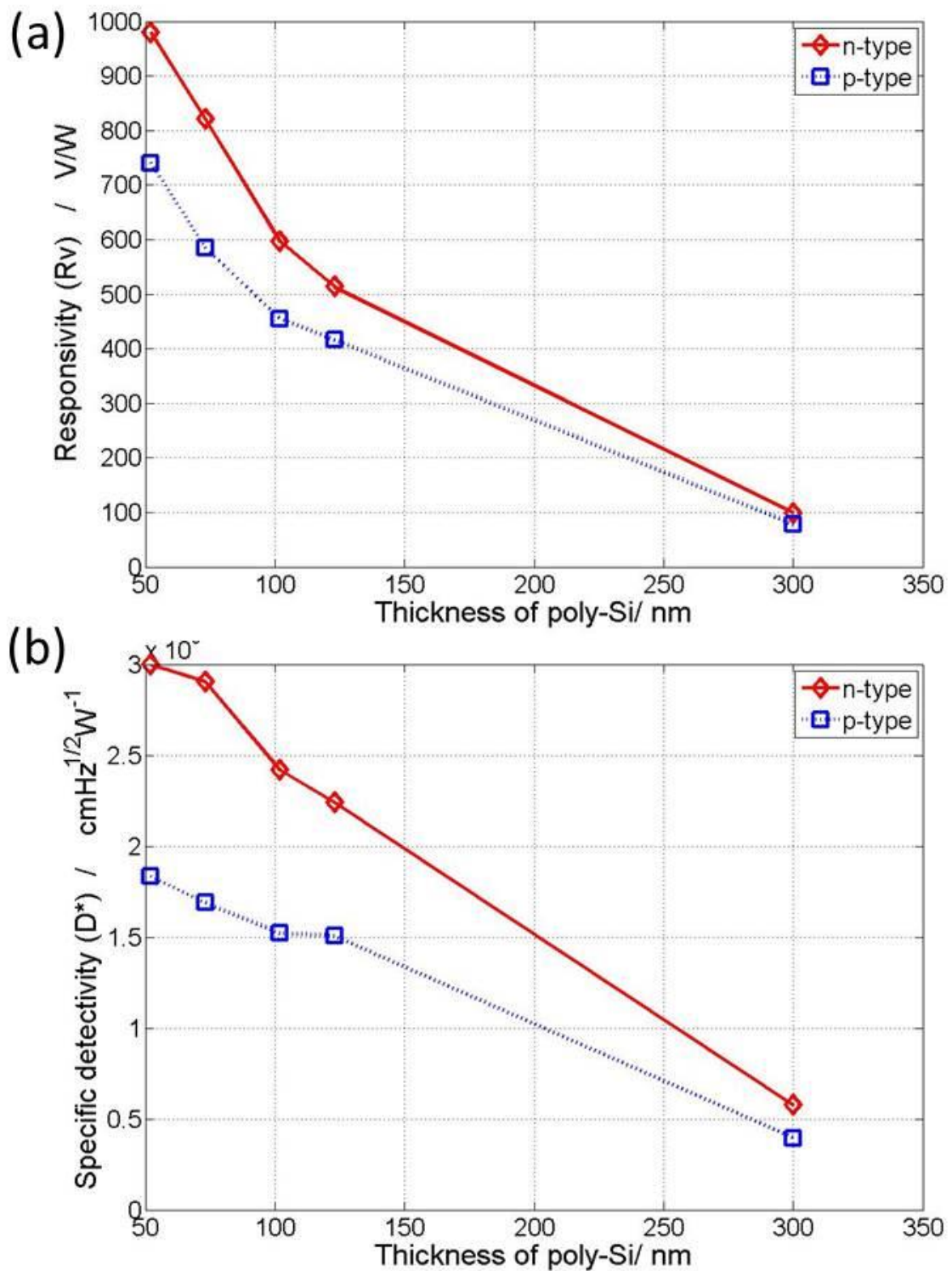
Figure 4.9. Measured responsivity (a) and specific detectivity D* (b) in vacuum.

*Table 4.4. Measured series electrical resistance and estimated Johnson noise of
the thermopile IR sensors.*

Thickness of poly-Si (nm)		52	73	102	123	300
Series electrical resistance ($10^6 \Omega$)	n-doped	1.91	1.43	1.09	0.94	0.52
	p-doped	2.91	2.14	1.60	1.37	0.70
Estimated Johnson noise ($\mu V Hz^{-1/2}$)	n-doped	0.18	0.15	0.13	0.12	0.09
	p-doped	0.22	0.19	0.16	0.15	0.11
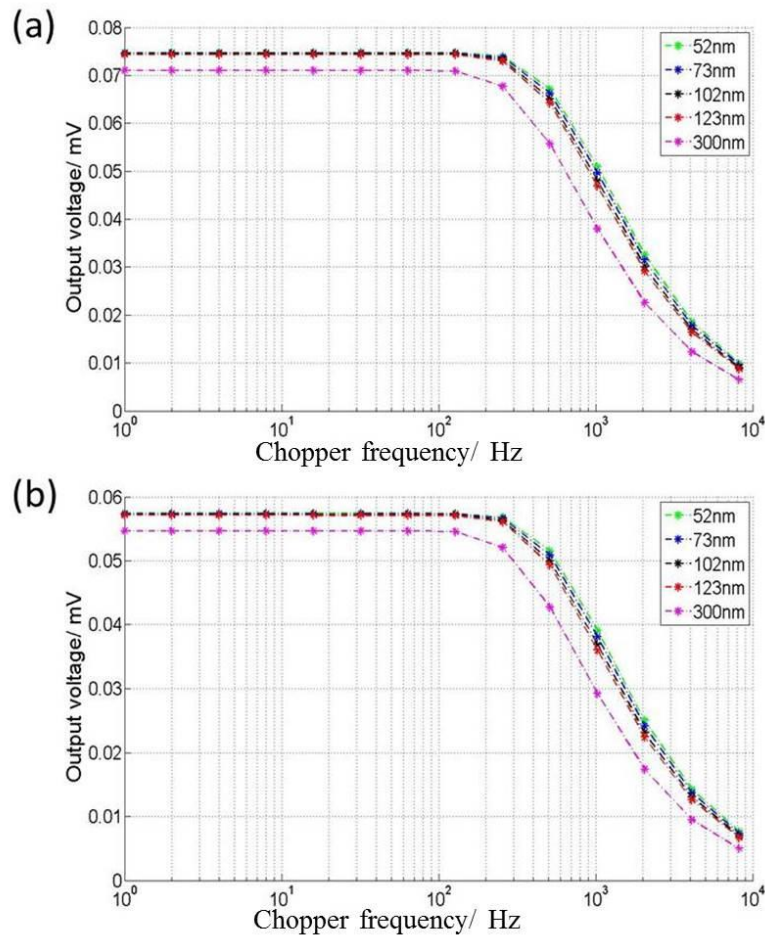
*Figure 4.10. IR responses of n-doped poly-Si (a) and p-doped poly-Si (b) thermopiles with
different chopper frequencies.*

The radiation test was also conducted at atmospheric pressure, and the results are shown in Figures 4.10 and 4.11. As shown in Figure 4.10 (a) and (b), the response of the sensor becomes considerably faster due to the large thermal conductance caused by air. The calculated time constant of the IR sensor is shown in Table 4.3 as well. The main difference between the IR test results obtained at atmospheric pressure, and that obtained in vacuum, is that D^* increases as the thickness of the poly-Si layer increases at atmospheric pressure but decreases in vacuum. As discussed above, as the thermal conductance of air is the dominating factor in this case, the reduction in the overall thermal conductivity caused by the decrease in the poly-Si thickness is not as significant as it is in the vacuum. Therefore, the increase in R_v is also not as significant. In contrast, the noise increases as the thickness of the poly-Si layer decreases. This is why D^*, as shown in Figure 4.11(b), exhibits a different trend when the sensor is at atmospheric pressure.

By leveraging the straightforward fabrication approach, we obtained sound thermoelectric properties for the nanometer-thick poly-Si because of the phonon-boundary scattering effect. This fabrication process is fully CMOS compatible, and it does not use other advanced nanofabrication technologies, such as electron beam lithography (EBL). The demonstrated R_v and D^* values of the thermopile IR sensors are promising for various applications.
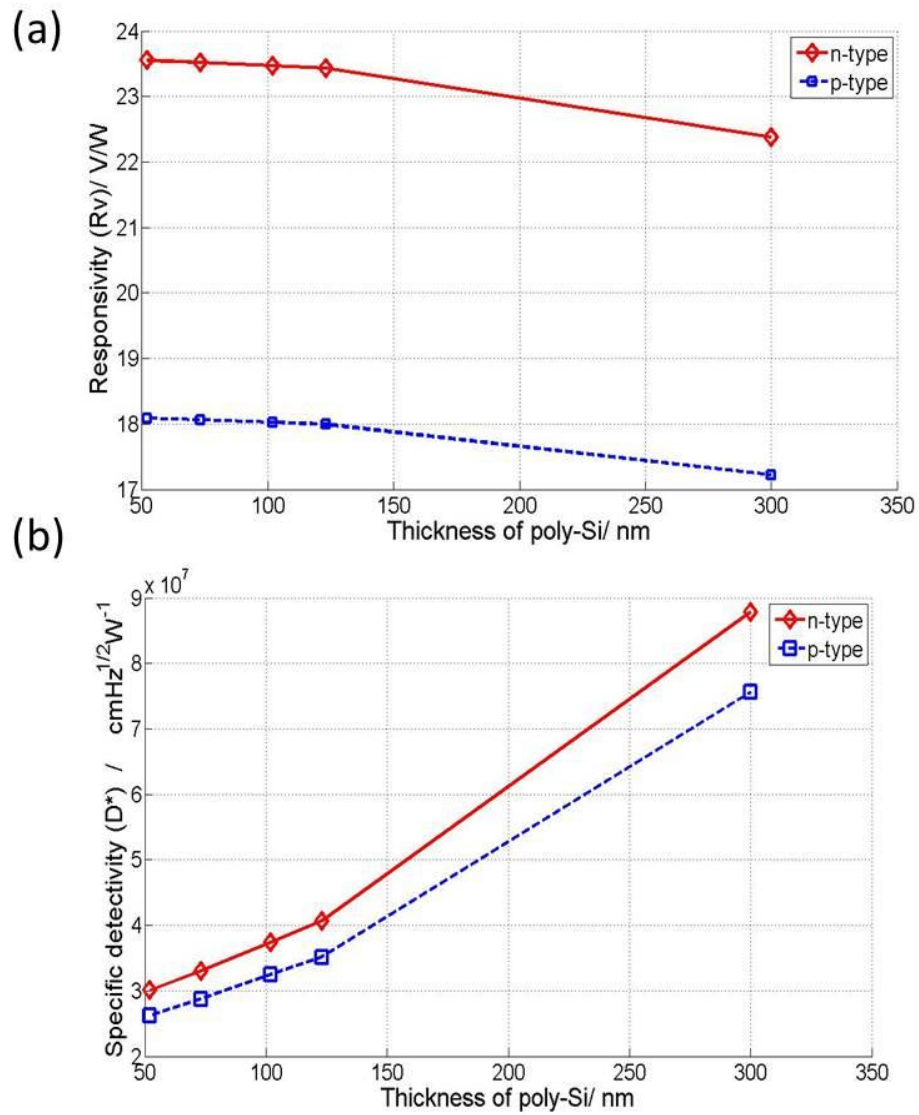
Figure 4.11. Measured responsivity (a) and specific detectivity D* (b) at atmospheric pressure.

4.3 Conclusion

In this chapter, we have studied the thermoelectric properties of nanometer-thick poly-Si, which exhibits an impressive increase in ZT as the decrease in the thickness of the poly-Si leads to significantly reduction in the thermal conductivity. This effect is caused by strong phonon-boundary scattering. The maximum ZT values of 0.067 and 0.024 are obtained for the 52-nm-thick n- and p-doped poly-Si layers, respectively. The ZT values increase by 116% and 92% when the thickness of the poly-Si layer decreases from 300 to 52 nm. We designed, fabricated and tested a thermopile IR sensor using nanometer-thick poly-Si to demonstrate its potential applications in thermoelectric devices. The measured R_v values of the IR sensor using 52 nm n- and p-doped poly-Si were 1000.1 and 772.5 VW^{-1} in vacuum, respectively. The D^* values of the IR sensor using 52 nm n- and p-doped poly-Si were 3.00×10^8 and 1.83×10^8 $cmHz^{1/2}W^{-1}$, respectively. These results illustrate that the R_v of a thermopile IR sensor using 52 nm poly-Si has increased by 845% and 815% for n- and p-doped poly-Si in a vacuum, respectively, as compared to the sensor using 300 nm poly-Si. The D^* values of the thermopile IR sensor using 52 nm n-doped and p-doped poly-Si were improved by 421% and 364% in vacuum as compared to the sensors using 300 nm poly-Si. This result indicates the advantage of the poly-Si with nanometer thickness as a thermoelectric material.

Reference

[1]. Callaway J. Model for lattice thermal conductivity at low temperatures. Physical Review, 1959, 113(4): 1046.

[2]. Holland M G. Analysis of lattice thermal conductivity. Physical Review, 1963, 132(6): 2461.

[3]. McConnell A D, Uma S, Goodson K E. Thermal conductivity of doped polysilicon layers. Microelectromechanical Systems, Journal of, 2001, 10(3): 360-369.

[4]. Uma S, McConnell A D, Asheghi M, et al. Temperature-dependent thermal conductivity of undoped polycrystalline silicon layers. International Journal of Thermophysics, 2001, 22(2): 605-616.

[5]. Paul O M, Korvink J, Baltes H. Determination of the thermal conductivity of CMOS IC polysilicon. Sensors and Actuators A: Physical, 1994, 41(1): 161-164.

[6]. Mandurah M M, Saraswat K C, Helms C R, et al. Dopant segregation in polycrystalline silicon. Journal of applied physics, 1980, 51(11): 5755-5763.

[7]. Zou J, Balandin A. Phonon heat conduction in a semiconductor nanowire. Journal of Applied Physics, 2001, 89(5): 2932-2938.

[8]. Goodson, K. E. Thermal conduction in nonhomogeneous CVD diamond layers in electronic microstructures. Journal of Heat Transfer, 118(2), 279-286 (1996).

[9]. Xie J, Lee C, Wang M F, et al. Characterization of heavily doped polysilicon

films for CMOS-MEMS thermoelectric power generators. Journal of
Micromechanics and Microengineering, 2009, 19(12): 125029.

[10].   Zhou H, Kropelnicki P, Tsai J M, et al. Development of a thermopile
infrared sensor using stacked double polycrystalline silicon layers based on
the CMOS process. J. Micromech. Microeng, 2013, 23(065026): 065026.

[11].   Zhou H, Kropelnicki P, Lee C. CMOS Compatible Midinfrared
Wavelength-Selective Thermopile for High Temperature Applications.

[12].   Strasser M, Aigner R, Lauterbach C, et al. Micromachined CMOS
thermoelectric generators as on-chip power supply. Sensors and Actuators A:
Physical, 2004, 114(2): 362-370.

Chapter V: Study of an infrared absorber

As introduced in Chapter I, different applications of thermopile IR sensors call for different types of integrated IR absorbers. Thermopile IR sensors as image sensors or temperature sensors typically require a relatively broad-band IR absorber because the targeting wavelength range of such sensors is quite wide. For these applications, the integrated IR absorber must have great absorption across a wide wavelength range. Some IR sensors targeting specific objects, e.g., human bodies or missiles, demand a specific wavelength range of IR absorption. For example, the IR image sensors used for surveillance monitoring target temperatures around that of the human body. According to Planck's law, the related wavelength range is from 8 to 14 μm. The IR image sensors made for military use, e.g., for missile detection, target objects with temperatures of hundreds of degrees Celsius; the related wavelength range is from 3 to 5 μm. In these cases, a wavelength selective IR absorber is in need[1].

In this Chapter, I present two types of IR absorber design to satisfy the need for broad-band, wavelength-selective single-band.

5.1 Broad-band IR absorber: CNT/SU-8 mixture IR absorber

One of the most widely used broad band absorbers is metal-black [2], which is a porous nano-structured conducting metal film. Figure 5.1 shows an SEM image and an IR reflectance spectrum for a sample of gold-black. Because the IR transmission of a relatively thick metal is close to 0, the absorption of the absorber can be calculated according to Equation 5.1:

$$a = 1 - r, \qquad\qquad (5.1)$$

where a is absorption and r is reflectance. Figure 5.1 shows that the metal-black absorber has great IR absorption over a wide wavelength range.

However, metal-black has many disadvantages that limit its integration with a thermopile IR sensor. First, because metal-black is a porous metal film, it is extremely fragile; almost all further handling will easily damage it. Even air currents can cause damage to the film. Such limitations make metal-black unsuitable for many applications that demand a robust sensor. Another disadvantage of metal-black is its fabrication process. Metal-black will cover large areas during the deposition process, but it cannot be patterned at sub-mm scale by the traditional metal lift-off process using photoresist and solvents because of its frangibility. The lift-off process will break the metal-black film and put it into a non-absorbing bulk metal state. In addition,

134

its poor durability limits its use as an IR absorber.
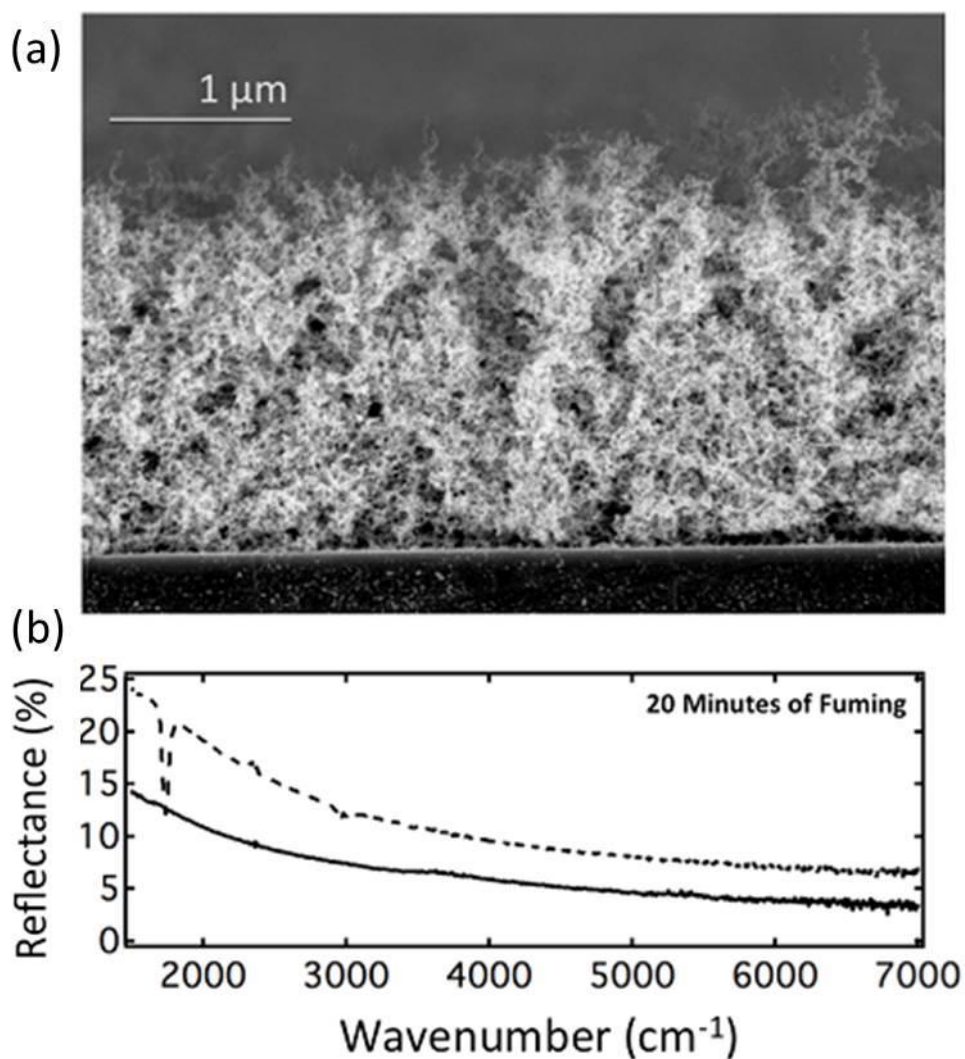
Figure 5.1. (a) Cross-section SEM image and (b) reflectance of the gold-black IR absorber [3].

To avoid the disadvantages of metal-black, I propose a great IR absorber with mixed SU-8 and CNTs.

IR absorbers based on CNTs have been studied since 2005, and they have shown great potential with regard to their absorption efficiency. CNT-based IR absorber paints

135

were reported to have approximately 90% absorbance by J. Lehman and colleagues in 2005 [4]. Vertically aligned CNT forest with a height greater than 400 μm can provide absorption up to 98% [5]. The experimental results from these two cases indicate that aligned and disordered CNTs[6] are capable of high IR absorption. However, a thorough theoretical analysis of the IR absorption of CNTs has not been conducted to date. An individual CNT should have similar absorbance characteristics to elemental carbon [7]. Therefore, the high IR absorption of CNTs should not rely on molecular resonance. The well-accepted explanation of the high IR absorbance characteristics of CNTs is that the aligned or disordered CNTs form a complex surface that traps IR radiation, making the CNTs act as a blackbody. Figure 5.2 illustrates the IR radiation trapping process.
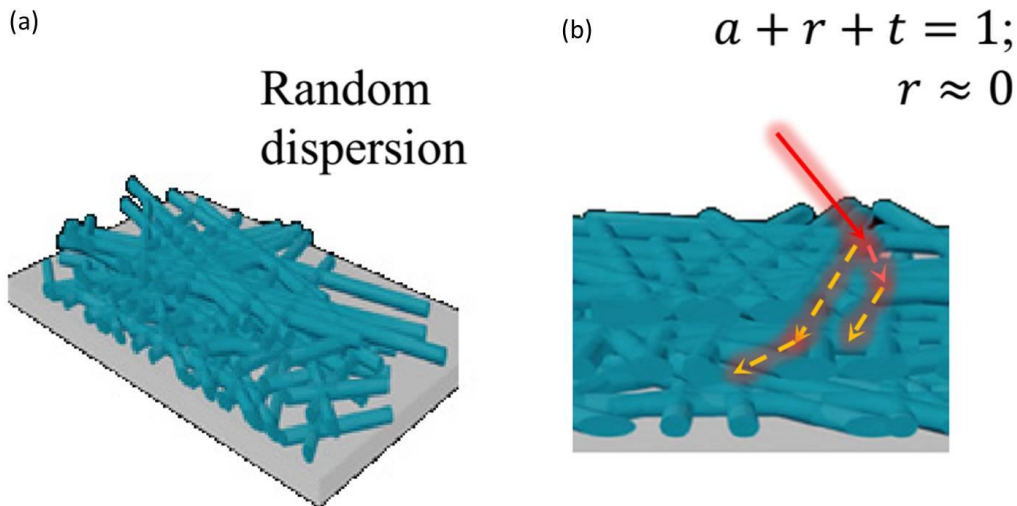
Figure 5.2. (a) Conceptual illustration of a dispersed random network of CNTs embedded in a polymer matrix. (b) The porous structure traps IR photons and absorbs them efficiently over multiple reflections inside the network [7].

However, integrating CNTs on a thermopile IR sensor is not easy because the adhesion of CNT to the dielectric layer is undesirable. In other applications of CNTs, CNTs are typically fixed with electrostatic force, but this method cannot be easily applied to a thermopile IR sensor. According to the thermopile IR sensor design introduced in the previous chapter, the IR absorber must be deposited on a suspended membrane at the central part of the thermopile structure, and the membrane is typically made of dielectric materials that cannot provide sufficient electrostatic force to fix the CNTs. Vertically aligned CNT forests are also not suitable because of their large thermal mass.

To simplify the integration of CNTs on thermopile IR sensors, I mixed CNTs with SU-8 to form a solution that can be easily attached to the thermopile and can be patterned with photo-lithography.

SU-8 is one of the most widely used high-contrast, epoxy-based negative photoresists designed for micromachining and other microelectronic applications. It is a highly viscous polymer that can be deposited with spin coating or spread coating to achieve a thickness ranging from below 1 μm to above 300 μm and still be patterned with standard contact lithography.

The SU-8/CNT mixture is prepared with a 1:5 volume ratio of SU-8 to CNT, and the two components are mixed in an ultrasonic bath for one hour. After the fabrication of

the thermopile structure, 0.1 µL of the mixture is dropped onto the central part of the thermopile. The SEM image of the SU-8/CNT mixture IR absorber and the characterization results using FTIR are shown in Figure 5.3.

As shown in this figure, the surface of the CNT/SU-8 mixture absorber is not smooth; imperfections arise from the manual process of coating the absorber onto the IR thermopile. The absorption of IR radiation is extremely high, exceeding 98.5% from 2 to 8 µm. This absorber was applied to the design of a thermopile IR sensor with nanometer-thick poly-Si, as shown in Chapter IV.
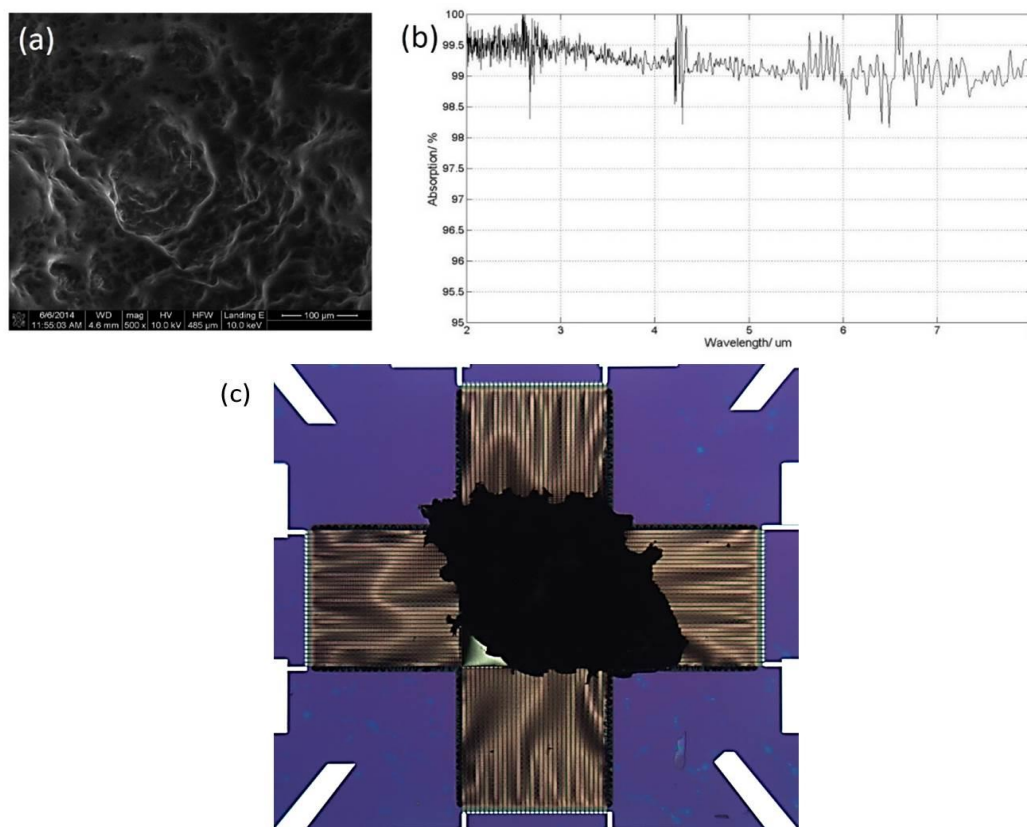
Figure 5.3. (a) SEM image, (b) FTIR measurement results of the CNT/SU-8 mixture and thermopile IR sensor integrated with the SU-8/CNT mixture absorber.

5.2   Single-band   wavelength-selective   absorber: interferometric absorber

Interferometric absorbers, which are also known as quarter-wavelength resonant cavities, are widely used for wavelength-selective absorber design. In 1991, Liddiard conducted an analytical study on interferometric structures in which three stacked layers were used to make absorbers [8]. The absorption spectrum of the interferometric absorber could be adjusted to the desired wavelengths by varying the thickness of the three layers. In contrast to the common approach of packaging a wavelength-selective filter and IR sensor in a metal can to form an IR-based chemical sensor, Liddiard's approach shows another way of making an IR radiation sensor that is wavelength selective. Hence, I used an interferometric-based wavelength-selective absorber in the proposed thermopile-based IR sensor described in this Chapter.

A thin film with a sheet resistance of 189 Ω per square will absorb 50% of the incident radiation. The reflection can be minimized due to impedance matching with atmospheric impedance. The dielectric layer is chosen to maintain a distance between the reflector and absorber of ¼ of the optical wavelength for the IR light, and thus, it contributes to interferometric enhancement, which will ideally provide 100% absorption for the desired wavelength. Equation 5.1 provides the general equation for the absorption of this 3-layer structure, in which the absorption rate α is a function of the wavelength λ.

139

$$\alpha(\lambda) = \frac{4}{Dn^2} \left\{ \left[\frac{f_s(f_r+1)^2}{n^2} + f_r \right] sin^2\theta + (f_r + f_s)cos^2\theta \right\}, \qquad (5.1)$$

where,

$$D = \left[\frac{(f_r+1)(f_s+1)}{n^2} + 1 \right]^2 sin^2\theta + [(f_r + f_s + 2)/n^2]cos^2\theta , \qquad (5.2)$$

$$f_r = 120\pi/R_r, \qquad (5.3)$$

$$f_s = \frac{120\pi}{R_s}, \qquad (5.4)$$

$$\theta = 2\pi nd/\lambda \qquad (5.5)$$

R_s is the sheet resistance of the Titanium Nitride (TiN) nano-thick film; R_r is the sheet resistance of the bottom reflective layer; d is the thickness of the dielectric layer; and n is the refractive index of the dielectric layer.

In this chapter, we present a simple absorber structure that can be applied to any IR sensor. This absorber consists of a TiN film, fabricated by atomic layer deposition (ALD) process, an amorphous silicon dielectric layer and a highly conductive metal reflector.

140
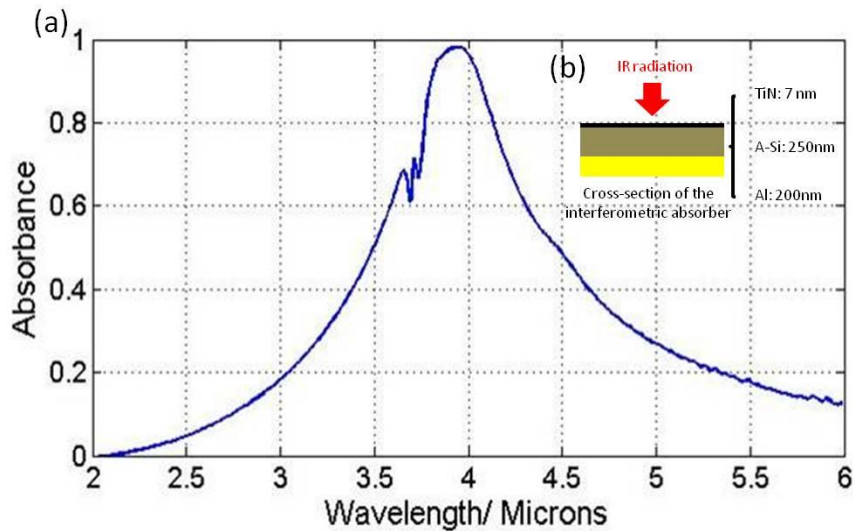
Figure 5.4. FTIR measured data for the interferometric absorber (a) and an illustration of the interferometric absorber (b).

According to K.C. Liddiard's report, the absorption rate depends on the sheet resistance of the top TiN nano-thick layer, which should be 377 $\Omega/°C$, and the position of the absorption peak depends on the thickness and refractive index of the dielectric layer. In this study, the thickness of the top TiN layer is 7 nm, and the rear reflective Al layer is 300 nm. The dielectric layer is amorphous silicon (A-Si) with a refractive index of approximately 4 and a thickness of 250 nm.

FTIR is used to measure the absorption spectrum, and the measurement results are shown in Figure 5.4(a). Figure 5.4(a) shows that the absorption peak is approximately 3.9 μm, at which point the absorption rate can reach approximately 99%. There is a small fluctuation in the spectrum near 3.7 μm, which cannot be explained by the theory discussed above. Further investigation will be required in the future to

141

determine the cause of this fluctuation.

Because this mid-IR sensor is designed for high-temperature applications, it is crucial to study the behavior of the absorber at various temperatures. According to the previous description, the main influence of temperature lies in the resistance change of the top TiN layer with temperature. The TCR of TiN is on the order of 10^{-4} K^{-1} [9]. Thus, the derived resistance difference of TiN from -50°C to 300°C should be less than 10%. Using equations presented in K.C. Liddiard's work [8], we determine that the simulation of the absorption at 3.9 μm with different sheet resistances for the top TiN was conducted. Figure 5.5 shows the simulation results, which indicate that the absorption at 3.9 μm is changed by less than 2%, even when the sheet resistance of the top TiN layer is changed from 300 Ω/°C to 500Ω/°C. In this work, the design sheet resistance of the top TiN layer is 377 Ω/°C. This simulation result indicates that the absorption behavior of the absorber is quite stable at temperatures from -50 °C to 300 °C.
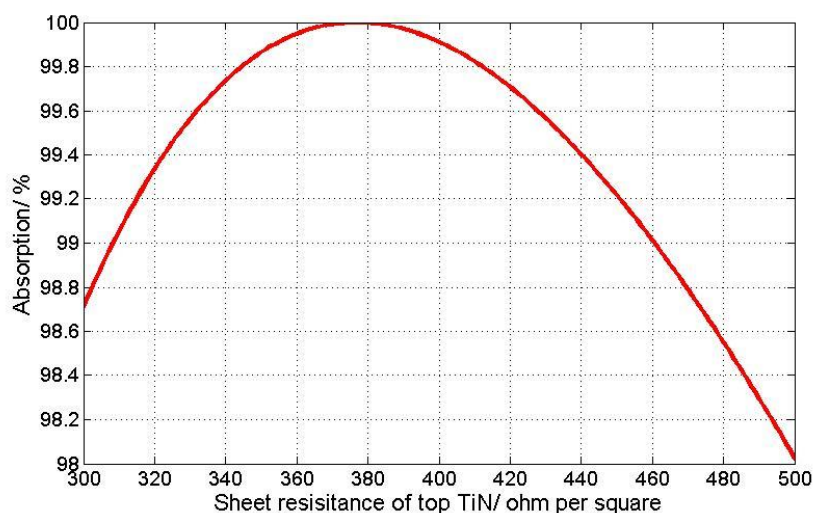
Figure 5.5 Simulation of the absorption at 3.9 μm with different sheet resistance of top TiN

Reference

[1]. Talghader J J, Gawarikar A S, Shea R P. Spectral selectivity in infrared thermal detection. Light: Science & Applications, 2012, 1(8): e24.

[2]. Nelms N, Dowson J. Goldblack coating for thermal infrared detectors. Sensors and Actuators A: Physical, 2005, 120(2): 403-407.

[3]. Harris L, Beasley J K. The infrared properties of gold smoke deposits. JOSA, 1952, 42(2): 134-140.

[4]. Lehman J H, Engtrakul C, Gennett T, et al. Single-wall carbon nanotube coating on a pyroelectric detector. Applied optics, 2005, 44(4): 483-488.

[5]. Mizuno K, Ishii J, Kishida H, et al. A black body absorber from vertically aligned single-walled carbon nanotubes. Proceedings of the National Academy of Sciences, 2009, 106(15): 6044-6047.

[6]. Hagopian J G, Getty S A, Quijada M, et al. Multiwalled carbon nanotubes for stray light suppression in space flight instruments, SPIE NanoScience+ Engineering. International Society for Optics and Photonics, 2010: 77610F-77610F-10.

[7]. Sui Y, Gokhale V J, Shenderova O A, et al. A thin-film infrared absorber using CNT/nanodiamond nanocomposite, MRS Proceedings. Cambridge University Press, 2012, 1452: mrss12-1452-ff05-04.,

[8]. Liddiard K C. Application of interferometric enhancement to self-absorbing thin film thermal IR detectors. Infrared Physics, 1993, 34(4): 379-387.

[9]. Creemer J F, Sarro P M, Laros M, et al. Titanium nitride for MEMS hotplates. Semieonductor adv for future electronics, 2004: 742-746.

Chapter VI: Conclusions and Future Directions

6.1 Summary of the Current Research

In this thesis, I have proposed three main works: improvement of a thermopile structure, optimization of the thermoelectric properties of poly-Si and applications of IR detection with different types of IR absorbers.

CMOS-compatible processes, including the design, fabrication and testing of micromachined n- and p-type poly-Si thermopiles in coplanar and SDL configurations, have been reported. Analytical calculations and experimental data suggest that the SDL thermopile has advantages in terms of thermal conductance and Seebeck coefficient differences, which make the SDL thermopile superior to the conventional coplanar thermopile. Although the resistance of the SDL thermopile is higher than that of the conventional coplanar thermopile, both the responsivity and detectivity of the SDL thermopile are better. This new SDL thermopile has advantages over the conventional coplanar thermopiles due to its small footprint and reduced surface area that is exposed to air. The SDL thermopile is shown to be a superior design in applications that require operating in air.

A CMOS-compatible mid-infrared wavelength-selective thermopile sensor made from

the SDL thermopile and an interferometric absorber is also described. The design, analysis, micro-fabrication and testing of the SDL thermopile structure and the interferometric absorber are presented. The study of the thermoelectric properties of heavily doped n- and p-type poly-Si indicates that the thermopile structure performs better at high temperature, which is consistent with the electrical testing results of the thermopile structure. IR measurements at different temperatures were conducted to determine the optimal working temperature when the source temperature is 470°C. For the output voltage, the fabricated IR sensor yields a maximum value of 0.59 mV at a temperature of 190°C, and the responsivity and detectivity are determined to be 425.7 V/W and $1.25 \times 10^7 \text{cmHz}^{1/2}\text{W}^{-1}$, respectively. These results suggest that thermopile-based mid-IR sensors are suitable for applications that involve operating at a temperature of approximately 200°C.

To optimize the thermoelectric properties of poly-Si, I investigated the thermoelectric properties of phonon-scattering-enhanced nanometer-thick poly-Si. The results indicate the advantages of poly-Si layers with nanometer thickness as thermoelectric materials.

6.2 Future development of thermopile-based IR image arrays

All of my previous designs are single detectors with relatively large dimensions. The

advantages of a thermopile IR image sensor, such as the lack of 1/f noise and the ability to operate without a cooler, make this topic increasingly attractive. To satisfy the demand for IR image arrays, the dimensions of the thermopile must be considerably smaller than that of my previous design, i.e., less than 100 μm. Achieving high efficiency with such small dimensions remains a challenge because the effective length and absorption area are reduced.

One of the most promising methods to develop fantastic thermopile IR image sensors is using novel materials that have advantageous thermoelectric properties.

Among the common thermoelectric materials, Half Heusler materials and complex cell structures [1], such as clathrates and skutterudites (e.g., $Sr_8Ga_{16}Ge_{30}$ [2], $Ba_8Al_{16}Si_{30}$ [3] and $Ba_8Al_xGa_{16-x}Sn_3$ [4]) provide ZT values that are higher than 1 because of their extremely low lattice thermal conductivity. The Seebeck coefficients of these materials are in the same range as doped silicon, i.e., approximately 100 μV/K [1]. However, these materials are not CMOS compatible. In addition, the high ZT values are only observed at high temperature (i.e., beyond 400 K). The ZT values of those materials at room temperature are less than 0.01, which is even worse than doped poly-Si (typically 0.01-0.02). Novel 2D materials, e.g., graphene and Molybdenum disulfide (MoS_2), have been reported as promising thermoelectric materials at room temperature because of their high Seebeck coefficients in the order of 10^4 μV/K [5].

The thermoelectric properties of graphene and MoS$_2$ are shown in Table 6.1 below. Both graphene and MoS$_2$ are suitable for thermoelectric applications due to their giant thermoelectric effects. Additionally, because of its low thermal conductivity and even higher Seebeck coefficient, MoS$_2$ is superior compared to graphene. Compared to the *ZT* values obtained in Chapter III, the *ZT* value of graphene and MoS$_2$ are more than 4 orders of magnitude greater. Although there are still some problems that remain to be solved before these two materials can be applied in real devices, the progress may lead to novel and promising thermopiles. Thus, research and development of these two materials will be one of my main tasks in future work.

Table 6.1. Thermoelectric properties of graphene and MoS$_2$.

	Thermal conductivity (W/mK)	Seebeck coefficient (μV/K)	Electrical resistivity (μΩm)	Figure of merit *ZT*
graphene	200[7]	100[9] ~ 30000 [5]	5[8]	0.003~270
MoS$_2$	~1[9]	-200 [9] ~ -100000 [6]	7[9]	1.7~4.3×10^5

Another solution to develop highly effective thermoelectric materials is to use Si-based phonon-scattering enhanced structures. Si has a good Seebeck coefficient, acceptable electrical resistivity and a properly designed phononic crystal to reduce thermal conductivity significantly [10]. As a result, Si-based phononic crystals will become one of the future's most promising thermoelectric materials.

148

6.3 Development of a dual-band IR absorber

As introduced in Chapter I, the demand for IR absorber for gas detection is more specific. Because most gases have more than one absorption peak, an IR absorber with only one absorption band is not suitable. Therefore, dual-band or even multi-band IR absorbers must be developed to fulfill the requirements of gas detection. Although an interferometric absorber can provide nearly 100% absorption at selected wavelengths, it cannot perfectly fulfill the requirements of an IR-based gas detection system. Figure 6.1 shows the most important vibrational and rotational transitions for carbon monoxide (CO), methane (CH_4), nitrous oxide (N_2O), ozone (O_3), Carbon dioxide(CO_2), Deuterium protium oxide (HDO), water (H_2O), and air. As shown in this figure, CH_4, N_2O and CO_2 all have two absorption peaks, and H_2O has even more absorption peaks. Therefore, an absorber with more than one absorption peak would need to be developed to fulfill the needs for specific detection of those gases.

In my study, I have designed and simulated a dual-band IR absorber using the concept of metamaterials.
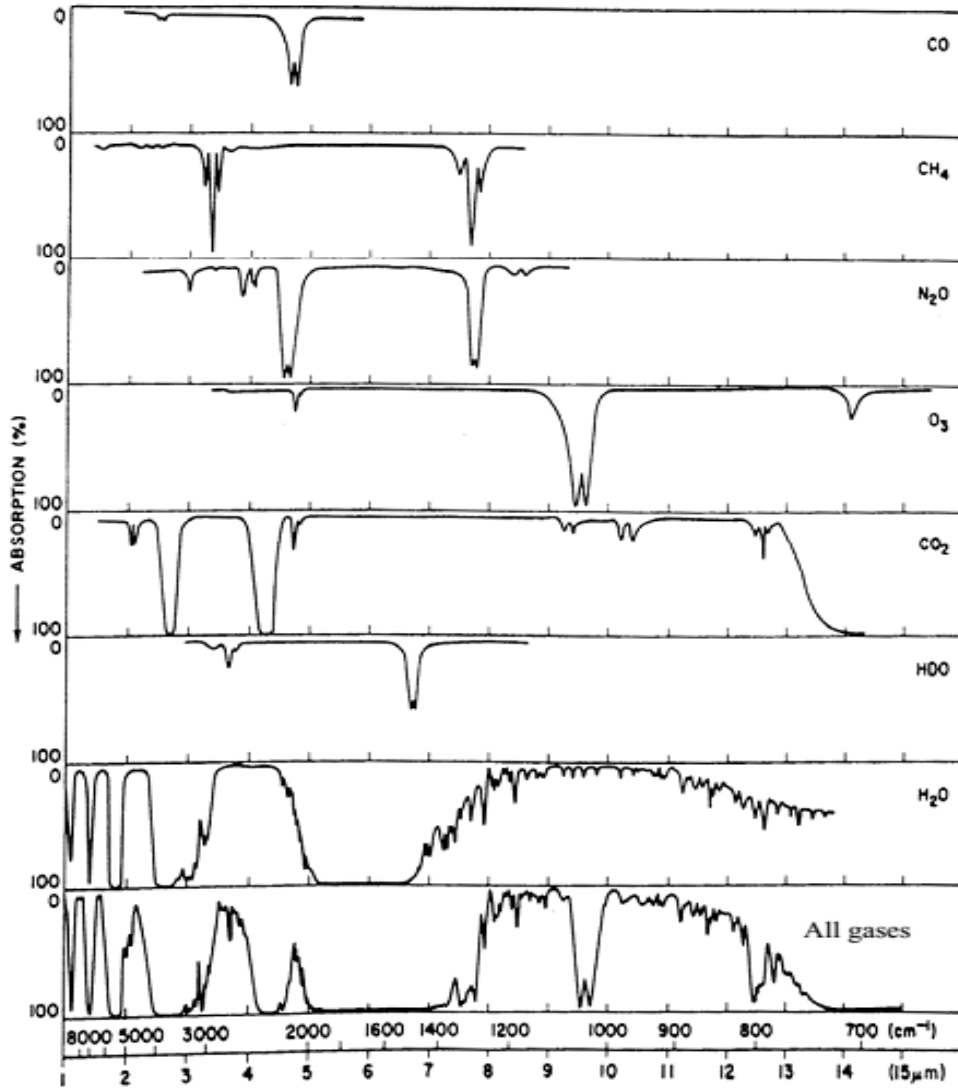
Figure 6.1. Infrared absorption spectra of the major atmospheric gases [11].

Electromagnetic metamaterials are arrays of periodically arranged structures with sub-wavelength size. With proper design, metamaterials can provide specific material properties that do not exist in nature, such as negative permittivity, negative permeability, negative refractive index, and high absorption [12-18].

In this section, I use a variant of the closed ring resonator (CRR) with an offset

150

circular hole in the center. I refer to it as the eccentric closed ring resonator (ECRR).

The concept of the absorber is shown in Figure 6.2 below.
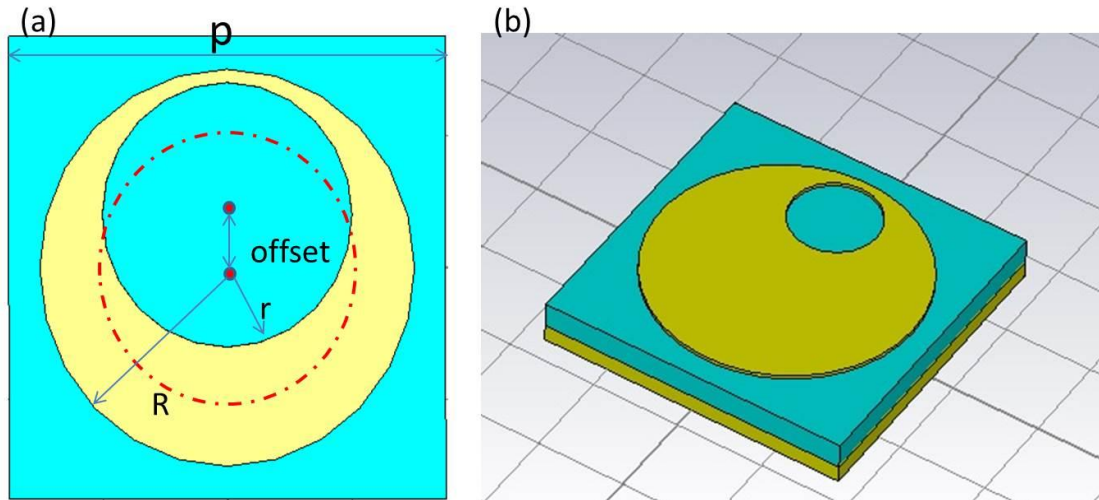
Figure 6.2. Diagram of an ECRR unit cell. (a) Top view, (b) 3D view.

Figure 6.2(a) and (b) shows a top view and 3D view of a unit cell of the ECRR metamaterial absorber. The absorber contains three parts: a bottom total reflection metal layer, a SiO_2 dielectric layer and a top layer of periodically arranged metal patterns. The patterns are aluminum discs with a circle hole inside. If the circle is exactly at the center of the disc, the structure would be a CRR. The red dotted line shows the original position of the circular hole for a traditional CRR. The ECRR is slightly different. The circular hole is not at the center of the disc; it is offset. It is the offset that causes the dual-band absorption behavior of the ECRR.

A simulation using CST Studio Suite 2013 was conducted to study the absorption behavior of the ECRR absorber. The outer radius of the circle is 1,500 nm, and the

151

radius of the hole is 1,000 nm. The thickness of the total reflection metal layer is 200

nm, and the SiO$_2$ dielectric layer is 400 nm. Figure 6.3 shows the influence of the

offset of the hole from 0 nm (traditional CRR). As shown in this figure, the traditional

ERR, without the offset, has only one absorption peak at 3.92 μm, with absorption of

approximately 83%. When the hole is moved up, causing asymmetry in the structure,

a second peak appears, and the intensity of the second peak is greater. The offset

creates a second absorption peak and changes the original peak at 3.92 μm. As the

offset increases, the original peak shifts slightly toward longer wavelengths, and its

absorption increases from 82% to greater than 95%.
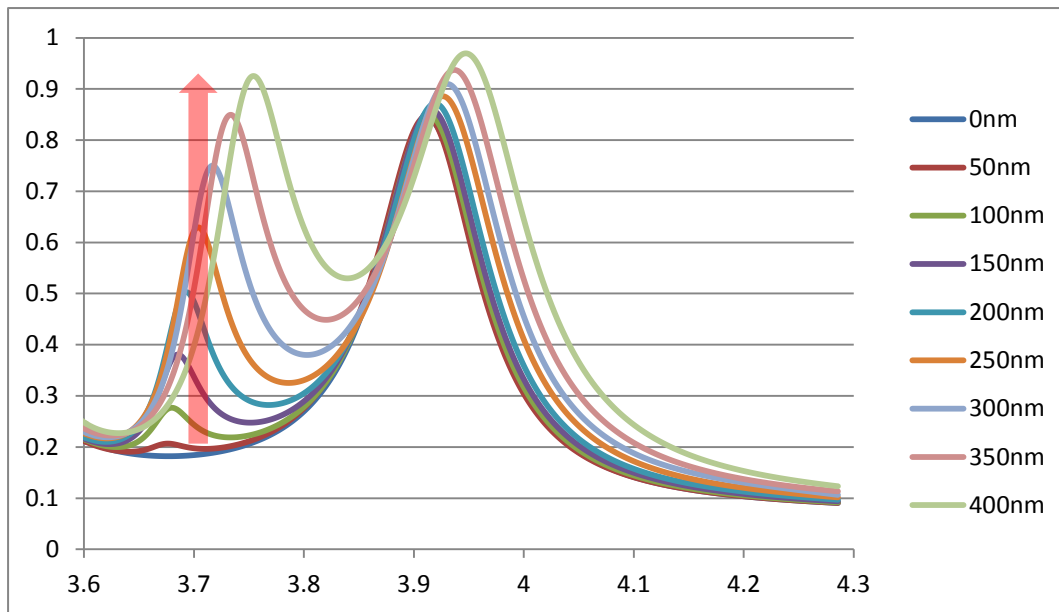
Figure 6.3. Simulation results showing the influence of the offset.

To investigate why the offset leads to the second peak, I observed the surface current

when the ECRR resonates at the two peaks. The distribution of the surface current

when the ECRR resonates at the two peaks is shown in Figure 5-9. Both of the resonant modes are dipolar, and thus, the resonance peak should depend on the effective electrical length of the surface current. The distribution of the surface current at the original peak (resonance peak at longer wavelengths) is shown in Figure 6.3 (a). The direction of the surface current, shown by the blue arrow, is along the outer radius, and it corresponds to the original absorption peak. However, the surface current in the other mode, shown in Figure 6.3 (b), comes from the higher edge of the pattern and flows around the inner hole to converge below the inner hole and finally flow to the lower edge. Because the effective electrical length of this mode is different from the mode shown in Figure 6.3(a), the resonance peak is different. Therefore, there is an additional resonance peak compared to traditional CRR.
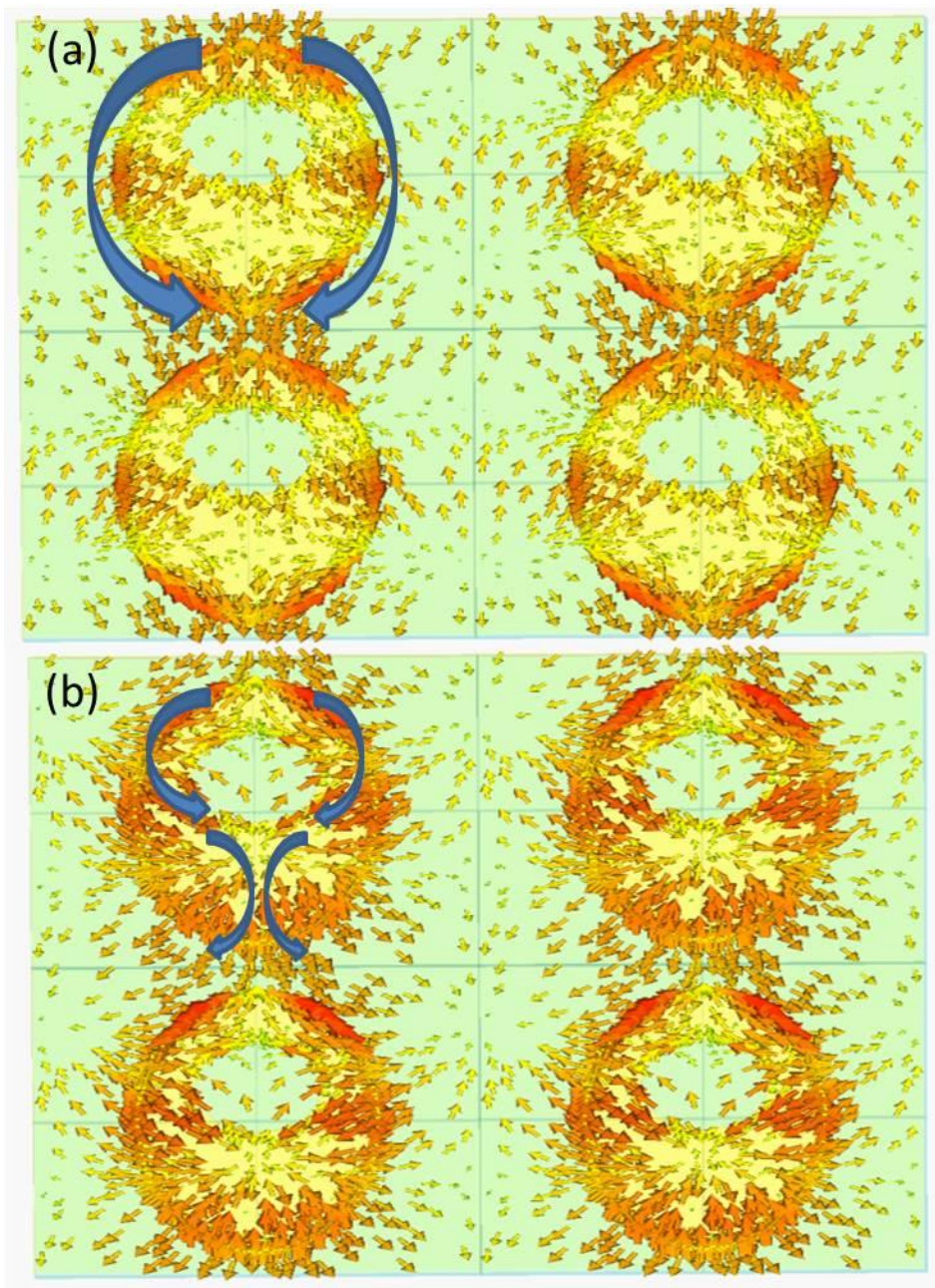
Figure 6.4. Surface current flow of the ECRR. (a) Original resonance peak; (b) Additional resonance peak.

According to the simulation results, the ECRR is capable of dual-band absorption. In my future work, more simulations will be conducted to match the two resonance

peaks to specific gases, such as CO_2 or CH_4. FTIR measurements will also be used to characterize this ECRR dual-band metamaterial absorber.

Reference

[1]. Alam H, Ramakrishna S. A review on the enhancement of figure of merit from bulk to nano-thermoelectric materials. Nano Energy, 2013, 2(2): 190-212.

[2]. Bentien A, Christensen M, Bryan J D, et al. Thermal conductivity of thermoelectric clathrates. Physical Review B, 2004, 69(4): 045107.

[3]. Mudryk Y, Rogl P, Paul C, et al. Crystal chemistry and thermoelectric properties of clathrates with rare-earth substitution. Physica B: Condensed Matter, 2003, 328(1): 44-48.

[4]. Deng S, Saiga Y, Suekuni K, et al. Enhancement of thermoelectric efficiency in type-VIII clathrate Ba8Ga16Sn30 by Al substitution for Ga. Journal of Applied Physics, 2010, 108(7): 073705.

[5]. Dragoman D, Dragoman M. Giant thermoelectric effect in graphene. Applied Physics Letters, 2007, 91(20): 203116.

[6]. Buscema M, Barkelid M, Zwiller V, et al. Large and tunable photothermoelectric effect in single-layer MoS2. Nano letters, 2013, 13(2): 358-363.

[7]. Guo Z, Zhang D, Gong X G. Thermal conductivity of graphene nanoribbons. Applied physics letters, 2009, 95(16): 163103.

[8]. Corey Alan Hewitt, Low Dimensional Carbon Based Organic Thermoelectric

Composites: Synthesis, Characterization, and Performance, PhD thesis, Wake Forest University, Graduate school Of Arts And Sciences, 2013.

[9]. Fan D D, Liu H J, Cheng L, et al. MoS2 nanoribbons as promising thermoelectric materials. Applied Physics Letters, 2014, 105(13): 133113.

[10].   Yu J K, Mitrovic S, Tham D, et al. Reduction of thermal conductivity in phononic nanomesh structures. Nature nanotechnology, 2010, 5(10): 718-721.

[11].   http://irina.eas.gatech.edu/EAS8803_Fall2009/Lec6.pdf

[12].   Shelby R A, Smith D R, Schultz S. Experimental verification of a negative index of refraction. science, 2001, 292(5514): 77-79.

[13].   Soukoulis C M, Linden S, Wegener M. Negative refractive index at optical wavelengths. Science, 2007, 315(5808): 47-49.

[14].   Landy N I, Sajuyigbe S, Mock J J, et al. Perfect metamaterial absorber. Physical review letters, 2008, 100(20): 207402.

[15].   Liu N, Mesch M, Weiss T, et al. Infrared perfect absorber and its application as plasmonic sensor. Nano letters, 2010, 10(7): 2342-2348.

[16].   Watts C M, Liu X, Padilla W J. Metamaterial electromagnetic wave absorbers. Advanced materials, 2012, 24(23): OP98-OP120.

[17].   Fang N, Lee H, Sun C, et al. Sub–diffraction-limited optical imaging with a silver superlens. Science, 2005, 308(5721): 534-537.

[18].   Zhang X, Liu Z. Superlenses to overcome the diffraction limit. Nature

materials, 2008, 7(6): 435-441.

Appendix 1. ANSYS Simulation description

In order to study the dimensions of the thermal electric part, ANSYS was used to do the simulations. Only one thermal couple of the whole thermopile sensor was investigated within the simulation. Figure A1 shows the geometries of the traditional planar thermopile used in the ANSYS model.

Lords: 1w/m2 heat flux on top of Al.

Hot junction

Cold junction

Si substrate
Al
Polysilicon
SiO2

Constant temperature
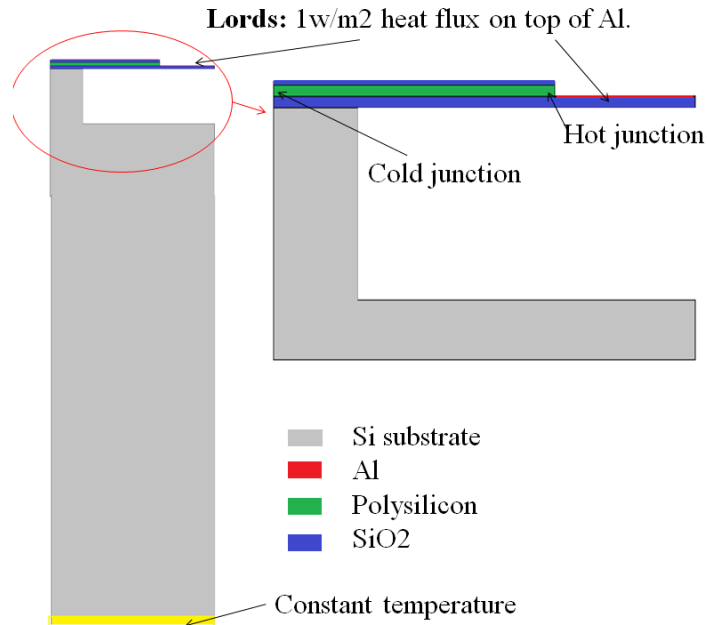
Figure A1. The geometry of traditional planar thermopile in ANSYS.(Half of cross-section view).

Below are the ANSYS codes for combine of length, width and thickness of poly-Si. In order to simulate different dimensions, I just revise the related parameters in this code.

Code for figure 2.3:

```
finish
/clear,nostart
/COM,   Thermal
/prep7
ET,1,PLANE55,,,0
MP,KXX,1,31.9     ! poly; material
MP,KXX,2,1.25     !silico dioxide
MP,KXX,3,149      !silicon
MP,KXX,4,0.000000000001  !vacuum
MP,KXX,5,0.025    !air
```

```
MP,KXX,7,238.6!Al
BTOL,1E-3
*DIM,del,,2


LengthP=300e-6
ThickB=0.4E-6
H=10E-6
ThickSiO2=1.5e-6
ThickP=0.3E-6
ThickA=150E-6          !absorb
LengthA=150E-6        !contack area
LengthB=LengthP+LengthA    !base oxide

As=4*(LengthP+LengthA)*(LengthP+LengthA)
BLC4,0,0,LengthB,200E-6,!base silion
BLC4,0,200E-6,30E-6,15E-6,
BLC4,0,215E-6,LengthP,ThickB,!base silicon dioxide
BLC4,LengthP,215E-6,LengthA,ThickB
BLC4,0,ThickB+215E-6,LengthP,ThickP, !Polysolicon beam1

BLC4,0,ThickB+ThickP+215E-6,LengthP,0.15E-6,!Silicon dioxide2
BLC4,0,ThickB+ThickP+215E-6+0.15E-6,LengthP,ThickP, !Polysolicon beam2

BLC4,0,ThickB+ThickP+215E-6+0.15E-6+ThickP,LengthP,0.15E-6,!Silicon dioxide3
BLC4,LengthP,ThickB+215E-6,1E-6,ThickP+ThickP+0.3E-6+H+1E-6, !Al
BLC4,0,ThickB+215E-6+ThickP+ThickP+0.3E-6+1E-6+H,LengthP+1E-6,1E-6,
!BLC4,LengthP,215E-6+ThickB,LengthA,1E-6;

BLC4,0,0,450E-6,300E-6, !Air

AOVLAP, all

AGLUE,all

asel,s,area,,15!silicon
asel,s,area,,10

AATT,3,,1,
```

```
allsel
asel,s,area,,12!silicon oxide
asel,a,area,,14
asel,a,area,,17
asel,a,area,,16
AATT, 2, , 1,
allsel
asel,s,area,,11        !poly silicon
asel,s,area,,13

AATT, 1, , 1,
allsel
asel,s,area,,18    !Al
AATT, 7, , 1,
allsel

lsel,s,line,,1
Dl,all,,temp,25
allsel
lsel,s,line,,52
SFL,all,HFLUX,1E3
allsel
SMRTSIZE,1
amesh,all
/SOLU
ANTYPE,STATIC
SOLVE
XC=0
YC=ThickP+ThickB+215E-6
XH=LengthP
YH=ThickP+ThickB+215E-6
numcold=NODE(XC,YC,0)
numhot=NODE(XH,YH,0)
*GET,cold,NODE,numcold,TEMP,
*GET,hot,NODE,numhot,TEMP,
del(2)=hot-cold
*CFOPEN,DELJMM,TXT,,APPEND
*DO,J,1,2
*VWRITE,(del(J))
(3F20.12)
```

```
*ENDDO
Finish
```

Code for figure 2.12:

```
finish
/clear,nostart
/COM,   Thermal
/prep7
ET,1,PLANE55,,,0
MP,KXX,1,3.19      ! poly; material
MP,KXX,2,1.25      !silico dioxide
MP,KXX,3,149       !silicon
MP,KXX,4,0.000000000001  !vacuum
MP,KXX,5,0.025    !air

MP,KXX,7,238.6!Al
BTOL,1E-3
*DIM,del,,2



LengthP=300e-6
ThickB=0.4E-6
ThickSiO2=1.5e-6
ThickP=4E-6
ThickA=150E-6          !absorb
LengthA=150E-6       !contack area
LengthB=LengthP+LengthA    !base oxide

As=4*(LengthP+LengthA)*(LengthP+LengthA)
BLC4,0,0,LengthB,200E-6,!base silion
BLC4,0,200E-6,30E-6,15E-6,
BLC4,0,215E-6,LengthP,ThickB,!base silicon dioxide
BLC4,LengthP,215E-6,LengthA,ThickB
BLC4,0,ThickB+215E-6,LengthP,ThickP, !Polysolicon beam1

BLC4,0,ThickB+ThickP+215E-6,LengthP,0.15E-6,!Silicon dioxide2
BLC4,0,ThickB+ThickP+215E-6+0.15E-6,LengthP,ThickP, !Polysolicon beam2

BLC4,0,ThickB+ThickP+215E-6+0.15E-6+ThickP,LengthP,0.15E-6,!Silicon dioxide3
BLC4,LengthP,ThickB+215E-6,1E-6,ThickP+ThickP+0.3E-6, !Al
```

```
BLC4,LengthP+3E-6,ThickB+215E-6,3E-6,ThickP, !POLY heater
AGLUE,all

asel,s,area,,15!silicon
asel,s,area,,11

AATT,3,,1,
allsel
asel,s,area,,13!silicon oxide
asel,a,area,,15
asel,a,area,,17
asel,a,area,,18
AATT, 2, , 1,
allsel
asel,s,area,,12         !poly silicon
asel,s,area,,13
asel,s,area,,10
AATT, 1, , 1,
allsel
asel,s,area,,19    !Al
AATT, 7, , 1,
allsel

lsel,s,line,,1
Dl,all,,temp,25
allsel
lsel,s,line,,39
SFL,all,HFLUX,50E3
allsel
SMRTSIZE,1
amesh,all
/SOLU
ANTYPE,STATIC
SOLVE
XC=0
YC=ThickP+ThickB+215E-6
XH=LengthP
YH=ThickP+ThickB+215E-6
numcold=NODE(XC,YC,0)
numhot=NODE(XH,YH,0)
```

```
*GET,cold,NODE,numcold,TEMP,
*GET,hot,NODE,numhot,TEMP,
del(2)=hot-cold
*CFOPEN,DELJMM,TXT,,APPEND
*DO,J,1,2
*VWRITE,(del(J))
(3F20.12)
*ENDDO
finish
```

Appendix 2. Runsheet for fabrication process

Table A.1. Runsheet for SDL thermopile based IR sensor.

Step	Stage	Operation	Step Description	Equipment	Recipe
1	**Wafer Start (from (CR3/CR2/CR1)**		**Test Wafers: 10wafers**		
2	laser marking	LaserMark	Wafer #1-10 laser marker	08-MET-LaserMarker	
3	Clean	Clean	Wafer #1-10 SPM 10min+QDR+Spin dry	08-CLN-SC1Bench	SPM
4	thermal oxide	Growth	Wafer #1-10 1500A thermal oxidation	08-DIF-SEMCO-Oxide	dry1050C1500A
5	LPCVD polysilicon	CVD	Wafer #1-10 0.7 um polysilicon	08-DIF-SEMCO-LPCVD	Custom Recipe
6	phosphorous implant	Implantation	Wafer #1-9 phos/280Kev/4e15/7 Degree	08-IMP-Implanter	phos/2800Kev/4e15/7 Degree

7	Clean	Clean	Wafer #1-10 SPM 10min+QDR+spin dry	08-CLN-SC1Bench	SPM
8	Annealing	Annealing	Wafer #1-10 Annealing, 1000C, 30min	08-DIF-SEMCO-Oxide	Argon, 1000C, 30min
9	Resistance test	Inspect	Wafer #1-10 Hold for four point test and electric test to check the resistance	08-MET-RsMap	
10	Backside clean	Clean	Wafer #1-8 Standard backside clean process	08-CLN-SEZCleaner	CZ0008
11	**Litho.(# 1): N beam (i)PR-COAT**	Coat	Wafer #1-8 2um photo resist/NO BARC	08-PHL-TELTrack	LA052
12	**(ii)Exposure**	Expose	Mask 1 (N-type Beam structure define) Reticle ID:Infared_N_type Jobfile:	08-PHL-NikonScanner	
13	**(iii)Develop**	Develop	Wafer #1-8 2um photo resist/NO BARC	08-PHL-TELTrack	LA052
14	Polysilicon etching	Etch	Wafer #1-8 0.7um polysilicon etching,choose a recipe with a large etching angle(>90)	08-DRE-P5000	Si-etch-1.3um
15	Inspection	Inspection	DR-SEM	08-MET-DRSEM	
16	PR Strip	PRS	Wafer #1-8 Pr strip	08-DRE-MattsonAsher	
17	Wet clean	Clean	Wafer #1-8 SPM 10min +QDR+SPIN DRY	08-CLN-SC1Bench	SPM
18	LPCVD SiO2 1500A	CVD	Wafer #1-8 1500A LPCVD oxide growth	08-DIF-SEMCO-LPCVD	dry1050C1500A
19	LPCVD polysilicon	CVD	Wafer #1-8 0.7 um polysilicon	08-DIF-SEMCO-LPCVD	Custom Recipe

20	B implant	Implantation	Wafer #1-8, 10 B+/120Kev/4e15/7 Degree	08-IMP-Implanter	B+/120Kev/ 4e15/7 Degree /
21	**Litho.(# 2):P beam (i)PR-COAT**	Coat	Wafer #1-8 2um photo resist/NO BARC	08-PHL-TELTrack	LA052
22	**(ii)Exposure**	Expose	Mask 2 (P-type Beam structure define) Reticle ID:Infrared_P_type Jobfile:	08-PHL-NikonScanner	
23	**(iii)Develop**	Develop	Wafer #1-8 2um photo resist/NO BARC	08-PHL-TELTrack	LA052
24	Polysilicon etching	Etch	Wafer #1-8 1um polysilicon etching	08-DRE-P5000	Si-etch-1.3um
25	Inspection	Inspection	DR-SEM	08-MET-DRSEM	
26	PR Strip	PRS	Wafer #1-8 Pr strip	08-DRE-MattsonAsher	
27	Wet clean	Clean	Wafer #1-8 SPM 10min +QDR+SPIN DRY	08-CLN-SC1Bench	SPM
28	PECVD1000a SiO2	CVD	Wafer #1-8 PECVD1000a SiO2	08-CVD-AMAT-PECVD	FA005
29	**Litho.(# 3): N_contact (i)PR-COAT**	Coat	Wafer #1-8 2.9um photo resist/NO BARC	08-PHL-TELTrack	LA051
30	**(ii)Exposure**	Expose	Mask 3 (p-contact) Reticle ID: Infrared_n_contact Jobfile:	08-PHL-NikonScanner	
31	**(iii)develop**	Develop	Wafer #1-8 2.9um photo resist/NO BARC	08-PHL-TELTrack	LA051
32	Oxide etch	Etch	Wafer #1-8 1000A oxide etch	08-DRE-TELEtcher	ED/POC/USG

33	Inspection	Inspection	Wafer #1	08-MET-DRSEM	
34	n++ implant	Implantation	Wafer #1-8 phosphorous++/100Kev/5e 16/7 Degree	08-IMP-Implanter	phosphorous ++/100Kev/5 e16/7 Degree
35	PR Strip	PRS	Wafer #1-8 Pr strip	08-DRE-MattsonAshe r	
36	Wet clean	Clean	Wafer #1-8 SPM 10min +QDR+SPIN DRY	08-CLN-SC1Bench	SPM
37	Litho.(# 4): P_contact (i)PR-COAT	Coat	Wafer #1-8 2.9um photo resist/NO BARC	08-PHL-TELTrack	LA051
38	(ii)Exposure	Expose	Mask 4 (open via) Reticle ID: Infrared_P_contact Jobfile:	08-PHL-NikonScanne r	
39	(iii)develop	Develop	Wafer #1-8 2.9um photo resist/NO BARC	08-PHL-TELTrack	LA051
40	Oxide etch	Etch	Wafer #1-8 2000A oxide etch (stop on poly)	08-DRE-TELEtcher	ELB009
41	Inspection	Inspection	Wafer #1	08-MET-DRSEM	
42	p++ doping	Implantation	Wafer #1-8 B+/70Kev/5e16/7 Degree	08-IMP-Implanter	B+/70Kev/5 e16/7 Degree
43	PR Strip	PRS	Wafer #1-8 Pr strip	08-DRE-MattsonAshe r	
44	Clean	Clean	Wafer #1-10 SPM 10min+QDR+Spin dry	08-CLN-SC1Bench	SPM
45	Annealing	Common_O peration	Wafer #1-10 Annealing, 1000C, 30min	08-DIF-SEMCO-Oxi de	1000C, 30min
46	Resistance test	Inspect	Wafer #1-10 Hold for four point test and electric test to check the	08-MET-RsMap	

			resistance		
47	Transfer to Cu POD	Wafer_Sort	Wafer #1-2	08-MET-Sorter2	Custom Recipe
48	Metal Deposition	PVD	Wafer #1-2 Ar clean20s-TaN 250A -Al 3000A	08-PVD-EnduraPVD	FL101(change time)
49	Backside clean	Clean	Wafer #1-2 Standard backside clean process Transfer wafers back to non-Cu Pod.	08-CLN-SEZCleaner	CZ0008
50	METROLOGY	Inspection	Wafer #1-2 Hold for microscope to check whether the polymer is clear	08-MET-DRSEM	
51	**LITHO(# 5)**	Coat	Wafer #1-2 PR thickness=1um/NO BARC	08-PHL-TELTrack	LA004
52	**(ii)Exposure**	Expose	Mask 5 (define metal line) Reticle ID: Infrared_Metal line Jobfile:IRSENSOR.METAL	08-PHL-NikonScanner	
53	**(iii)develop**	Develop	Wafer #1-2 PR thickness=1um/NO BARC	08-PHL-TELTrack	LA004
54	Aluminum etch	Etch	Wafer #1-2 250A TaN/3500A aluminum etch, strip PR after etching	08-DRE-MetalEtcher	Al_TaN using Ar with BARC OE=60s
55	Wet Clean	Clean	Wafer #1-2 post Al etch polymer clean	08-CLN-Vert-Cleaner	CV015
56	METROLOGY	Inspection	Wafer #1-2 Hold for microscope to check whether the polymer is clear	08-MET-DRSEM	

57	PECVD SiO2	CVD	Wafer #1-2 1000A PECVD SiO2	08-CVD-AMAT-PECVD	
58	Transfer to Cu POD	Wafer_Sort	Wafer #1-2	08-MET-Sorter2	Custom Recipe
59	Metal Deposition	PVD	Wafer #1-2 Ar clean 20s-TaN 250A -Al 2000A-TaN250A	08-PVD-EnduraPVD	Userdefine
60	Backside clean	Clean	Wafer #1-2 Standard backside clean process Transfer wafers back to non-Cu Pod.	08-CLN-SEZCleaner	CZ0008
61	METROLOGY	Inspection	Wafer #1-2 Hold for microscope to check whether the polymer is clear	08-MET-DRSEM	
62	PECVD	CVD	Wafer #1-2 6000A SiO2	08-CVD-AMAT-PECVD	Userdefine
63	TiN Deposition	PVD	Wafer #1-2 7nm TiN	BR-PVD-ALD	userdefine
64	PECVD	CVD	Wafer #1-2 1000A SiO2	08-CVD-AMAT-PECVD	Userdefine
65	METROLOGY	Inspection	Wafer #1-2 Hold for microscope to check whether the polymer is clear	08-MET-DRSEM	
66	**LITHO(# 6)**	Coat	Wafer #1-2 2.9um photo resist/NO BARC	08-PHL-TELTrack	LA051
67	**(ii)Exposure**	Expose	Mask 6 (release) Reticle ID: Infrared_absorber Jobfile:IRSENSOR.DEFINE	08-PHL-NikonScanner	
68	**(iii)develop**	Develop	Wafer #1-2 2.9um photo resist/NO BARC	08-PHL-TELTrack	LA051

69	Oxide etch	Etch	Wafer #1-2 1.2umoxide etch (do more over etch)	08-DRE-MEMS-Cluster	userdefine
70	Aluminum etch	Etch	Wafer #1-2 250A TaN/3500A/250A TaN/ aluminum/TaN etch, trip PR after etching,	08-DRE-MEMS-Cluster	userdefine
71	Wet Clean	Clean	Wafer #1-2 post Al etch polymer clean	08-CLN-Vert-Cleaner	CV015
72	METROLOGY	Inspection	Wafer #1-2 Hold for microscope to check whether the polymer is clear	08-MET-DRSEM	
73	**LITHO(# 7)**	Coat	Wafer #1-2 2um photo resist/NO BARC	08-PHL-TELTrack	LA052
74	**(ii)Exposure**	Expose	Mask 7 (pad_open) Reticle ID: Infrared_pad_open Jobfile:	08-PHL-NikonScanner	
75	**(iii)develop**	Develop	Wafer #1-2 2um photo resist/NO BARC	08-PHL-TELTrack	LA052
76	Oxide etch	Etch	wafer #2-4 0.3um oxide etch	08-DRE-TELEtcher	
77	METROLOGY	Inspection	Wafer #1-2 Hold for microscope to check whether the polymer is clear	08-MET-DRSEM	
78	PR Strip	PRS	Wafer #1-2 PR strip	08-DRE-MattsonAsher	userdefine
79	Wet Clean	Clean	Wafer #1-2 post Al etch polymer clean	08-CLN-Vert-Cleaner	CV015
80	METROLOGY	Inspection	Wafer #1-2 Hold for microscope to check whether the polymer is clear	08-MET-DRSEM	

81	**LITHO(# 8)**	Coat	Wafer #1-2 4um photo resist/NO BARC	08-PHL-TELTrack	LA058
82	**(ii)Exposure**	Expose	Mask 6 (release) Reticle ID: Infrared_Release Hole Jobfile:IRSENSOR.RELEASEHOLE	08-PHL-NikonScanner	
83	**(iii)develop**	Develop	Wafer #1-2 4um photo resist/NO BARC	08-PHL-TELTrack	LA058
84	Oxide etch	Etch	Wafer #1-2 1um oxide etch (do more over etch)	08-DRE-MEMS-Cluster	userdefine
85	Aluminum etch	Etch	Wafer #1-2 250A TaN/3500A/250A TaN/ aluminum/TaN etch,	08-DRE-MEMS-Cluster	userdefine
86	Oxide etch	Etch	Wafer #1-2 1um oxide etch (do more over etch)	08-DRE-MEMS-Cluster	userdefine
87	DRIE silicon	Etch	Wafer #1-2 DRIE silicon	08-DRE-STS-CMOS	THM 20min
88	METROLOGY	Inspection	Wafer #1-2 Hold for microscope to check whether the polymer is clear	08-MET-MEMs-Scope	
89	PR Strip	PRS	Wafer #1-2 Pr strip	08-DRE-MattsonAsher	
90	Wet Clean	Clean	Wafer #1-2 post Al etch polymer clean	08-CLN-Vert-Cleaner	CV015
91	METROLOGY	Inspection	Wafer #1-2 Hold for microscope to check whether the polymer is clear	08-MET-DRSEM	
92	Silicon etch	Etch	Wafer #1 silicon isotropic etch 100min	08-REL-XeF2-Tool	userdefine

Table A.2. Runsheet for nanometer-thick poly-Si based thermopile based IR sensor.

Step	Stage	Operation	Step Description	Equipment	Recipe
1	**Wafer Start (from (CR3/CR2/CR1)**		**Test Wafers: 10wafers**		
3	LASERMARK	LaserMark	Wafer #1-10 laser marker	08-MET-LaserMarker	User_define
4	WET_CLEAN_ONLY	Clean	Wafer #1-10 SPM 10min+QDR+Spin dry	08-CLN-ManualBench-A	SPM
5	FURNACE_OXIDE	Oxidation	Wafer #1-10 100A SiO2	08-DIF-SEMCO-Oxide	User_define
6	PECVD	CVD	Wafer #1,6 100A SiO2	08-CVD-AMAT-PECVD	FA006
7	FURNACE_LPCVD	Growth	Wafer #1,6 400A polysilicon	08-DIF-SEMCO-LPCVD	User_define
8	FURNACE_LPCVD	Growth	Wafer #2, 7 600A polysilicon	08-DIF-SEMCO-LPCVD	User_define
9	FURNACE_LPCVD	Growth	Wafer #3, 8 800A polysilicon	08-DIF-SEMCO-LPCVD	User_define
10	FURNACE_LPCVD	Growth	Wafer #4, 9 1000A polysilicon	08-DIF-SEMCO-LPCVD	User_define
11	FURNACE_LPCVD	Growth	Wafer #5, 10 1200A polysilicon	08-DIF-SEMCO-LPCVD	User_define
12	METROLOGY	Measurement	Wafer #1-10 Measure thickness of Poly-Si	08-MET-Optiprobe	User_define
13	IMPLANT	Implantation	Wafer #1-5 phosphorous++/40Kev/1e16 /7 Degree	08-IMP-Implanter	User_define
14	IMPLANT	Implantation	Wafer #6-10 B+/20Kev/1e16/7 Degree	08-IMP-Implanter	User_define
15	LITHO	Coat	Wafer #1-10 1um photo resist/NO BARC	08-PHL-TELTrack	LA003
16	LITHO	Expose	Mask 1 (N-type Beam structure define) Reticle ID:Infared_N_type Jobfile:IRSENSOR.NTYPE	08-PHL-NikonScanner	
17	LITHO	Develop	Wafer #1-10	08-PHL-TELTrack	LA003

			1um photo resist/NO BARC		
18	DRY_ETCH_ONLY	Etch	Wafer #1-10 0.2um polysilicon etching,	08-DRE-P5000	User_define
19	METROLOGY_ONLY	Measurement	Wafer #1-10 Check whether the poly-Si is clean	08-MET-DRSEM	User_define
20	DRY_ETCH_PR	PRStrip	Wafer #1-10 1um PR strip	08-DRE-MattsonAsher	User_define
21	WET_CLEAN_ONLY	Clean	Wafer #1-10	08-CLN-Vert-Cleaner	CV005
22	ANNEALING	Anneal	Wafer #1-10 Annealing, 1000C, 30min with pure N2	08-IMP-RTA2BE	User_define
23	PVD	PVD	Wafer #1-10 50A Al2O3	08-PVD-ALD	User_define
24	LITHO	Coat	Wafer #1-10 1um photo resist/NO BARC	08-PHL-TELTrack	LA003
25	LITHO	Expose	Mask 2 (p-contact) Reticle ID: Infrared_n_contact Jobfile::IRSENSOR.NCONTACT	08-PHL-NikonScanner	
26	LITHO	Develop	Wafer #1-10 1um photo resist/NO BARC	08-PHL-TELTrack	LA003
27	DRY_ETCH_METAL	Etch	Wafer #1-10 50A Al2O3 etching	08-DRE-MetalEtcher	User_define
28	METROLOGY_ONLY	Measurement	Wafer #1-10 Check whether the Al2O3 is clean	08-MET-DRSEM	User_define
29	DRY_ETCH_PR	PRStrip	Wafer #1-10 1um PR strip	08-DRE-MattsonAsher	User_define
30	WET_CLEAN_ONLY	Clean	Wafer #1-10	08-CLN-Vert-Cleaner	CV005
31	PVD_ONLY	PVD	Wafer #1-10 500A TiN deoposition	08-PVD-AnelvaPVD	User_define
32	LITHO	Coat	Wafer #1-10 1um photo resist/NO	08-PHL-TELTrack	LA003

			BARC		
33	LITHO	Expose	Mask 3 (define metal line) Reticle ID: Infrared-Metal line-NEW Jobfile::IRSENSOR.METAL L	08-PHL-NikonScanner	
34	LITHO	Develop	Wafer #1-10 1um photo resist/NO BARC	08-PHL-TELTrack	LA003
35	METROLOGY_ONLY	Measurement	Wafer #1-10 Chceck after litho	08-MET-DRSEM	User_define
36	DRY_ETCH_METAL	Etch	Wafer #1-10 500A TiN etchin	08-DRE-MetalEtcher	User_define
37	METROLOGY_ONLY	Measurement	Wafer #1-10 Chceck after etching	08-MET-DRSEM	User_define
38	DRY_ETCH_PR	PRStrip	Wafer #1-10 1um PR strip	08-DRE-MattsonAsher	User_define
39	WET_CLEAN_ONLY	Clean	Wafer #1-10	08-CLN-Vert-Cleaner	CV005
40	LITHO	Coat	Wafer #1-10 4um photo resist/NO BARC	08-PHL-TELTrack	LA058
41	LITHO	Expose	Mask 6 (release) Reticle ID: Infrared_Release Hole Jobfile:IRSENSOR.RELEA SEHOLE	08-PHL-NikonScanner	
42	LITHO	Develop	Wafer #1-10 4um photo resist/NO BARC	08-PHL-TELTrack	LA058
43	DRY_ETCH_METAL	Etch	Wafer #1-10 100A Al2O3 etching	08-DRE-MetalEtcher	User_define
44	DRY_ETCH	Etch	Wafer #1-10 10um Si etching	08-DRE-STS-MEMS	THM 20min
44	WET_CLEAN_ONLY	Clean	Wafer #1-10	08-CLN-SEZCleaner	CV005
45	METROLOGY_ONLY	Measurement	Wafer #1-10 Check after DIRE	08-MET-LithoScope	User_define
46	RELEASE	Etch	Wafer #1-10 silicon isotropic etch	08-REL-XeF2-Tool	

			100min		
47	DRY_ETCH_PR	PRStrip	Wafer #1-10 1um PR strip	08-DRE-MattsonAsher	User_define

Appendix 3. Benchmark of my work and other researchers' work

Table A.3. Benchmark of my work and other researchers' work.

	Number of thermocouples	R_v (V/W)	D^* $(cmHz^{1/2}W^{-1})$
My work (Chapter II)	**96**	**202.8**	**2.85×10^8**
Dehui Xu and et. [1]	64	43.5	2.51×10^8
H Wu and et. [2]	105	294.7	1.31×10^8
Chen and et. [3]	40	138	0.58×10^8

Reference

[1] Xu D, Xiong B, Wang Y. Self-aligned thermoelectric infrared sensors with post-CMOS micromachining. Electron Device Letters, IEEE, 2010, 31(5): 512-514.

[2] Wu H, Grabarnik S, Emadi A, et al. A thermopile detector array with scaled TE elements for use in an integrated IR microspectrometer. Journal of Micromechanics and Microengineering, 2008, 18(6): 064017.

[3] Du C H, Lee C. 3D Thermoelectric structures derived from a new mixed micromachining process. Japanese Journal of Applied Physics, 2000, 39(12S): 7125.